Monte Carlo Simulation of Time of Flight Transient Photocurrents in High Resistivity Semiconductors with Shallow and Deep Traps: Effects of Photoinjection Strength, Duration and Absorption Depth

A Thesis

Submitted to the College of Graduate Studies and Research

In partial fulfilment of the requirements

For the degree of

Master of Science

In the Department of Electrical and Computer Engineering

University of Saskatchewan

Saskatoon

by

JONATHAN A. BALLENDINE

Saskatoon, Saskatchewan

Permission to Use

The author has agreed that the Library, University of Saskatchewan, may make this thesis freely available for inspection. Moreover, the author has agreed that the permission for extensive copying of this thesis for scholarly purposes may be granted the professor, who supervised the thesis work recorded herein, or in his absence, by the Head of the Department or the Dean of the College in which this thesis work was done. It is understood that due recognition will be given to the author of this thesis and to the University of Saskatchewan in any use of the material in this thesis. Copying or publication or any other use of this thesis for financial gain without approval by the University of Saskatchewan and the author's written permission is prohibited.

Requests for permission to copy or make any other use of the material in this thesis are whole or in part should be addressed to:

Head of the Department of Electrical and Computer Engineering

3B48 Engineering Building

57 Campus Drive

University of Saskatchewan

Saskatoon, Saskatchewan

S7N 5A9

Abstract

Amorphous selenium (a-Se) alloys are currently used as x-ray photoconductors in modern digital direct conversion flat panel detectors. Time-of-flight (TOF) transient photoconductivity technique is widely used in the characterization of a-Se alloy photoconductors for quality control. Using MATLab as a modeling tool, Monte Carlo techniques have been performed to simulate the transport of photogenerated charge carriers through a readily definable generic photoconductor material. High carrier injection ratios, finite absorption depths, as well as long photogeneration times are examined to evaluate their effects on the propagating charge carrier packet and transient photocurrent shape. It is assumed that the photoconductor has a set of shallow traps and a set of deep traps. The distinct effects of shallow and deep trapping on the transient photocurrent are also examined subject to different levels of photoinjection. The extent of carrier charge dispersion during drift is also examined as a function of the injection ratio, photogeneration absorption and duration, and the capture and release times associated with localized sates.

Acknowledgements

No academic work, much less this one, can be considered complete without recognizing the efforts and contributions of the other stakeholders involved. Chief among them, I'd like to thank my supervisor, Dr. Safa Kasap, whose invaluable guidance and material support made this work possible. I'd also like to thank his team, including Cyril Koughia for his academic support, Derek Mortensen for his experimental results, and Joel Frey for his assistance in formulating my testing algorithms. I'd like to thank the ANRAD Corporation for their financial support, and the Engineering Department's administrative staff for managing my status at the University. And lastly, I'd like to thank my wife Sharon, and the rest of my family for their nigh endless patience over eight months of me dominating the computer for my simulations, and for being there to bounce ideas off of when inspiration was in short supply.

Table of Contents

Permission to Use i

Abstract ii

Acknowledgements iii

Table of Contents iv

Table of Figures vi

List of Terms ix

Chapter 1 Introduction 1

1.1 Background and Applications 1

1.2 Applications in Radiography 2

1.2.1 Indirect Conversion Techniques 4

1.2.2 Direct Conversion Techniques 5

1.3 Application of Amorphous Semiconductors in Consumer Electronics 8

1.4 Applications in Photovoltaic Cells 9

1.5 Summary of work 11

Chapter 2 Transient Photoconduction 12

2.1 Introduction 12

2.2 Photon Absorption and Generation 13

2.3 Time of Flight simulation 14

2.4 Injection ratio 15

2.5 Photoconduction 17

2.5.1 Diffusion 17

2.5.2 Field Assisted Drift 18

2.6 Applicable materials 22

2.7 Summary 24

Chapter 3 Monte Carlo Simulation 25

3.1 MATLab functionality 25

3.2 Methodology – Test plan 30

3.2.1 Phase One – Generic Crystalline Semiconductor 30

3.2.2 Phase Two – Generic Amorphous Semiconductor 37

3.2.3 Detailed Balance 47

3.3 Summary 50

Chapter 4 Results and Discussion 52

4.1 Phase One 52
4.1.1 No variation in carrier package generation 52
4.1.2 Gaussian distribution of generation time 56
4.1.3 Exponential distribution of absorption depth 62
4.2 Phase Two 70
4.2.1 Discrete shallow trapping 71
4.2.2 Discrete bi-level trapping 82
4.2.3 Gaussian shallow trapping 92
4.3 Summary 98
Chapter 5 Conclusion 100
5.1 Observations 100
5.2 Implications 101
5.3 Future Work 102
5.3.1 Recombination effects 103
5.3.2 Trap filling effects 104
5.3.3 Poole-Frenkel emission 104
5.3.4 Ghosting and residual effects 105
References 107

Table of Figures

Figure 1-1: X-ray attenuation though generic tissue sample. **4**
Figure 1-2: X-ray film cartridge image dispersion **5**
Figure 1-3: Cross sectional schematic of a pair of AMA photo-detector pixels **6**
Figure 1-4: Sample of the substrate layer of an AMA photodetector screen showing the pixel grid and the charge polling electronics[] **7**
Figure 1-5: Schematic plans for a variety of TFT devices using amorphous silicon for the channel.[] **9**
Figure 2-1: Semiconductor materials as classified by the periodicity of their atomic lattice structure (a) Long Range Order - crystalline (b) Short Range Order - amorphous **12**
Figure 2-2: Example of how the presence of foreign charges might interfere with the electric field across the medium. Cases shown are (a) low injection, (b) high injection, and (c) saturation. **16**
Figure 2-3: Simplified examples of diffusion and field assisted drifting. As the applied field increases, the diffusion movement becomes less pronounced against the drift movement. The diffusion rate doesn't change, but the carrier has much less time to diffuse. **19**
Figure 2-4: Sample mid-gap DOS acquired through Laplace transform analysis. Models shown are (a) amorphous selenium[], (b) hydrogenated amorphous silicon[] (dashed plot applied Tikhonov regularization to compute) and (c) polycrystal CZT[] (also using Tikhonov regularization) **24**
Figure 3-1: Package count test results vs. processed result **29**
Figure 3-2: Processed package count test results **29**
Figure 3-3: Energy band diagram and Time of Flight waveforms for an individual photogenerated EHP in crystalline material assuming $\mu_h > \mu_e$ **30**
Figure 3-4: Flow diagrams for (a)main simulation and (b) electric field computation **34**
Figure 3-5: Energy band diagram and TOF waveform for an individual EHP drifting through an amorphous semiconductor showing the photocurrent staggering effects of trapping **37**
Figure 3-6: Flow chart for trap/release modelling and drift/current calculation for an individual electron carrier package. **40**
Figure 3-7: Time of Flight transient waveform for (a) raw output, (b) processed output, showing smoothing filter exaggerated thermalization and (c) derivative function of processed output and corresponding dispersion D, as measured in multiples of the transit time **41**
Figure 3-8: Response of release time τ_R to changes in θ for preset capture times of $\tau_C = 0.001t_T$, $0.01t_T$, and $0.1t_T$. **44**
Figure 3-9: Energy band diagram for gaussian distributed mono-energetic trapping with constant state concentration N, mean energy depth $\mu = E_S$, and energy depth standard deviation $\sigma = \Delta E/2$ **46**
Figure 4-1: TOF results for infinitesimally thick carrier plane including (a)induced transient photocurrent and (b) transit time as a function of injection ratio **53**
Figure 4-2: Package distributions and electric fields for infinitesimal carrier package plane at times $t = 0.1t_T$, $0.5t_T$, $1.0t_T$, and $1.5t_T$ for injection ratios of (a) r = 0.01% (b) r = 10% (c) r = 50% (d) r = 99% **55**
Figure 4-3: Time dependence of field balancing constant C_E for infinitesimal carrier package plane **56**
Figure 4-4: Dispersion comparisons for Gaussian generation time (a)as measured and (b) as a multiple of the low injection case dispersion $D_{0.0001}$ **57**
Figure 4-5: TOF waveform results for Gaussian generation time for (a)$\sigma = 0.01t_T$,(b) $\sigma = 0.05t_T$, (c) $\sigma = 0.10t_T$, (d) $\sigma = 0.15t_T$, and (e) $\sigma = 0.20t_T$ **58**

Figure 4-6: Carrier package distributions and corresponding electric fields for Gaussian generation time test for $\sigma = 0.1t_T$ at $t = 0.1t_T$, $0.5t_T$, $1.0t_T$, and $1.5t_T$ for (a) r = 0.01%, (b) r = 10%, (c) r = 50%, and (d) r = 99% **62**

Figure 4-7: Generated photocurrents and their corresponding time derivative functions for delta absorption tests with mobility ratio b = 0.1 for (a)electron current $I_e(t)$, (b)hole current $I_h(t)$, and (c)total current $I_e+I_h = I_t(t)$. **64**

Figure 4-8: Generated photocurrents and their corresponding time derivative functions for delta absorption tests with mobility ratio b = 1.0 for (a)electron current $I_e(t)$, (b)hole current $I_h(t)$, and (c)total current $I_e+I_h = I_t(t)$. **65**

Figure 4-9: Generated photocurrents and their corresponding time derivative functions for delta absorption tests with mobility ratio b = 10.0 for (a)electron current $I_e(t)$, (b)hole current $I_h(t)$, and (c)total current $I_e+I_h = I_t(t)$. **66**

Figure 4-10: $C_E(t)$ compared to number of each carriers type collected per time step dt for ratios of r = 0.0001 and 0.99 and mobility ratios (a) b = 0.1, (b) b = 1.0, and (c) b = 10.0 **68**

Figure 4-11: Carrier package distributions and corresponding electric fields for delta absorption testing with mobility ratio = 1.0 for injection ratios (a)0.0001, (b)0.10, (c)0.50, and (d)0.99 **70**

Figure 4-12: Example of noise prevalence as a product of θ, which governs the equilibrium current level. **73**

Figure 4-13: Dispersion D and $D/D_{0.0001}$ compared against the injection ratio r, including the theoretical low-injection dispersion values D_{th} as computed from Eq 2-11 for (a) $\tau_C = 0.001\ t_T$, (b) $\tau_C = 0.010\ t_T$ and (c) $\tau_C = 0.100\ t_T$. **75**

Figure 4-14: TOF transient photocurrents for single discrete level trapping simulations with θ = 0.001, and τ_C = (a)0.001, (b)0.010, and (c)0.100 **76**

Figure 4-15: TOF transient photocurrents for single discrete level trapping simulations with θ = 0.010, and τ_C = (a)0.001, (b)0.010, and (c)0.100 **77**

Figure 4-16: TOF transient photocurrents for single discrete level trapping simulations with θ = 0.100, and τ_C = (a)0.001, (b)0.010, and (c)0.100 **78**

Figure 4-17: Transit times for monoenergetic trap tests showing all time measurements for τ_C and θ = (a) $0.001\ t_T$ and 0.001(b) $0.001\ t_T$ and 0.1 (c) $0.1\ t_T$ and 0.001 (d) $0.1\ t_T$ and 0.1. **79**

Figure 4-18: Scale adjusted field balancing $C_E(t)$ plots for all injection ratios using capture times of τ_{CS} = (a) $0.001\ t_T$, (b) $0.010\ t_T$, and (c) $0.100\ t_T$ **80**

Figure 4-19: Carrier position histograms for the lowest and highest carrier injection cases for τ_{CS} = (a) $0.001\ t_T$, (b) $0.010\ t_T$, and (c) $0.100\ t_T$ **81**

Figure 4-20: TOF transient photocurrent and derivative function corresponding to testing data listed in Table 4-7. Note that the r = 0.50 case returned a curve for which FWHM measurement could not be used to identify the dispersion, while the r = 0.99 case returned a distorted dispersion value. **84**

Figure 4-21: Capture incidence as obtained for deep capture rates $1/\tau_{CD}$ = 0 (no deep capture), 1/3, 1, and 3. Cases shown are for (a)$\tau_{CS} = 0.001t_T$ and (b) $\tau_{CS} = 0.100\ t_T$. **85**

Figure 4-22: Dispersion measurements for bi-level trapping tests showing changes to injection ratio response for τ_{CS} and θ of (a) $0.001\ t_T$ and 0.001 (b) $0.01\ t_T$ and 0.1 (c) $0.01\ t_T$ and 0.001 and (d) $0.01\ t_T$ and 0.1. **86**

Figure 4-23: Processed transient TOF waveforms for four simulation sets with the same values for parameters τ_{CS} and θ_S, but varying preset deep capture time as τ_{CD} = (a) infinite, (b) $3t_T$, (c)$1t_T$, and (d) $1/3t_T$ **88**

Figure 4-24: Derivative function plots for processed TOF waveforms of Figure 4-17, for τ_{DC} = (a) infinite, (b) $3t_T$, (c) $1t_T$, and (d) $1/3t_T$ **89**

Figure 4-25: Field balancing factor plots for tests with varying deep carrier trapping rates. Shallow capture and release rates are kept constant with deep capture times of τ_{CD} = (a) infinity, (b) 3 t_T, (c) 1 t_T, and (d) 1/3 t_T. **90**

Figure 4-26: Histograms for carrier positions at sample times 1 t_T, 4 t_T, 8 t_T, and 12 t_T for varied deep trapping times of (a) infinity, (b) 3 t_T, (c) 1 t_T, (d) 1/3 t_T **92**

Figure 4-27: Dispersion as measured and normalized against low injection case compared with injection ratio for single Gaussian range trapping tests, including tests for τ_C = 0.010 t_T and (a,b) θ = 0.001 and (c,d) θ = 0.1 **94**

Figure 4-28: Trap depth histograms and corresponding TOF waveforms for lowest and highest injection ratios by variance ΔE for τ_C = 0.010 and θ= (a) 0.001, (b) 0.010, and (c) 0.100. **95**

Figure 4-29: TOF waveforms and differential functions for Gaussian trap energy depth testing. Tests shown are for τ_C = 0.010 t_T, θ = 0.010, and ΔE = (a) 0.0001, (b) 0.01, and (c) 0.1 **97**

List of Terms

a-Si:H	Hydrogenated amorphous silicon
a-Se	Amorphous selenium
AMA	Active Matrix Array
CDF	Cumulative distribution function
CVD	Chemical Vapour Deposition (CdZnTe)
CZT	Cadmium-Zinc-Telluride
DOS	Density of states
E_c	Conduction band lower energy limit
E_g	Bandgap energy E_c - E_v
E_v	Valence band upper energy limit
EHP	Electron hole pair
FET	Field effect transistor
FWHM	Full width – Half maximum
IGZO	Indium Gallium Zinc Oxide
LRO	Long range order
PbI_2	Lead iodide
PET	Polyethyline terephthelate
SRO	Short range order
TFT	Thin film transistor
TOF	Time of Flight
t_T	Carrier transit time

Chapter 1 Introduction

1.1 Background and Applications

Semiconductor research has come a long way since Shockley, Bardeen, and Brattain created the first transistor in 1947. Their simple point-contact transistor device has given rise to generations of solid state devices which have transformed almost every aspect of modern society. Crystalline devices, which are recognized by the coherence of their component atoms to a highly periodic atomic structure, have led the way in revolutionizing fields such as communications, control systems, and entertainment. Specifics aside, this was a predictable consequence of the relative simplicity that comes from building devices whose behaviour can be so readily described mathematically. Amorphous semiconductor devices are not so simple, but the logistical factors in their fabrication, combined with the known limitations of crystalline devices, have led to some compelling applications; provided that problems resultant of their innate complexities can be resolved.

One such material, the primary material of interest in this work, is alloyed amorphous Selenium (a-Se); a group-6 chalcogenide glass. Though not the most utilized amorphous semiconductor material, its wide bandgap makes it a prime candidate for use in X-ray detection. Like other amorphous materials, it is full of localized energy states in the bandgap between the valence band mobility edge and the conduction band mobility edge. These localized states correlate not to injected impurities, as with doped crystalline devices, but rather to the innumerable structural defects within the structure of the glass. These localized states serve as trapping points where a drifting carrier can relax to a lower energy state. Depending on the depth of the trap, relaxation can be temporary, serving to modulate the current generated, or functionally permanent, attenuating the signal. As the carriers drift in and out of these trapping

states, the resultant drop in current flow can be computed as a functional reduction in the natural drift mobility of each species of carrier. The relationship between the energy levels and the respective concentration of energy states at those levels is illustrated with a *density of states* (DOS) profile. A number of studies have been used to establish the particular DOS of a-Se, but the highly stochastic nature of amorphous materials makes a mathematical description problematic.

The primary goal of this work is to create a computer simulation model of a generic amorphous semiconducting material under a high applied biasing voltage. In doing so, we replicate the process of photoinjection, and study how the charge carriers generated are propelled through the medium. Of particular interest is the simulation of high rates of carrier injection, comparable in total charge contribution to that created by the applied voltage across the sample, hereby referred to as the *injection ratio*. In amorphous semiconductor studies, injection ratio studies are generally overlooked because there is little application for such in commercial devices. This is because, typically, high injection ratios result in a distortion of the signal that such devices are designed to detect. Furthermore, injection ratios above unity can over-saturate the electric field, overwhelming the capacity of the field to propel all the charge carriers in the correct direction. This work will catalogue the effects of injection ratio testing by isolating the factors which govern the amount of spread in the carriers and identify what utility exists in doing so.

1.2 Applications in Radiography

Since their inception in 1896, X-ray devices have become a standard medical diagnostic procedure across the world. Though refinements to the process have mitigated the risk inherent in exposing patients to radiation, as of 2006, medical X-ray devices constituted 73% of medical

imaging procedures and 11% of the annual human radiological exposure[1] (See table 1-1). Exposure amounts of 50 to 200 microsieverts (μSv) are typical for single regional exposures, with recommended annual accumulation limit of 50 mSv per year[2]. The main hazards posed by excessive X-ray exposure include tissue damage from the high energy X-ray photons severing bonds in the DNA structures that govern tissue formation, killing cells directly, interrupting their reproduction leading to cellular death through apoptosis, or, more hazardously, mutating them into cancerous agents[3]. Consequently, finding means of reducing exposure without a corresponding decrease in device functionality is a topic of keen interest in radiological studies.

Table 1-1: Estimated number and collective doses from various categories of radiographic (excluding dental) and nuclear medicine procedures utilizing ionizing radiation (2006)

	Number of procedures (millions)	%	Collective dose (person-Sv)	%	Per capita (mSv)
Radiography	281	73	96,000	11	0.3
Intervention	17	4	129,000	14	0.4
CT	67	17	440,000	49	1.5
Nuclear Medicine	19	5	231,000	26	0.8
Total	384	100	896,000	100	3.0

The fundamental principles of X-ray diagnosis haven't changed since their initial use. High energy photons (~20keV to 60keV, depending on the application) are projected upon the patient's area of interest, say a damaged bone, which then pass through onto a detection screen on the other side. Absorption of X-rays by the body depends on the tissue type being irradiated, with softer tissues such as skin, fat, and muscles attenuating the incident X-rays at a lower rate than denser tissues such as bone or cartilage. The detection screen registers its own exposure to the X-ray light based upon the how the photons are attenuated by the tissue sample. The detection screen then translates it's exposure onto a readable format for a technician to evaluate. The variance in the absorption rates between tissues modulates the incident X-rays and creates

contours in the image that allow the technician to see underlying structures otherwise obscured (Figure 1-1).

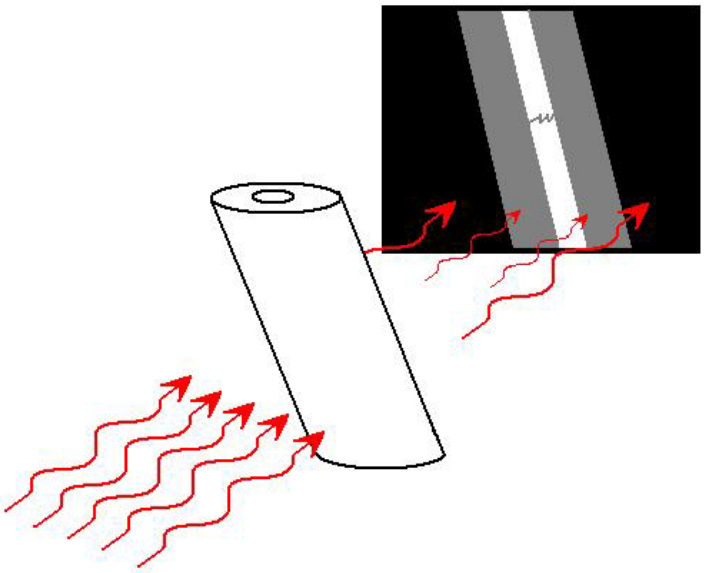

Figure 1-1 : X-ray attenuation though generic tissue sample.

1.2.1 Indirect Conversion Techniques

The most promising advances in X-ray diagnoses pertain to the detection screens; categorized as either a *direct* conversion or *indirect conversion* detector. In the majority of legacy devices in use in the field, the detector screen is basically unchanged from its original form; a photographic film sandwiched between two fluorescent plates. The fluorescent plates serve as intensifying screens by absorbing the high energy X-ray photons and spherically emitting a greater number of lower energy visible light photons which expose the film. This technique is a form of indirect conversion, since it relies on an intermediary process. Though widely used for reasons of economics, familiarity, and availability, this approach requires significant X-ray exposure on behalf of the patient; leading to the aforementioned primacy of medical imaging diagnostics in human radiological exposure. This technique also features the notable limitation of image resolution in that the fluorescent plates emit their visible wavelength photons in all directions, thus scattering the converted light across an area of film which is

proportional to the distance from the screen that the X-ray photon was absorbed (Figure 1-2). Thus, a thick intensifying screen suffers from higher incidence of image degradation. Conversely, a thin screen suffers from inadequate X-ray photon absorption. Typical screen thickness ranges between 100 – 200 µm.

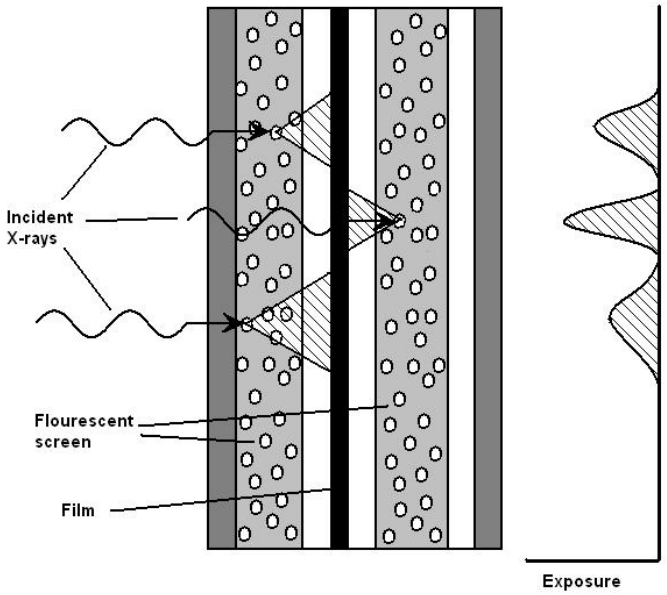

Figure 1-2 : X-ray film cartridge image dispersion

1.2.2 Direct Conversion Techniques

Advances in semiconductor technology, particularly in non-crystalline solids, have allowed for the development of medical imaging devices that do not require secondary processes to convert the X-ray light into a usable form. A number of materials exist which can provide for adequate conversion, but they all rely on a semiconducting layer which is responsive to X-ray radiation energy levels. This arrangement requires the use of an *active matrix array* (AMA) based device which is an aligned $M \times N$ grid of cells which are responsive to photons at X-ray wavelengths; each of which serves to translate its own accumulated exposure into an individual pixel of image. By this means, the resolving capacity of the detector as a whole is limited only by the sensitivity of the material and the size constraints of the pixel fabrication process.

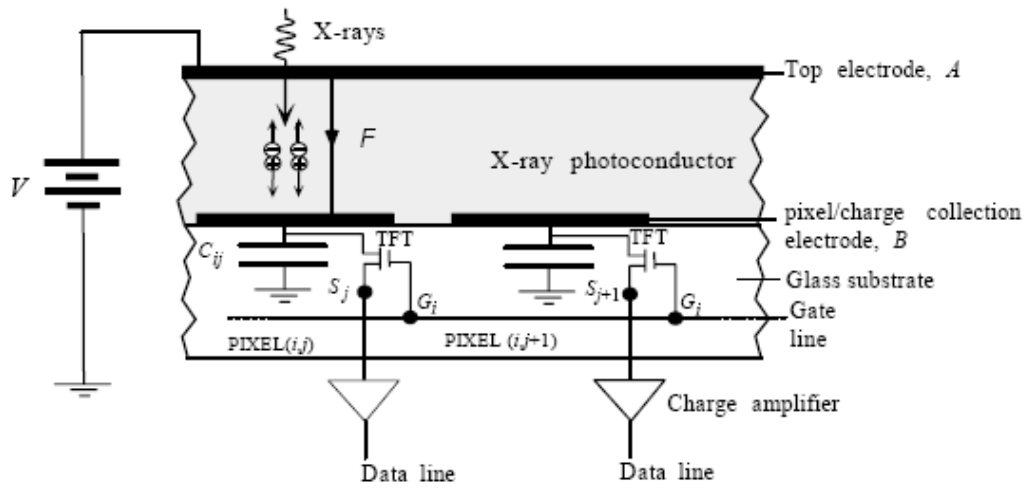

Figure 1-3 : Cross sectional schematic of a pair of AMA photo-detector pixels[4]

Device operation is generally universal and fairly simple. A semiconducting layer packaged between two electrodes is irradiated, as shown in Figure 1-3, which causes photoinduced generation of electron-hole pairs (EHPs) inside the bulk of the layer. A high biasing voltage is applied across the surface electrodes creates an electric field which separates the newly ionized charge carriers from each other and drifts them across the bulk to their respective destination electrodes, generating a photocurrent which places a signal charge in a local storage capacitor (each pixel in the detector array has a storage capacitor as shown in Figure 1-3). The amount of charge stored depends on the dose incident on each pixel (as attenuated by the irradiated tissue), the responsivity R and quantum efficiency η of the photoconductor, and the concentration of defect related trapping states inside the bulk of the semiconductor, which controls the charge collection efficiency. Upon completion of the exposure process, the individual pixels are addressed sequentially for their respective stored charges which are then stored digitally for translation into a usable image with the system as shown in figure 1.4.

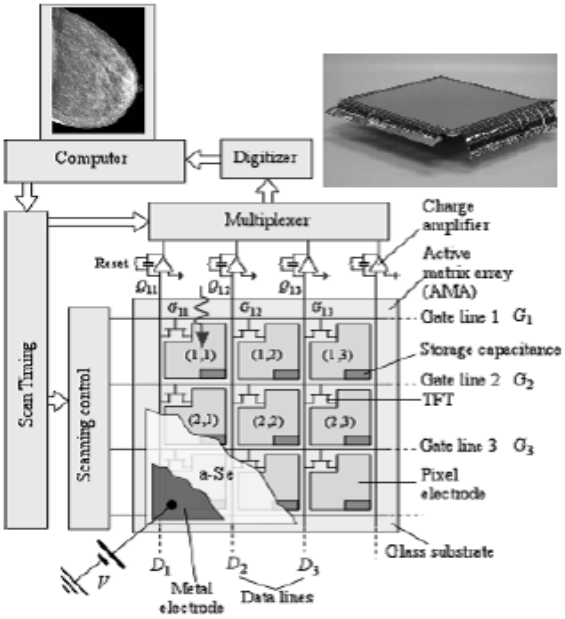

Figure 1-4: Sample of the substrate layer of an AMA photodetector screen showing the pixel grid and the charge polling electronics[5]

Injection ratio testing of such a device would involve replicating over-illumination of the device. Each electron and hole has a charge which disturbs the biasing field according to its polarity and position. Excessive injected charges will modify the electric field inside the photoconductor and distort the drifting rates, that is, the drifting velocities, of all charge carriers. In practical terms, we need to know the extent of dispersion of the injected charge carrier packet, and the longest time that is involved in the photoconduction process. The simulations in this work will help identify to what extent the charge carrier packet becomes dispersed as the injection ratio is increased. As will be shown, under high injection ratios, the extent of temporal dispersion of the charge packet can be much longer than the transit time; and dominate the time scale of collection.

In this work, dispersion is the primary metric used in evaluating the simulation results. By measuring the transit time spread of the photocurrent pulse, the expectation is that a comparable

analogue can be drawn to describe the shape of the carrier pulse, and we can thus assess how the multiple trapping mechanism of an amorphous semiconductor deteriorates charge collection efficiency, which directly impacts the viability of any particular material for practical use. One application directly related to the dispersion measurement is based on a Frisch grid[6] embedded in the bulk at a distance L_2 from the lower electrode. The grid shields the electrode from the electrostatic flux changes which generate the current. As carriers pass the grid, the electrode begins to register photocurrent according to the fraction of carriers that have passed. Dispersion modelling is key because Frisch grid detectors are designed to discriminate against the current produced by the slower charge carriers. Photons at X-ray energies exhibit absorption profiles which distribute carriers throughout the bulk, rather than at the surface, creating dual current sources. By isolating the current from the faster carriers, an improvement in the charge collection efficiency is observable[7], which translates into improved device sensitivity.

1.3 Application of Amorphous Semiconductors in Consumer Electronics

Aside from medical diagnostic use, amorphous semiconducting devices have also found use in the commercial sector. The fabrication qualities which make amorphous semiconductors – typically hydrogenated silicon (a-Si:H) in this case – desirable stem from the fact that they can be readily produced through *chemical vapour deposition* techniques. CVD fabrication works by reacting chemicals on the surface of a substrate wafer and controlling the reaction to leave a thin film of excess reactant, while the undesired reagents vaporize away. Monocrystalline solids can also be produced this way, but these have high growth temperatures which require a substrate which will not be damaged by the process. Amorphous devices can be fabricated by these means at temperatures as low as 75°C, which makes them suitable for deposition on to more delicate surfaces, including flexible polymers such as polyethylene terephthalate (PET)[8].

Unlike the photosensitive cells used in imaging, where the semiconductor is an electroded photosensitive bulk crystal designed to maximize absorption, the amorphous semiconductor used in these applications forms the conductive channels of arrays of FET *thin film transistors* (TFT), a variety of which are shown in Figure 1-5.

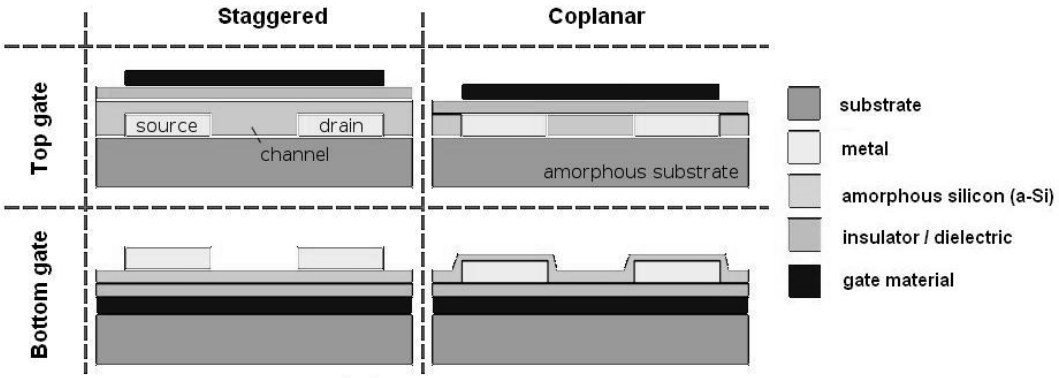

Figure 1-5: Schematic plans for a variety of TFT devices using amorphous silicon for the channel.[9]

The nature of amorphous semiconductor devices of this type are based on the field effect, and their models are quite different from those involved in photoconduction. FET type devices do not operate on injected charges, but rather by using electric fields at the gate electrode to generate conductive channels in otherwise non-conductive materials.

1.4 Applications in Photovoltaic Cells

Photovoltaic cells are much like the imaging devices described above, but with a different geometry, sensitivity, and operation scheme. Firstly, the architecture uses a *pn*-junction of doped hydrogenated amorphous silicon (a-Si:H) with a bandgap of 1.8eV, making it responsive to much of the range of visible and infrared illumination which constitutes the majority of solar output. One of the most important reasons for the use of a-Si:H in solar cell applications is that it can be doped both *n* and *p*-type and the doped material has a high conductivity. This is not the case

with a-Se, which cannot be doped as readily as a-Si:H. Even when doped, the conductivity of a-Se is still very low, which leads to a high series resistance in the solar cell; highly undesirable. There are other distinct differences between imaging devices and solar cells in terms of their material requirements. For example, the lack of a resolution requirement negates concern of crosstalk between neighbouring cells. Further, digital imaging AMA devices operate on short finite bursts of X-ray or laser illumination. In the X-ray detector, the finite illumination translates to a finite transient photocurrent with features that are characteristic of the material and the operational parameters. In a photovoltaic cell, the operational terms involve steady state (dc-like) exposure meant to generate a sustained photocurrent.

Taken as a special application of the X-ray detector, illumination can be treated as a constant rate of EHP injection which steadily rises from zero until collection begins. Equilibrium is reached when the collection rate equals the injection rate in spite of the effects of trapping. A constant collection rate equates to a constant drift rate proportional to the ratio of the average drift velocity to the bulk thickness. Injection testing at this equilibrium point can be performed two ways in these devices; first as an impulse injection of extra EHPs to evaluate the transient response, and second as a protracted elevation of the illumination level to examine the efficiency of the detector and the saturation point beyond which no additional current is generated.

Though crystalline photocells can be manufactured and enjoy the best energy efficiency for the same illumination, the monocrystalline fabrication process is highly expensive, which limits their widespread use. An amorphous device is inexpensive and flexible, but suffers from performance degradation. The US Department of Energy reports that a-Si:H photocells have an initial efficiency around 10.5%, with a 1.5% efficiency loss after 585 hours of light soaking[10]. Though not properly understood, the efficiency loss, labelled as the Staebler-Wronski effect, is

largely a product of increases in the defect concentration due to bond structure degradation. This rise in defect abundance correlates to a reduction in the maximum effective photocurrent.

1.5 Summary of work

This work is separated into 5 chapters. Chapter 2 will outline the principles behind photoconduction in both crystalline and amorphous semiconductors, as well as provide detail on the *time of flight* transient photoconductivity measurement methods used. Chapter 3 contains a comprehensive overview of the ability of the simulation software to perform as required, a description of the testing model to be used, and a detailed listing of the test plan with expectations. Chapter 4 contains the results of each segment of testing listed in Chapter 3, including the output TOF waveforms, electric field responses, histograms to track the progress of carrier test packages, and, where interesting, dispersion measurement comparisons. The final chapter contains the most relevant observations made in this work, as well as some possible implications. It also outlines in what ways the model can be further enhanced, and how it the simulations can be applied to real world problems involving amorphous devices.

Chapter 2 Transient Photoconduction

2.1 Introduction

Photoconduction is the process by which electron flow can be induced by projecting photons of particular wavelengths at a particular conducting medium so as to cause electrons, through photoabsorption, to ionize completely from their host atoms, thereby generating electron-hole pairs (EHP) in the conducting medium. Semiconductor materials are preferred because the poor natural conductivity creates a useful impediment to direct electrical conduction between biasing electrodes, thereby allowing us to apply an electric field to both facilitate and isolate charge carrier drift, and thus its respective current, to that of the EHPs generated by photoabsorption.

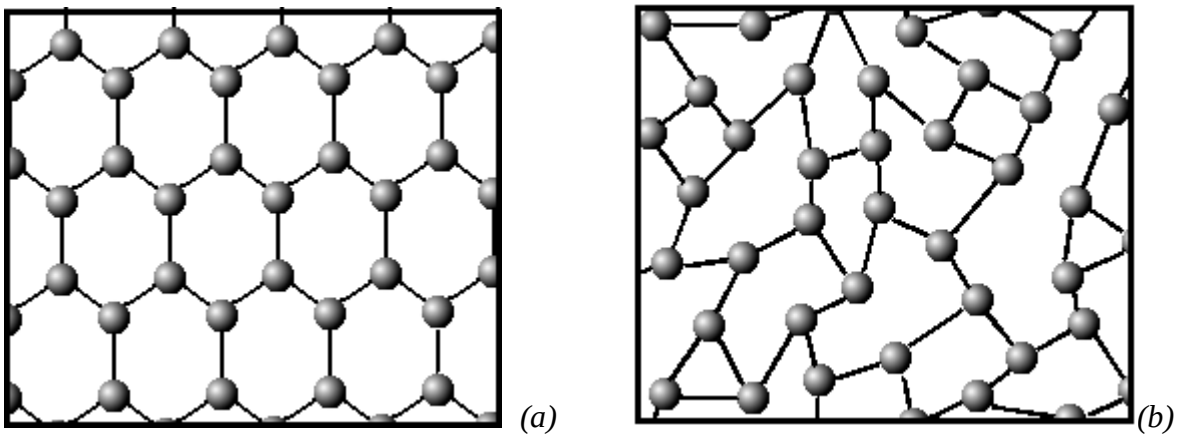

(a) *(b)*

Figure 2-1: Semiconductor materials as classified by the periodicity of their atomic lattice structure (a) Long Range Order - crystalline (b) Short Range Order - amorphous

Semiconductors, as with any solid material, can be classified into two primary categories: monocrystalline, and amorphous. The distinction between the two is the structural relationships between their component atoms. These structural relationships are identified as *Long Range Order* (LRO) and *Short Range Order* (SRO). Crystalline solids are recognized by their long range order. This indicates that a structural periodicity exists throughout the bulk of the material in question. This periodicity creates a material which behaves in an inherently predictable

manner. A variant on crystalline structures is poly-crystalline structures where the bulk is a composite of non-aligned crystalline structures. By contrast, amorphous materials lack the periodicity of crystalline structures. This is manifest as short range order, in which structural similarities between component atoms exist only within the immediate vicinity of any particular molecular sample. This lack of periodicity creates an inherent unpredictability in the flow characteristics of the amorphous sample. This unpredictability invariably complicates the modeling of the carrier flow.

2.2 Photon Absorption and Generation

Photonic energy incident on any material imparts some or all of its kinetic energy into that medium. In semiconductor physics, this absorption of energy is used to completely ionize electrons from their outermost energy shell into the bulk of the material. In doing so, we create two charge carriers; the promoted electron and the vacancy that it once occupied. Factors determining how well photonic energy is absorbed into a semiconductor include the type of bandgap, the thickness L of the irradiated sample, the wavelength of incoming photons λ, the corresponding penetration depth $\delta(\lambda)$, and the quantum efficiency $\eta(\lambda)$. These factors combine to the responsivity $R(\lambda)$, the measurement of output current per unit of input power computed in amps per watt.

In crystalline devices, R is typically measured from the generated photocurrent and derived from η, which is defined as the number of free EHPs generated for each incident photon. Amorphous devices complicate this relationship because the bandgap localizations create a quasi-resistive mesh in the bulk of the material which inhibits the net carrier drift, and thus modulates the current used to define R. Typically, R is measured as:

$$R = \frac{I_{ph}}{P_o} \qquad (2\text{-}1)$$

where I_{ph} is the generated current and P_o is the incident optical power. By comparison, η is:

$$\eta(\lambda) = \frac{\text{Generated EHPs}}{\text{Incident photons}} = \frac{I_{ph}/e}{P_o\lambda/hc} \qquad (2\text{-}2)$$

Because of the trapping effects in amorphous devices, I_{ph} does not adequately reflect the number of carriers generated, and so must be multiplied by a factor representing the ratio of trapped to drifting carriers. Furthermore, where I_{ph} varies with time, as is the case with transient studies and elevated injection rates, it becomes impractical to try to measure the responsivity in the conventional way.

2.3 Time of Flight simulation

Simulations based on measuring the transient drifting time of carriers under an applied field are useful for estimating the microscopic mobility of both carrier types in a semiconductor. Tests which measure the traversal time of the drifting particles across a medium are referred to as *Time of Flight* (TOF) simulations. In these tests, absorption depth is minimized to ensure a unipolar test carrier set, and biasing charge polarity is used to select the preferred carrier species. Under a known applied field, each carrier type exhibits a species specific transit time t_T to drift from $x=0$ to $x = L$ which is used to identify the corresponding mobility.

Because drift is uninterrupted in their testing, crystalline TOF experiments provide useful baseline values for microscopic mobility estimates. In amorphous or polycrystalline devices, since the carriers drift in and out of variable depth traps for a finite period of time determined by the thickness of the specimen device, the terminating conditions for carrier flight need to be reconsidered. As they can be considered as repeatedly terminating in localizations, the flight

time is necessarily based on the respective carrier lifetimes – a function of the local state concentrations - rather than their transit time. Individual materials are characterized by their carrier *Schubwegs*, the measurement of the average drift distance preceding deep trapping.

Given the sporadic movement of the carriers - full speed while free but immobile while trapped – the adjusted mobility is highly dependent on the interchange rates of capture and release. The adjusted transit time $t_{T_{mod}}$ is separable into free and trapped times; free time being equal to the trap free transit time t_T and trapped time being equal to $N \times \tau_r$, where N is the average number of trapping events. The average trapping count is simply the trap free transit time t_T divided by the average capture time τ_c. This is given as:

$$t_{T_{mod}} = t_T + \frac{t_T \cdot \tau_{r(release)}}{\tau_{c(capture)}} = t_T \frac{\tau_c + \tau_r}{\tau_c}$$

which simplifies to: $t_{T_{mod}} = \frac{t_T}{\theta}$ where: $\theta = \frac{\tau_c}{\tau_c + \tau_r}$ *(2-3)*

Equation 2-3 introduces θ, the mobility reduction factor which is the fraction of the capture time as part of the total trapping cycle time. This factor is dependent on trap concentration (due to τ_c) and trap depth (due to τ_r), against which the localization concentrations are variable, and thus is material specific. This factor dictates the increase in transit time and, by extension, the adjustment to the mobility and the fraction of total present carriers moving at any given time, which yields the photocurrent as a fraction of the maximum potential current.

2.4 Injection ratio

The main goal of this work is to evaluate how the TOF transient photocurrent curve generated in the simulations is responsive to increases in the amount of incident illumination.

Low injection is regarded as a case where the total electric field created by charges injected through photoabsorption is much less in magnitude than that of the applied field. High injection cases are typified by being comparable to the applied field, such that the field is disturbed and the flow rates of the moving carriers are impacted. Injection rates creating fields exceeding the applied field push carriers back into the near electrode, quickly returning the remaining injection ratio back to unity, as illustrated in Figure 2-2.

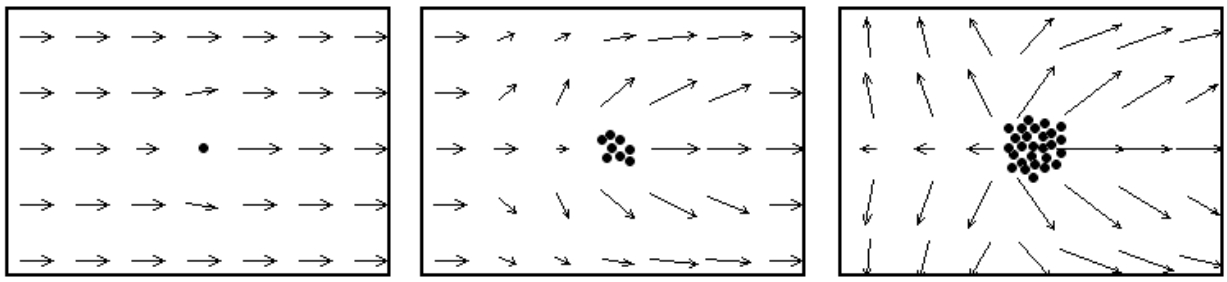

(a) *(b)* *(c)*

Figure 2-2: Example of how the presence of foreign charges might interfere with the electric field across the medium. Cases shown are (a) low injection, (b) high injection, and (c) saturation.

Unlike the biasing field, which is unidirectional along the *x*-axis, the spherical field created by each carrier either hinders or enhances the *x*-direction drift speed of neighbouring carriers, depending on their relative position. In non-imaging injection studies of the material, the geometry of the device is of less import than with AMA imaging devices. Under low injection, the lateral spread of the carriers due to repulsive effects is nominal, but under high injection, the amount of lateral spread leads to image degradation due to increased crosstalk between neighbouring pixels as the carriers redistribute themselves across the bulk in the *y* and *z* directions; irrelevant where imaging quality is of no concern. The injected charge ratio is established by estimating the number of electrons photogenerated N_{EHP} and using:

$$r = \frac{Q_{inj}}{Q_0} = \frac{Lq_e N_{EHP}}{V\varepsilon_0\varepsilon_R} \qquad (2\text{-}4)$$

2.5 Photoconduction

Once generated, two primary mechanisms exist which drive movement of free carriers. The first, diffusion, is a stochastic process by which carriers move randomly in all directions due to their thermal vibrations. On an individual level, no particular change is typically seen, but in large scale systems involving millions of individuals, diffusion results in redistribution of carriers across the sample area from highly concentrated regions local to points of carrier injection into a uniform distribution across the bulk. The other mechanism is drift; locomotion resultant of an electric field which impels carriers in the conduction band along the direction of the field via electromotive force.

2.5.1 Diffusion

Diffusion is the migration of charge carriers down the carrier concentration gradient via thermally activated motion. Fick's first law, given in equation 2-5, describes the proportionality between the particle flux Γ and the concentration gradient dn/dx as being dependent on the diffusion coefficient D. These coefficients D_e and D_h describe the rate of carrier movement according to the lattice temperature and the microscopic mobilities, μ_e and μ_h, of each carrier type as shown in Equation 2-6.

$$\Gamma_e = -D_e \frac{dn}{dx} \qquad (2\text{-}5)$$

$$D_e = \mu_e \frac{kT}{q_e} \qquad D_h = \mu_h \frac{kT}{q_e} \qquad (2\text{-}6)$$

The current generated through carrier diffusion is limited at best. Diffusion related carrier movement is three dimensional, tends to be Gaussian in nature, and drives both carrier types

according to the same conditions, negating much of what current is produced. Carriers diffuse down the concentration gradient because the movement statistics are the same for each individual, and statistically, there are more carriers available in the high concentration regions to diffuse out than there are carriers in the neighbouring low concentration regions to diffuse in. Assuming the highly concentrated region is near a device boundary, as is the case with low absorption depth illuminations, carrier diffusion will trend in one direction, but the injection boundary is typically electroded with a metal, which easily absorbs both holes and electrons and as such serves as a collection point for removing free carriers from the bulk.

2.5.2 Field Assisted Drift

Of greater relevance to this work is drifting of carriers due to the force exerted by an applied electric field. Here, the average movement of carriers is along the lines of the electric field, with drift direction being dependent on the polarity of the carrier with respect to the direction of the field; notably, this opposing drift increases the generated photocurrent. The microscopic mobility μ of the carriers is the measure of the mean drift velocity per unit of applied electric field, and is dependent of the prevalence of events which impede carrier movement. In crystalline materials, this impediment is due solely to scattering by collisions with atoms in the lattice[1]. In amorphous devices, the structural irregularity creates an abundance of potential wells of varying depths which serve to trap or deflect drifting carriers. To assess the mobility reduction resultant of these localizations, it is necessary to compute it as a factor of the microscopic mobility corresponding to the device's crystalline counterpart.

[1] Note, these are not impact collisions with atoms per se, but rather scattering by effects such as bending of the carrier flight paths due to proximity with the potential wells of the atoms.

From initial generation, carriers create current by eliciting work from the biasing voltage by moving either with or against the applied field, as guided by polarity. Using L as the bulk thickness, l as the initial generation depth, the amplitude of current for each EHP is given by *Ramo's theorem* as detailed in Eq 2-7,2-8, and 2-9. Ramo's theorem posits that current is produced by electron movement as a consequence of instantaneous change in the electrostatic flux lines on the electrode, rather than from received charges per unit time[11]. Integrating both hole and electron currents from t = 0 to their transit times yields a net collected charge of q_e; provided both carriers reach their respective destination electrodes.

$$i(t) = \begin{cases} {}^{e\nu_h}/_{L} \,; t < t_h \\ 0 \quad\quad ; t > t_h \end{cases} + \begin{cases} {}^{e\nu_e}/_{L} \,; t < t_e \\ 0 \quad\quad ; t > t_e \end{cases} \qquad (2\text{-}7)$$

where:

$$\nu_e = \mu_e E(x) \quad , \quad \nu_h = \mu_h E(x) \qquad (2\text{-}8)$$

and:

$$t_e = \frac{L - l}{\nu_e} \quad , \quad t_h = \frac{l}{\nu_h} \qquad (2\text{-}9)$$

The current generated by the movement of the carriers is greater than that of diffusion first because it is unidirectional and second because the field is capable of moving carriers much more efficiently and with no loss due to collection at the wrong electrode, as per figure 2-3.

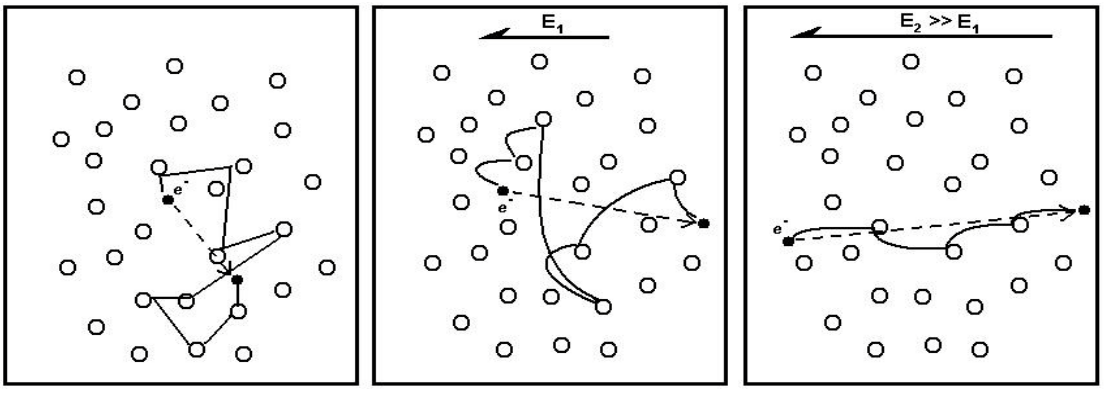

Figure 2-3: Simplified examples of diffusion and field assisted drifting. As the applied field increases, the diffusion movement becomes less pronounced against the drift movement. The diffusion rate doesn't change, but the carrier has much less time to diffuse.

Since diffusion motion is omnidirectional, its contribution to the photocurrent is negligible. As a dispersive mechanism it must be quantified against the alternative mechanisms of multiple trapping and coulombic repulsion. Using electrons as the carriers, the *x*-axis mean change of distribution, Δx_{rms}, as caused by diffusion is given as double that of Eq. 2-6:

$$\left(\Delta {x_{rms}}^2\right)_{Diff} = 2D_e \frac{L}{\mu_{e0} E_0} = 2 \frac{kT}{q_e} \frac{L}{E_0} \qquad (2\text{-}10)$$

Prior work by Schmidlin[12] on monoenergetic multiple trapping shows that the transit time variance of the carriers in the pulse is describable with:

$$\Delta t_{mt}^2 = \frac{2\tau_r^2 L}{\tau_c \mu_{e0} E_0} \qquad (2\text{-}11)$$

Assuming that capture time τ_c is sufficiently less than release time τ_r such that $\theta \approx \tau_c/\tau_r$, and knowing that θ relates the microscopic mobility μ_{e0} and the effective mobility μ_e by $\theta = \mu_e/\mu_{e0}$, equation 2-11 simplifies to:

$$\Delta t_{mt}^2 = \frac{2\tau_r L}{\mu_e E_0} \qquad (2\text{-}12)$$

The transit time spread Δt_{mt} relates to the spatial spread Δx_{rms} by:

$$(\Delta x_{rms})_{mt} = \Delta t_{mt} \mu_e E_0 = \left(\frac{2\tau_r L}{\mu_e E_0}\right)^{\frac{1}{2}} \mu_e E_0$$

so:

$$\left(\Delta {x_{rms}}^2\right)_{mt} = 2\tau_r L \mu_e E_0 \qquad (2\text{-}13)$$

Comparing equations 2-10 and 2-13 and simplifying, the first dispersion ratio – trapping spread to diffusive spread – is given with:

$$r_{m-d} = \frac{\Delta x_{mt}^2}{\Delta x_{diff}^2} = \frac{q_e \tau_r \mu_e {E_0}^2}{kT} \qquad (2\text{-}14)$$

The rms spread due to carrier coulombic repulsion is subject primarily to the ratio r of injected charge Q_{inj} to the applied charge Q_0. Assuming a Gaussian shape to the carrier pulse, $(\Delta x_{rms})_{cr}$ will correspond to the distance of one standard deviation σ in each direction, where the net portion of injected charge repelling carriers away from the center of the pulse is equal to 0.682 of the total injected charge. The drift velocities at $\pm\sigma$ are given with:

$$v_{e(\pm\sigma)} = \big(E_0(1 \pm 0.682r) + C_E(t)\big)\mu_{e0} \qquad (2\text{-}15)$$

where $C_E(t)$ is the uniform field integration constant which keeps the total field at E_0. So, factoring out the uniform field components $E_0 + C_E(t)$, which governs the drift velocity of the carrier pulse peak, the total spreading rate between $-\sigma$ and $+\sigma$, Δv_e, is:

$$\Delta v_e = 1.364 r E_0 \mu_{e0} \qquad (2\text{-}16)$$

which, over the transit time, allows a spread distance Δx_{cr} of:

$$(\Delta x_{rms})_{cr} = 1.364 r L$$

and thus:

$$(\Delta x_{rms}^2)_{cr} = 1.86 r^2 L^2 \qquad (2\text{-}17)$$

giving us our second dispersion ratio from eqs. 2-10 and 2-17 as:

$$r_{c-d} = \frac{\Delta x_{cr}^2}{\Delta x_{diff}^2} = \frac{0.930 r^2 q_e E_0 L}{kT} \qquad (2\text{-}18)$$

The most relevant variables in these ratios are the capture time, the electric field, and the injection ratio. For evaluating the dispersion ratios, we use baseline values of L = 100μm, μ_e = 1×10^{-4}cm^{2}V^{-1}s^{-1}, and T = 300K. Table 2-1 lists some sample dispersion ratio calculations using these parameters. The reference evaluation uses release time τ_r of 10ns, applied field E_0 of

10V/μm, and an injection ratio r of 1%. This returns dispersion ratios of $r_{m\text{-}d}$ =3481 and $r_{c\text{-}d}$ = 3.6. The high trapping to diffusion ratio shows comparably negligible dispersive contribution from diffusion. A much lower applied field brings the ratio below 35, but all testing in this work is done at 10V/μm, so this is not applicable. At low to medium injection, the repulsion dispersion is comparable to diffusion dispersion, but only because both are negligible against the trapping dispersion. Under high carrier injection, the primary dispersive force changes from multiple trapping to the coulombic repulsion, while the diffusive component remains trivial. Since the diffusive component is so small in the relevant parts of testing, for brevity, it is excluded in this work.

Table 2-1: Dispersion ratios as computed for L=100μm, $\mu_e=10^{-4}cm^2/Vs$, and T =300K.

Capture time τ_r (s)	Applied field E_0 (V/μm)	Injection ratio r	$\frac{\Delta x_{mt}^2}{\Delta x_{diff}^2}$	$\frac{\Delta x_{cr}^2}{\Delta x_{diff}^2}$
10×10^{-9}	10	0.01	34814	3.60
20×10^{-9}	10	0.01	69628	3.60
5×10^{-10}	10	0.01	17407	3.60
10×10^{-9}	1	0.01	348.14	0.36
10×10^{-9}	20	0.01	139256	7.20
10×10^{-9}	10	0.0001	34814	0.00035
10×10^{-9}	10	0.50	34814	8993

2.6 Applicable materials

There are a number of useful semiconductors for photodetection; the type depending on the application. A number of polycrystalline materials include mercury iodide (p-HgI_2), cadmium zinc telluride (p-CdZnTe – CZT for short), lead iodide (p-PbI_2), and lead oxide (PbO). Amorphous semiconductor materials include hydrogenated silicon (a-Si:H), alloyed selenium (a-Se:Cl), and indium germanium zinc oxide (a-IGZO). A limited selection of commonly used materials is listed in Table 2-2 along with electrical properties which are pertinent to TOF

simulations. Each material has a unique density of states which, when illuminated by photon in the responsive wavelengths, exhibits a characteristic transient photocurrent curve.

Table 2-2: Sample electrical properties of a few semiconducting materials.

Material	Dielectric breakdown field V_b (V cm^{-1})	Bandgap E_g (eV)	Electron mobility μ_e (cm^2 V^{-1}s^{-1})	Hole mobility μ_h (cm^2 V^{-1}s^{-1})	Electron diffusion D_e † (cm^2 s^{-1})	Hole diffusion D_h (cm^2 s^{-1})
a-Se	7×10^5	2.2	0.001	0.1	0.00003	0.003
c-Si	3×10^5	1.1	1400	450	36	12
p-CZT	5×10^5	1.4-2.2††	1120	27-66	28	1.2
a-IGZO	4-8 $\times 10^5$	~3.0	23.8	0.15	0.6	0.004
p-PbI_2	5-8 $\times 10^5$	2.3	65	20	1.7	0.5

† - diffusion values are as estimated for room temperature T = 300K
†† - CZT bandgap varies with material composition

Experimentally, the photocurrent waveforms can be used to derive low resolution estimations of the DOS of the materials under study. This is done mathematically through a Laplace transformation of the photocurrent waveform[13]. Since the waveform does not conform to a readily definable function, the current is approximated across N sample times, with the output transformed to produce an effective discrete reparameterization of the time domain signal. Factoring in parameters such as listed in Table 2-2, the device geometry, and the injected charge magnitude, the method returns a loose approximation of the material DOS such as shown in Figure 2-4(a) to (c). The DOS itself is given by:

$$g(E_0) = \frac{1}{\sigma v k T}\left\{\frac{d}{d\ln(s)}\left[\frac{I(0)}{\hat{I}(s)}\right] - s\right\} \qquad (2\text{-}19)$$

where: $I(0) = qn_0\mu_0 F$

and: $\hat{I}(s) = \sum_{j=2}^{N-1} I(t_j)e^{-t_j s}\left(\frac{t_{j+1} - t_{j-1}}{2}\right)$

where σ is the capture cross sectional area, v is the thermal velocity, and n_0 is the initial carrier density. Since this approach is based on reparameterizing the transient photocurrent, which is

based on unipolar charge transport, it is useful for estimating bandgap state concentrations for both carrier types.

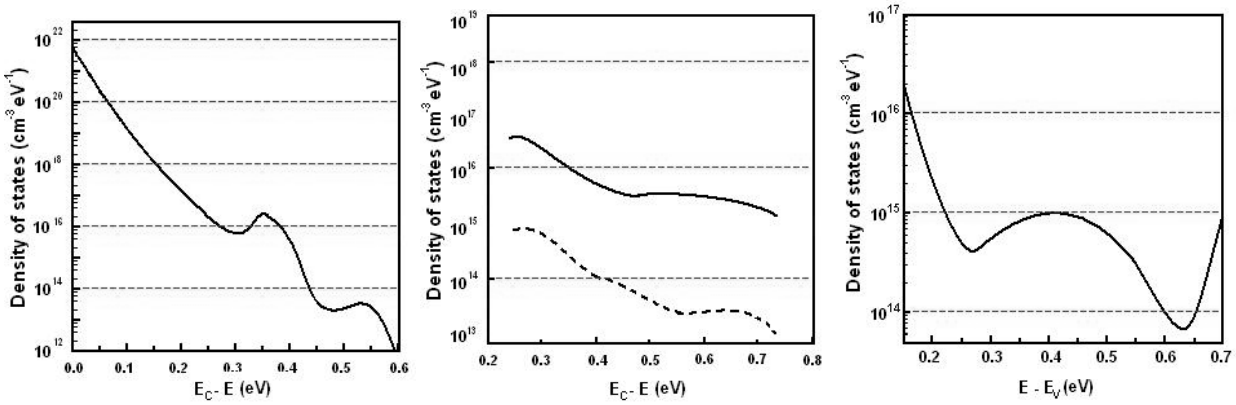

Figure 2-4: Sample mid-gap DOS acquired through Laplace transform analysis. Models shown are of (a) amorphous selenium[14], (b) hydrogenated amorphous silicon[15] (dashed plot applied Tikhonov regularization to compute) and (c) polycrystalline CZT[16] (also using Tikhonov regularization)

2.7 Summary

This chapter provided a brief overview of the principles underlying the work. We reviewed the material classifications and their significance. We reviewed the basics of the photoabsorption, and how the energy transfer of semiconductor irradiation was related to the quantum efficiency and responsivity specific to material types. Time of Flight simulation as applied to trap limited transient photocurrent modelling was described, and the mobility reduction factor θ was introduced and derived. Injection ratio was briefly discussed, including how the high injection ratio distorts the surrounding electric field. We briefly reviewed the two primary mechanics which drive free carrier motion in an illuminated semiconductor, as well as how they were applied in simulation to develop a photocurrent calculation procedure. We also identified three main dispersion causing factors and estimated the value of their inclusion to this work. Finally, a few examples of photodetecting semiconductors were identified, their relevant electrical properties listed, and the mathematical technique used to estimate their DOS profiles based on their properties and their transient photocurrent curve was summarized.

Chapter 3 Monte Carlo Simulation

The primary focus of this work is to establish a viable modelling platform for simulating high carrier photoinjection in semiconducting materials with a focus on the effects of disturbing the applied electric field. Creating a viable model for the flow of carriers through such a material requires that as many factors as possible be simulated. Experiments for this work are conducted using Monte Carlo computer simulations. Using MATLab as the computing language for its built-in library of statistics and data processing functions, this work will demonstrate that the effect of high charge injection creates distinct dispersive effects upon the photoinjected discharge current, which can be combined to predict the expected dispersion in experimental samples. This will be done through a sequence of progressive steps designed to isolate the factors which contribute to carrier dispersion in the photoinjected discharge current and gauge the effect of increasing the charge injection ratio applied to each.

3.1 MATLab functionality

In order to demonstrate the validity of the model under consideration, we must first validate the computing software used in its realization. MATLab is, at core, a versatile mathematics engine with a built-in visualization utility. It features a programmable interface that interprets algorithmic code with a primary focus on matrix operations and plotting, a symbolic computing engine, and the capacity to interface with compiled programming languages. The benefit of this is that when resource intensive code is required, a faster compiled version can be applied to expedite the process. As MATLab is an interpreted computing language, it simply isn’t designed for speed in highly repetitive computations, and is best suited to leaving such tasks to compiled code.

For purposes of simulating TOF carrier flow through a definable medium, the primary functions of interest are in the statistics functions available to MATLab, and the data processing used in evaluating the end results from the testing. Both of these features must be adequate to the task of producing outputs consistent with the expected stochastic behaviour of TOF carrier flow. To simulate photoinjected discharge, we need to be able to reliably replicate the events of generation, carrier trapping, and carrier release. The process of generation is based firstly on the illumination time – a Gaussian distribution based on the illuminating laser pulse duration - and secondly on absorption depth – an exponentially distributed variable based first on the Gaussian distributed wavelength of the illuminating photons λ and its corresponding absorption depth $\delta(\lambda)$. Trapping time is calculated based on an exponential distribution which is dependent on the concentration of traps in the bulk of the sample. As it is impractical to compute this on a spatial level, we compute trapping time based on the expected drift lifetime of the carrier. The release event is a thermally activated process based on the Maxwell-Boltzmann energy distribution, so to estimate the time for release, we evaluate a time based on an exponential distribution using the depth of the trap from the level of the conduction band energy E_C.

Thus, the statistics functions must be able to produce millions of unpredictable and non-repeating outputs based on the uniform, Gaussian, and exponential random number distributions. In MATLab, the outputs of the random number generator RAND(M,N) creates a matrix of $M \times N$ pseudorandom numbers based on a 35 element vector capable of generating random numbers between 2^{-53} and $1\text{-}2^{-53}$; a range theoretically capable of generating 2^{1492} unique numbers distributed uniformly. Notably absent in this range are ‘0’ and ‘1’, though these could be synthesized if there existed any utility in doing so. The Gaussian random number generator RANDN(M,N) creates an $M \times N$ sized matrix based on a normal distribution with mean of zero,

variance of one, and standard deviation of one. The exponential random number generator function EXPRND(μ) creates a single output *y* based on the input mean μ and the output *x* of the uniform number generator passed through the following:

$$y = -\mu \cdot \log(x)$$

With a capacity for generating outputs with precision up to 16 decimal points from the range boundaries [0,1], the considerably high resolution of the output range for the built-in random number generator far exceeds the practical requirements for testing of this nature.

For analysis, the tools used are a dispersion calculator which measures the spread using the *Full Width – Half Maximum* (FWHM) of the derivative function of the TOF waveform and a smoothing procedure which will permit the dispersion calculations to be automated, facilitating a more readable measurement of the carrier spread. Though it does distort the raw data of the simulated test result, the section most affected is typically outside the area where dispersion is computed from. The smoothing procedure is performed using first a built-in moving average function, then secondly a 1:100 sampling of the averaged data, and thirdly a custom built moving average function built to isolate the collection peaks. The immediate concern of this procedure, as mentioned prior, is that the distortion of the raw data by the smoothing procedure will provide skewed results which don't reflect the reality of the actual test. To allay this concern, it must be demonstrated that the smoothing procedure does not interfere with the pertinent parts used in analysis of the output. This requires that we identify the source which necessitates the smoothing procedure, which stems from the considerable amount of signal noise inherent to the limitations of Monte Carlo testing.

In the interests of timely test performance, we artificially limit the number of carrier test packages to be simulated to a modest *N* = 10,000, and then assign a scaling value to it so that the

total injected charge can be dictated as a ratio r of the total biasing charge. In doing so, we can investigate the effects of varying the injected charge by directly controlling the injection ratio. The scale is the number of carriers represented by each package and is determined as follows:

$$scale = -\frac{\varepsilon_0 \cdot \varepsilon_R \cdot V \cdot r}{L \cdot q_e \cdot N} \qquad (3\text{-}1)$$

where L is the thickness of the sample, ε_R is the material relative permeability, and q_e is the electron charge. The immediate problem that arises from this small package count is that when the ratio of the trapping rate to the release rate, θ, is in the range of 10^{-3}, the number of event transitions per time step becomes comparable to the number of carriers drifting, thus, each individual state transition exhibits a more pronounced influence on the current for the time step. Increasing the package count inversely modulates the scaling factor while maintaining the overall injection ratio, resulting in more drifting carriers exhibiting proportionally reduced influence on the photocurrent. This, in turn, results in a smoother curvature in the photocurrent profile. Presumably, as the scale approaches unity, the photocurrent profile curvature should much more closely resemble that of the profile as created by the smoothing procedure.

To confirm this expectation in testing, we must run concurrent tests where the only variables are the carrier package counts and their respective scaling factors. The test used for this is the same as used in the next parts, but performed for counts of N = 10,000, 50,000, and 100,000 packages and using deep capture time t_{cd} of $3t_T$, shallow capture time t_{cs} of $0.01t_T$, and mobility reduction θ of 0.01. These are then compared against the processed result from the test with the highest expected noise. The results of these tests are shown in Figure 3-1 and Figure 3-2**,** which clearly illustrate how the photocurrent noise converges toward a processed output that remains unchanged as the package count is increased. Note that the discrepancies at each end of the

processed outputs are artefacts of the moving average filter, on account that all carriers are moving only in the very first steps of the simulation, which falls to ~0.1% of the initial full current within a few steps, owing to the very low thermalization time.

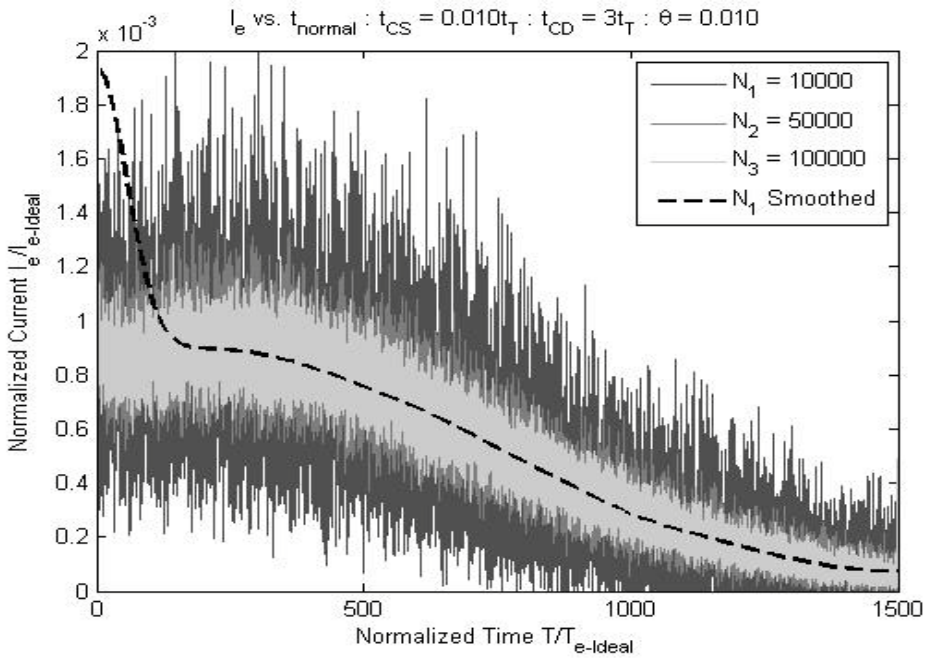

Figure 3-1: Package count test results vs. processed result

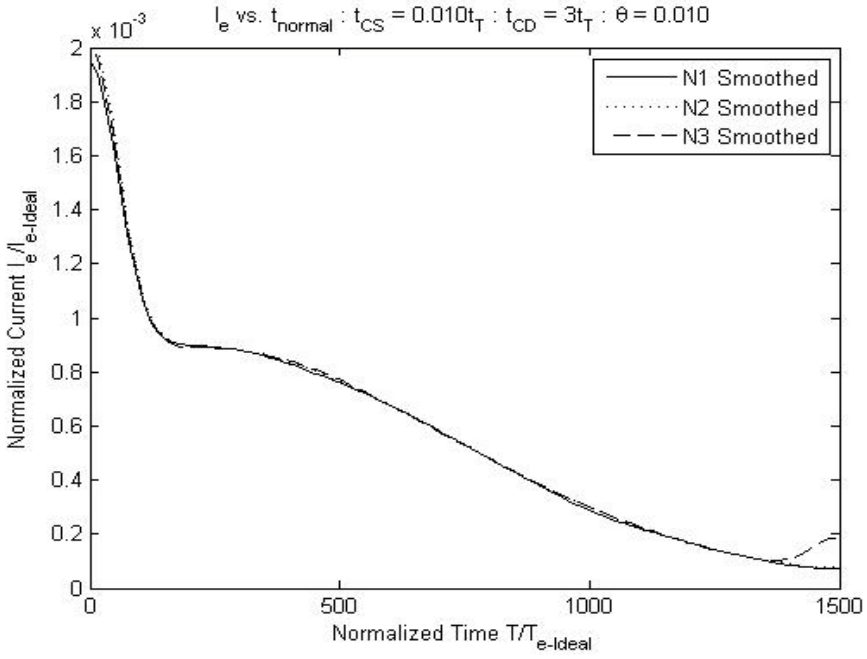

Figure 3-2: Processed package count test results

3.2 Methodology – Test plan

Simulations for this work will be performed in two primary phases. The first phase will serve to emulate a generic crystalline semiconductor with easily definable properties. In the absence of trapping states, we'll most clearly identify the two direct effects of high charge injection: electric field perturbation which alters the current flow, and high mutual repulsion between artificially large charge packages which manifests as a contributory dispersion factor. The second phase will incorporate the localized states that are abound in amorphous semiconductor devices. This will be an idealized test set which will reveal the relationships between capture time τ_C, capture/release ratio θ, and injection ratio r. Furthermore, this set will model multiple levels of trapping states, so as to help clarify the relationship between each to the dispersive effect of elevated injection

3.2.1 Phase One – Generic Crystalline Semiconductor

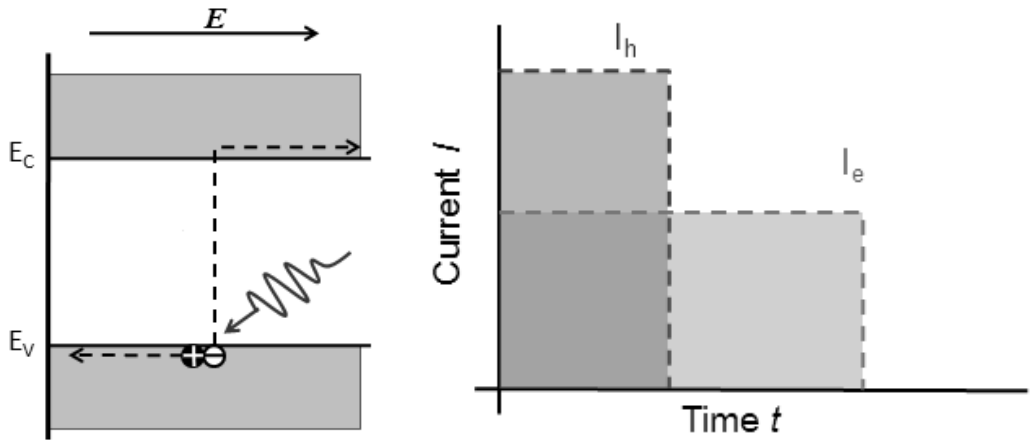

Figure 3-3: Energy band diagram and Time of Flight waveforms for an individual photogenerated EHP in crystalline material assuming $\mu_h > \mu_e$

This phase of testing will establish the effect of high carrier injection as applied to each behavioural factor in crystalline TOF simulation, as illustrated in Figure 3-3, and in doing so; highlight the artifacts which result from the applied simplifications in the modeling process.

This is done by isolating each dispersion causing factor and measuring the magnitude of their respective contributions to the measured dispersion. Since increasing the injection results in a proportional increase in the total photocurrent, in order to directly compare the outputs of these tests, it becomes necessary to normalize the testing so that the outputs are on the same scale. This has the added benefit of making the measured dispersion values into directly usable numerical factors as they represent multiple values of the unmodified transit times.

To standardize this work, time, photocurrent, and electric field are all normalized against an idealized TOF test that simulates the current across a trap free environment with photogeneration characteristics of infinitesimal time and absorption depth. These are given as follows by equations 3-2, 3-3, and 3-4:

$$t_T = \frac{L^2}{\mu_e \cdot V} \tag{3-2}$$

$$I_N = \frac{N \cdot scale \cdot q_e \cdot \mu_e \cdot V}{L^2} \tag{3-3}$$

$$E_0 = \frac{V}{L} \tag{3-4}$$

In this way, we encapsulate a square pulse with duration t_T and magnitude I_N drifting through an electric field of strength E/E_0. By normalizing against these characteristics, time t becomes a multiple factor of the transit time, current I; a fractional factor of the full current, and electric field E a percentage of the applied field E_0. Measured dispersion results will be provided as both multiples of the time normalization standard and as multiples of the low injection case dispersion value to measure the effect of the injection ratio change. Note that some tests are not expected to produce results with a discernable flight time, and as such, no dispersion value will be calculable for these tests.

For this first testing phase, the testing progression will perform time of flight simulations in the following generic semiconductor environments with charge injection being the variable factor in each:

- An ideal trap free environment with infinitesimal absorption depth δ and illumination time.
- A trap free environment with Gaussian illumination pulse time of variance σ = 0.01 t_T, 0.05 t_T, 0.1 t_T, 0.15t_T, and 0.2 t_T, and $\delta \approx 0$
- A trap free environment with delta absorption depth δ = 0.2L and absorption time of 0. Both species of carriers are used here with mobility drift ratio $b = \mu_e / \mu_h$ = 1.0, 0.1 and 10.0.

The electron drift mobility μ_e is constantly set at 0.01L. , and the applied field at 10V/μm The controlling factor here is *r*, which is the ratio of total injected charge to the charge of the applied field. Prior work by Blakney et al. asserts that the photoinjected discharge current waveform follows the same general shape so long as *r* remains below 10%[17] of the applied field; from which we accept that an injection ratio of 0.01% will produce no measurable alteration in the dispersion, providing a baseline value to evaluate the impacts of the increased injection ratios of 10%, 50%, 90% and 99%.

3.2.1.1 No generation variation

The expectations for the first tests are as follows. By simulating an infinitesimal absorption depth and illumination time, we are assuming that the photogeneration process creates a likewise infinitesimally thick plane of carriers drifting in the test medium as propelled by the applied voltage. In a trap free environment with an assumed constant value for microscopic mobility, there is no impediment to carrier flow to individual test packages, and thus no cause for spread in the test package collection time. This should be true regardless of the injection ratio applied.

This is a case where injection ratio variation highlights the fundamental effect of high electric field perturbation on the TOF waveform, being the sole contributing effect. Effectively, a plane of carriers creates a moving step function in the electric field with magnitude equal to the total injected charge. Since the applied biasing voltage is unaffected, the total field across the whole sample must also be so. As such, the field strength, as computed by tabulating drifting charges, is both position and time dependent, and subject to a time dependent integrating constant C_E. Thus, we get the following:

$$\frac{1}{N_{bins}} \cdot \sum_{X=1}^{N_{bins}} E(X,t) + C_E(t) = E_0$$

Where:

$$E(X,t) = E_0 + \frac{1}{2\varepsilon_0 \varepsilon_R} \cdot (Q_{x<X} - Q_{x>X})$$

$$Q_{x<X} = q_e \cdot \sum_{i=1}^{X-1} N_h(i,t) - N_e(i,t)$$

And:

$$Q_{x>X} = q_e \cdot \sum_{i=X+1}^{N_{bins}} N_h(i,t) - N_e(i,t)$$

Where N_{bins} is the number of quantized electric field bins, E_0 is the applied field, q_e is the charge of each scaled carrier package, and $N_h(i,t)$ and $N_e(i,t)$ are the number of each species of carrier positionally quantized into field bin i. Note that, in electric field calculations, carriers inside bin X are not tabulated, as doing so produced distorted results. It is assumed that any case where there are a substantial number of carriers in the bin, that they will be distributed roughly evenly, thus negating each other for the package counting process.

The integration value, C_E, manifests as a shifting change in the flow rate of the carriers. As the packet moves from $x = 0$ toward $x = L$, C_E starts low and rises according to the position and spread of the packet. As a uniformly distributed component of the electric field driving this movement, this represents an acceleration of all carriers in the bulk, as predicted by Papadakis[18].

The flow diagrams in Figure 3-4 illustrate the operational behaviour of the test platform for this phase. Starting with initialization of the parameters and carrier packages, the core of the test is performed through two nested loops; the outer of which encapsulates the behaviour of the whole system for each time interval *dt*, while the inner loop models the activities of each individual scaled test package from 1 to *N* for that time step. At each step, the electric field is calculated first based on the positions of all the carriers. The field is divided into *X* bins and both species of test packages are tabulated on each side of each bin to generate a total charge on each side of the bin, which is used to calculate the portion of the field injected by the test packages. The mean of the injected field is computed to produce the *field balancing* C_E, since the injected field must integrate to zero. Thus, we get equation 3-5:

$$E(x) = E_0 + E_{inj}(x) + C_E \qquad (3\text{-}5)$$

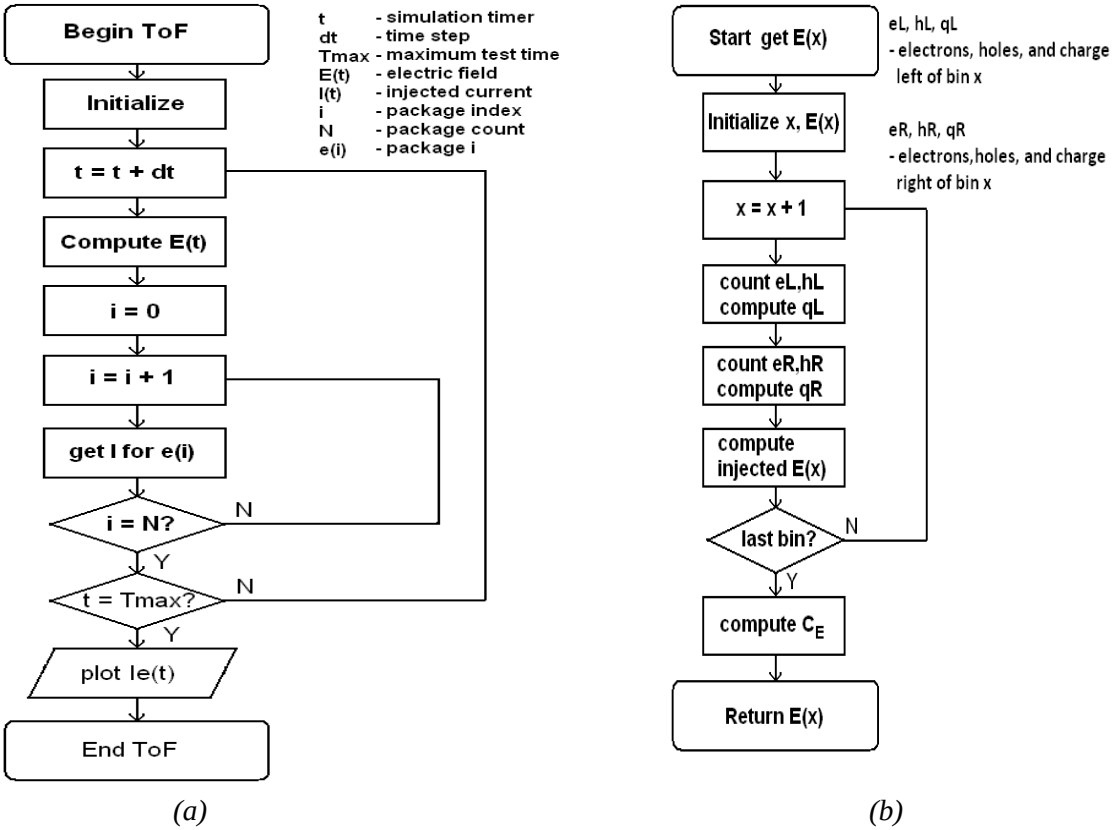

Figure 3-4: Flow diagrams for (a)main simulation and (b) electric field computation

After the time step's electric field is established, the inner loop computes a drift velocity for each package based on the microscopic mobility μ_e and the value of the electric field bin corresponding to the package's position in the bulk. This is tallied to a total photocurrent as per Ramo's theorem modified as shown in equation 3-6, with thickness L being normalized to 1:

$$I(t) = \frac{1}{I_{norm}} \cdot \sum_{i=1}^{N} \frac{scale \cdot Q_{e^-} \cdot Ve_i(t)}{L} \qquad (3\text{-}6)$$

Having determined the current for time step *dt*, the outer loop iterates from there until either all carriers are collected or the maximum testing time elapses. Results are saved and the test is repeated with a higher injection ratio.

3.2.1.2 Gaussian distributed generation time

The second set of testing simulates the variability of the excitation time during which EHP carrier packages are generated over a Gaussian distributed time frame with standard deviation of σ = 0.01, 0.05, 0.10, 0.15 and 0.2 of the normalized time scale t_T. By introducing time variance in the carrier generation, we introduce a source of carrier spread and thus dispersion. Given the non-uniformity of the perturbed electric field, carrier packages move at different rates depending on their position in the sample. Carrier packages generated first drift ahead initially and are propelled forward by the additional repulsive charge of later packages, thus starting at the unperturbed speed and accelerating thereafter. Carrier packages generated later are slowed by the repulsive effects of the prior packages but accelerate as the prior packages begin to undergo collection. At an injection ratio nearing unity, the final packages generated should experience a repulsive force from the preceding packages nearly on par with the applied field, and should thus

experience minimal drift until collection begins. The variable drift rates resulting from the perturbed field are reflected in the increase in dispersion as the injection ratio increases.

3.2.1.3 Delta absorption depth

Set three sets the excitation time back to zero, but introduces variation by simulating photoabsorption depth, which manifests as an exponentially distributed initial generation position for the carrier packages. This necessitates the TOF simulation for both species of carrier packages, since the holes had previously been assumed to have been immediately collected, negating any potential contribution to the photocurrent. It must also be noted that both species do not necessarily share the same microscopic mobility, and thus we must evaluate the effect of modulating the ratio of their mobilities. Also note that the absorption profile ensures that hole packages are collected much earlier than electron packages, due to their proximity to their collection electrode. The presence of the positive charge carriers serve to counterbalance the effect of the field perturbation by the negative charge carriers, with the effect being more pronounced where the mobility ratio $b = \mu_e/\mu_h$ is higher than 1.

Expectations for this set of tests are that the positive field influences of the hole carriers will increase the sum of the field, likewise reducing the balancing factor C_E, damping the acceleration experienced in their absence. Furthermore, the mixing of the carrier species will serve to reduce the net coulombic repulsion experienced by each carrier. This should lead to a lower rise in dispersion as the injection ratio increases, so long as the carrier species' are intermingling. In the instance of higher hole mobility μ_h (b = 0.1), the dispersive effects of mutual repulsion should recommence as the holes undergo quick collection, though the initial influence of the holes should still serve to reduce the injection ratio related net dispersion. In the instance of lowered

hole mobility (b = 10.0), the electrons should undergo complete collection prior to the holes, which linger to reduce the field acceleration and repulsion effects. Due to the generation profile, the magnitude of the effect of the holes on the dispersion should not be symmetrical around that of the case for b=1.0, since the hole collection profile mirrors that of electron collection.

3.2.2 Phase Two – Generic Amorphous Semiconductor

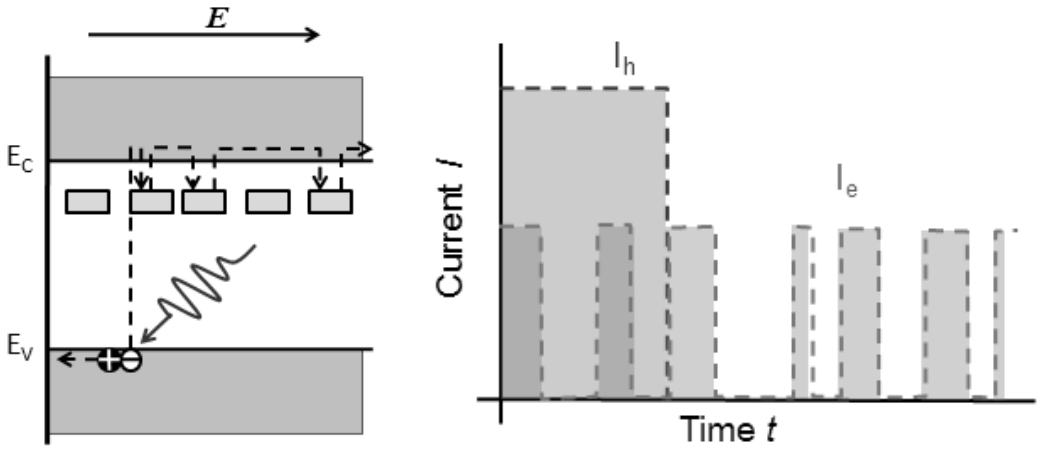

Figure 3-5: Energy band diagram and TOF waveform for an individual EHP drifting through an amorphous semiconductor showing the photocurrent staggering effects of trapping

Phase two revisits the infinitesimal generation profile of the first tests of phase one, but introduces localized trapping centres which impede charge carrier drift by serving as immobile positions for the carriers to thermalize into. Figure 3-5 shows the typical behaviour of an individual carrier package drifting in and out of these traps, and the subsequent effect on the photocurrent. Whereas previously, the TOF modelling approach was to run the simulation for each package until collection, this phase models the TOF against the times required for carriers to drift in and out of the local states. Trapping time is determined as a product of the carrier lifetime and an exponentially distributed random number. Generally, the average lifetime τ_C is determined by the concentration of localized traps: higher incidence of trap centres translates to

reduced time before a carrier thermalizes into one. For simplicity in testing, the average carrier lifetime will be specified in advance, leading to a corresponding - though irrelevant for this phase - trap concentration N_t. Likewise, as these traps are to be considered as shallow traps, localized traps of low relative depth so as to enable release, the average release time is also specified in advance; in this case by specifying a *mobility reduction factor* θ, which reflects the relationship between τ_C and τ_R, allowing us to derive an average release time τ_R and its corresponding trap depth. These computations are as follows below, where x is a uniformly distributed random number between 0 and 1:

$$t_{capture} = -\tau_C \cdot \log(x) \tag{3-7}$$

$$\theta = \frac{\tau_C}{\tau_C + \tau_R} \quad \rightarrow \quad \tau_R = \frac{\tau_C \cdot (1-\theta)}{\theta} \tag{3-8}$$

$$E_S = k \cdot T \cdot \log(f \cdot \tau_R \cdot t_T) \tag{3-9}$$

$$\begin{aligned} t_{release} &= -\log(x)/f \cdot e^{-\left(\frac{E_S}{k \cdot T}\right)} \cdot t_T \\ &= -\tau_R \cdot \log(x) \end{aligned} \tag{3-10}$$

Where $t_{capture}$ is the predicted carrier capture time given τ_C, k is the Boltzmann constant, E_S is the effective trap depth for a material with phonon frequency of f (in this work, f is given as 10^{11}Hz for the purposes of estimating trap depth), and $t_{release}$ is the predicted release time given τ_R.

To manage the eventualities of multiple traps and releases for each carrier package over the course of the test, we assign each package an event timer, which changes the state of the package from mobile to trapped and back when triggered. Upon expiration, the timer is reset with a new value based on the randomly computed time for the next event. To simulate the effect of trapping, drift for trapped packages is set to zero, which automatically computes to zero current

for the carrier in that time step. Time steps are scaled so as to be comparable to the lower of the event times; generally that of capture, since the mobility reduction factor θ is often below 10^{-2}. In doing so, we minimize the occurrence of multiple event changes in a single time step. Single event time steps allow for calculation of partial drift based on the portion of each time step during which the carrier is not moving.

Phase two uses the same testing platform described in Figure 3-4, but with an additional series of logical tests performed for each package at each time step to determine the drift state for each and its respective movement and generated photocurrent. The trap and release modelling section is shown in Figure 3-6, which also lists the parameters assigned to each carrier package for this phase. Carrier packages are individually polled for generation status, position, time until next state change event, and next event type. Carrier drift is induced only from carrier packages for which:

- Simulation runtime exceeds package generation time
- Package position is less than sample thickness
- State change event timer has not elapsed
- Package is either free or has an event timer at less than *dt*, resulting in partial drift

To improve the precision of these simulations, partial drift computations are made possible by determining the amount of each time step which corresponds to the portion where drift occurs. A free package nearing expiration of the event timer will drift only for the value of the timer instead of *dt*, whereas a trapped package will have *dt* minus the event timer. Partial drift is the velocity multiplied by the drifting time, while partial current is the charge multiplied by the fraction of the time step that the package drifts.

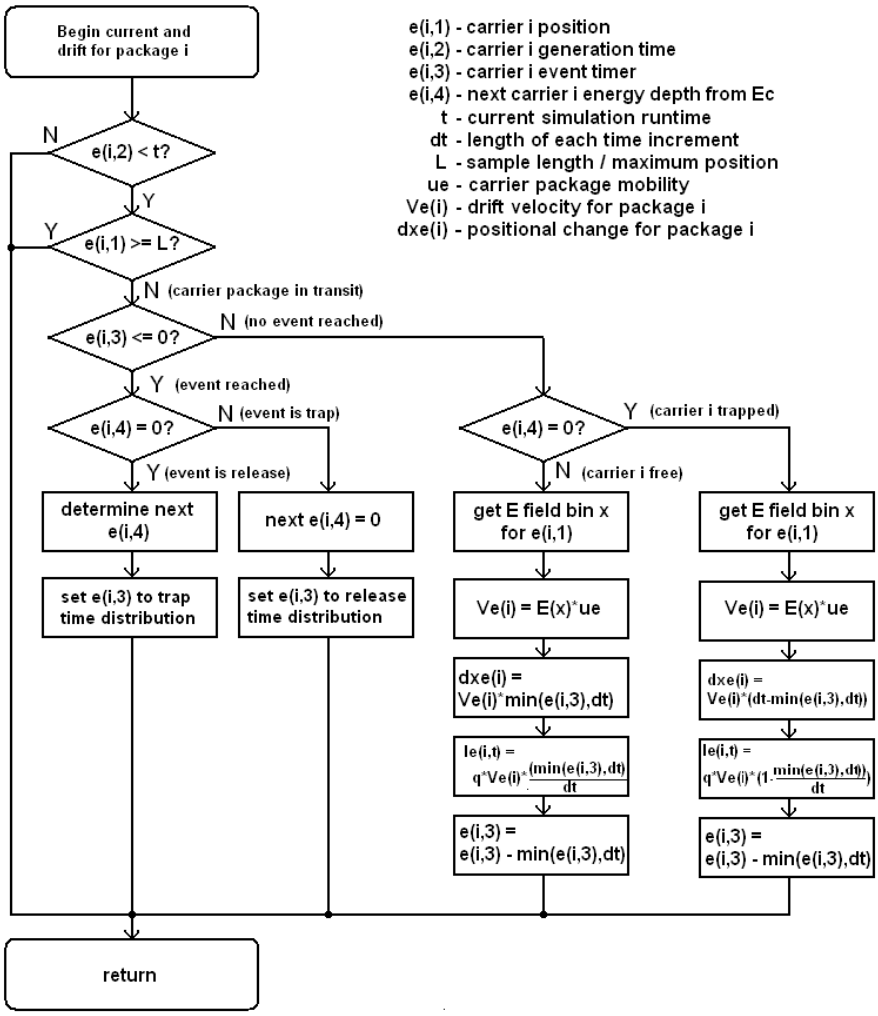

Figure 3-6: Flow chart for trap/release modelling and drift/current calculation for an individual electron carrier package.

Testing for this phase will consist of three different trapping arrangements comprising a total 240 simulation runs. All tests are performed for injection ratios of r = 0.01%, 10%, 50%, 90%, and 99%. These trapping schemes are listed as follows:

- A single discrete shallow trap only environment with capture time τ_C = $0.001t_T$, $0.01t_T$, and $0.1t_T$. Release is controlled by the mobility reduction factor θ = 0.001, 0.01, and 0.1
- A dual discrete level trap environment with τ_{CS} = $0.001t_T$, $0.01t_T$, and $0.1t_T$, τ_{CD} = $1/3t_T$, $1t_T$, and $3t_T$, θ_S = 0.001, 0.01, and 0.1, and θ_D = 0 ($\tau_{RD} = \infty$)
- A single ranged trap environment with τ_C = $0.01t_T$, θ = 0.001, 0.01, and 0.1, and a Gaussian distributed trapping depth of variance ΔE = $0.0001E_S$, $0.01E_S$, $0.1E_S$, $0.25E_S$

Each test output result in this phase will bear some resemblance to those of Figure 3-7, with a transient photocurrent waveform for the raw output, a waveform output smoothed using the algorithm described in section 3.1, and its corresponding time derivative function which makes dispersion calculation possible. Dispersion calculation is automated by specifying a search range of the derivative function from which the local minimum and its index are identified. For brevity, only the processed waveforms and their derivative functions will be examined.

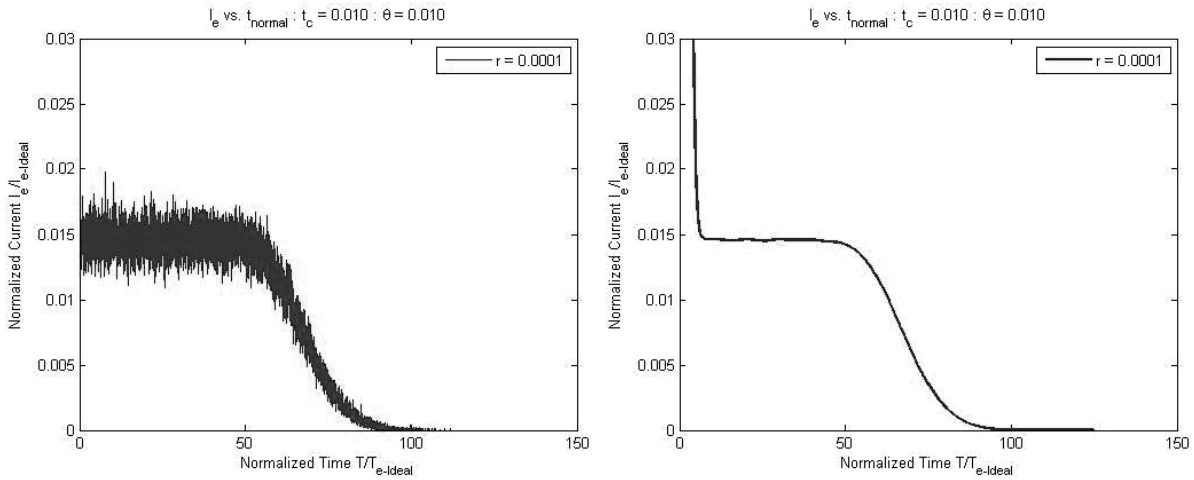

(a) *(b)*

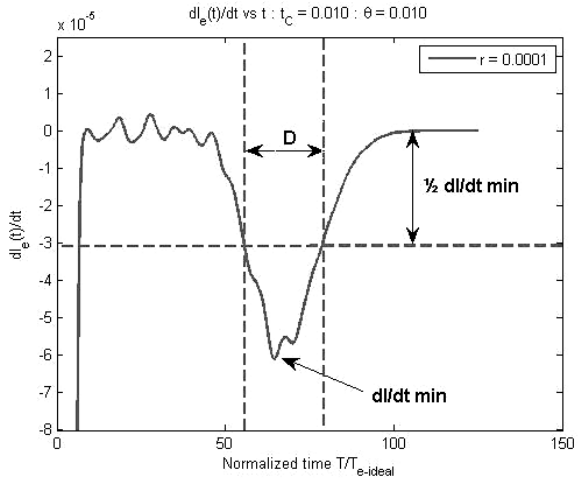

(c)

Figure 3-7: Time of Flight transient waveform for (a) raw output, (b) processed output, showing smoothing filter exaggerated thermalization and (c) derivative function of processed output and corresponding dispersion D, as measured in multiples of the transit time

The waveform of the processed test output reveals five key facets of TOF trap modelling. The first is in the beginning time steps, where drifting carriers undergo mass thermalization from the conduction band into the localized states. During this point, there is a sharp decrease in the number of free carriers drifting in the bulk. This is counterbalanced by a corresponding rise in the release of trapped carriers. Equation 3-11 shows how the rate of carrier change is governed by these two rates. The second TOF trap modelling facet is the point where this equation equals zero; a condition termed *detailed balance*, which signifies the equilibrium point between the capture and release rates, and manifests on the TOF waveform as a levelling off of the current. The third article of interest is the "knee" of the curve, which signifies the point of initial collection of drifting carrier packages. A sharp knee signifies low dispersion as it represents a cluster of carriers being collected in a short time span. Inversely, high prevalance of dispersion in the signal can obscure the knee entirely, making FWHM dispersion calculation all but impossible. The fourth item of note is visible in the differential function of the waveform $dI(t) \,/\, dt$. This is the local minima that corresponds to the point of highest carrier collection. It is at this minima from which dispersion is measured, by establishing the half-magnitude points on either side and measuring the time in between. The fifth facet of trap modelling is where the photocurrent falls to zero as all packags are either collected or trapped at depths that correspond to release times that exceed any practical measurement times.

$$\frac{dn_f}{dt} = \frac{n_t}{\tau_R} - \frac{n_f}{\tau_C} = 0 \qquad (3\text{-}11)$$

3.2.2.1 Discrete mono-level trapping

The first set in this phase simulates a single level of electron trapping at depth E_s as determined by the release time τ_R. By varying control factors τ_C, θ, and r, it is hoped that an

inference can be made as to the relationship of each factor to the output waveform and their corresponding dispersion values. The first such inferences can be made from modifying τ_C as compared to equation 3-11, which suggests that each tenfold increase in the capture time leads to a proportional, but not equal, increase in the number of free carriers at equilibrium. The inequality is due to the mutual dependence of n_t and n_f. The rise of free carrier counts corresponds to a proportional rise in current and proportional decrease in the average carrier transit time.

With the carrier capture time hard set, the only result from using θ as a control factor is the inverted response in the release time τ_R illustrated in Figure 3-8 as calculated from equation 3-8. This inversely proportional relationship between the release time and the control factor should translate directly into a magnitude of dispersive response for all injection ratios. Increasing release time by reducing θ translates into longer simulation runs; the case where θ = 0.001 corresponds to approximately a thousand-fold increase in the duration of the simulation time, while θ = 0.1 produces only a tenfold increase in test time. This factors into the selection of the maximum testing time for each simulation run; since the time step *dt* is scaled against the capture time, the average capture/release event pair time becomes approximately τ_C / θ. Working with $dt = \frac{1}{2}\tau_C$, this returns a typical trap/release time of $\approx 1 / (2\theta)$ time steps. Assuming that each carrier package is captured $1/\tau_C$ times during transit, this yields an expected average transit time of $1 / (2\theta\tau_C)$ time steps, which, in the case of τ_C = 0.001 and θ = 0.001, translates into 2,000,000 time steps to model! This assumes no other dispersive effects are prolonging the test; a case which is presumed false with expectations from injection ratio increases.

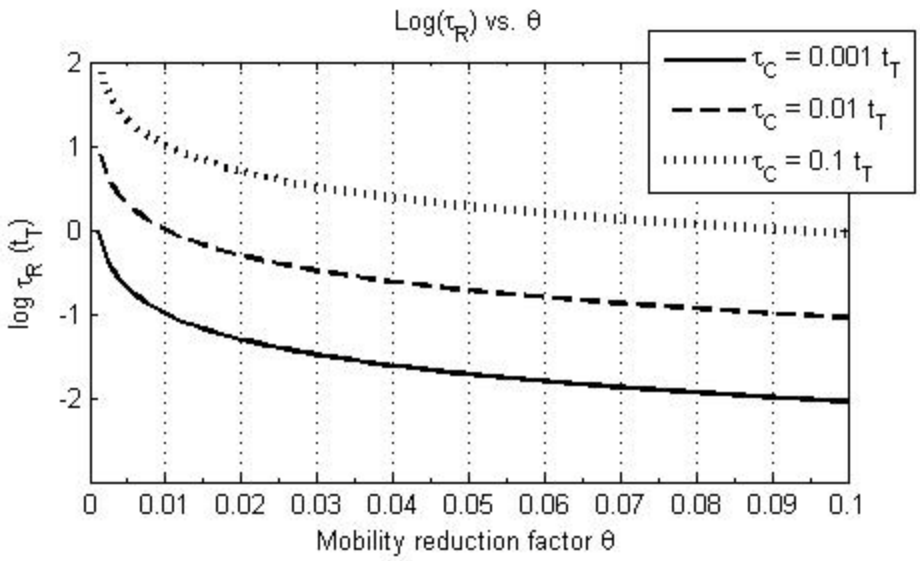

Figure 3-8: Response of release time τ_R to changes in θ for preset capture times of $\tau_C = 0.001t_T$, $0.01t_T$, and $0.1t_T$.

The third control factor *r* is expected to have the same effect as in phase one, but with the initial dispersion being caused by the uneven trapping of the carrier packages. Injection ratios of 0.01%, 10%, 50%, and 99% are examined for each combination of τ_C and θ to reveal what influences are present from the injection ratio testing.

3.2.2.2 Discrete bi-level trapping

In a multiple level trap system, the same basic testing principle applies as for a singular level. Multiple level simulations increase the complexity of the model by necessitating a selection routine that assigns a trap depth based on the concentrations corresponding to each trap level. This routine operates by randomly determining a carrier lifetime for all trap types upon expiration of the package event timer, and then setting the timer to that of the lowest lifetime. In this way, the testing model can easily incorporate any number of trap types, each with unique concentrations and energy distributions.

The energy levels of interest for this round are designated as either shallow or deep. Shallow traps, as mentioned previously, are low depth localized states that have a brief release time resultant of thermal excitation back into the conduction band. The other trap type of interest is the deep trap, which has a release time often far in excess of any practical testing time, and thus for all practical purposes is hard set to infinity. As such states have no functional release rate, this manifests as a time progressive attenuation in the number of drifting carriers and subsequently the photocurrent.

Simulations for this phase will be performed using all combinations of τ_C, θ, and r from the shallow state testing, but with deep trap carrier lifetimes of $\tau_{CD} = 1/3t_T$, $1t_T$, and $3t_T$. The deep trap release rate $1/\tau_{RD}$, while theoretically non-zero, is hard set to zero for simplicity. Expectation holds that the simulated TOF waveforms should experience net collection rates of≈ 5%, 37%, and 72% respectively for each deep trap lifetime. These collection rates correspond to the percentage of carriers with expected capture times higher than the transit time t_T, again assuming no disruption from additional dispersive effects. As higher electric field perturbation is known to extend transit time, we expect a lower collection rate as r increases.

3.2.2.3 Gaussian mono-level trapping

The final set of simulations replicates the circumstances of the mono-energetic trapping depth tests, but this time introduces a Gaussian spread in the carrier depths such as shown in Figure 3-9. Tests are performed based on the parameters of $\tau_C = 0.01t_T$, $\theta = 0.001$, 0.01, and 0.1, and injection ratios of $r = 0.0001$, 0.1, 0.5, 0.9, and 0.99. As θ represents the control factor for a discrete trapping model, its use here will be in identifying a specific mean depth of trap states at E_S as it corresponds to specific test parameters of lattice vibration frequency and sample temperature. This allows us to specify the standard deviation σ of the trapping state distribution

as a fraction of the trap depth. Simulations are performed for each of the above parameter combination for $\Delta E_1 = 0.0001E_S$, $\Delta E_2 = 0.01E_S$, and $\Delta E_3 = 0.1E_S$, where $\sigma = \frac{1}{2}\Delta E$.

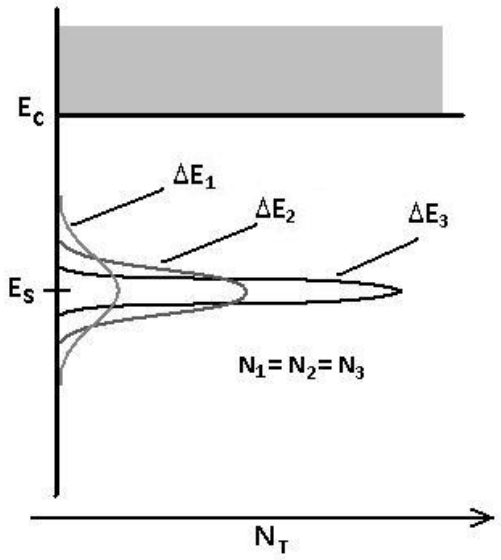

Figure 3-9: Energy band diagram for gaussian distributed mono-energetic trapping with constant state concentration N, mean energy depth $\mu = E_S$, and energy depth standard deviation $\sigma = \Delta E/2$

The purpose of this round of testing is to clarify how the dispersion due to a discerete level compares with that due to a Gaussian distribution. The expectation is that higher spread correlates to higher dispersion times largely on account of the trap states located at the extremes of the distributions. We know that thermal carrier excitation is a random process based on the exponential distribution of the Boltzmann factor. Using the first standard deviation from the mean on each side, the release rates for trap depths E_S, $E_S + \Delta E/2$, and $E_S - \Delta E/2$ are given as:

$$\frac{1}{\tau_{R(0\sigma)}} = \upsilon e^{\frac{-(E_C - E_S)}{k \cdot T}} \qquad \frac{1}{\tau_{R(-1\sigma)}} = \upsilon e^{\frac{-(E_C - E_S + \Delta E/2)}{k \cdot T}} \qquad \frac{1}{\tau_{R(+1\sigma)}} = \upsilon e^{\frac{-(E_C - E_T - \Delta E/2)}{k \cdot T}}$$

This is used to establish the ratios of $1/\tau_{R(-1\sigma)}$ to $1/\tau_{R(0\sigma)}$ and $1/\tau_{R(0\sigma)}$ to $1/\tau_{R(+1\sigma)}$, which becomes:

$$\frac{\tau_{R(-1\sigma)}}{\tau_{R(0\sigma)}} = \frac{\tau_{R(0\sigma)}}{\tau_{R(+1\sigma)}} = e^{\frac{-\Delta E}{2k \cdot T}} \qquad (3\text{-}12)$$

So, at T = 298K, for ΔE = 0.1, the release ratio from that of E_S is 0.1427 for -1σ and 7.008 for +1σ. That is to say that the lower 15.8% of trapped carriers will remain trapped at least forty-nine times longer than the higher 15.8%. The potential dispersion that arises from this trap time disparity is considerable. This is, at core, a test of dispersion as a result of variation in release time. As this is independent of any interference from injection ratio testing, the expected dispersive contributions from this work's injection ratio testing should resemble that of the discrete level trapping tests' contributions.

3.2.3 Detailed Balance

The equilibrium point between capture and release rates is an important state because it leads directly into the derivation of our mobility reduction factor θ. Given that n_t represents the number of trapped carriers and n_f, the number of free carriers, we define these terms as described by the Boltzmann energy distribution. Inserting the capture and release rate formulae into equation 3-11, we get the steady state condition as equation 3-13:

$$n_f = N_c e^{\frac{(-E_C + E_F)}{k \cdot T}}$$

$$n_t = N_t e^{\frac{-(E_T - E_F)}{k \cdot T}}$$

$$\frac{1}{\tau_C} = \nu_{th} \sigma_C (N_t - n_t)$$

$$\frac{1}{\tau_R} = \upsilon e^{\frac{-(E_C - E_T)}{k \cdot T}}$$

$$\frac{dn_f}{dt} = n_f \nu_{th} \sigma_C (N_t - n_t) + n_t \upsilon e^{\frac{-(E_C - E_T)}{k \cdot T}} = 0 \qquad (3\text{-}13)$$

Assuming N_t (the number of trapping states) >> n_t (the number of trapped carriers) to neglect trap filling effects, we can redefine the capture rate as:

$$\frac{1}{\tau_C} = \nu_{th} \sigma_C N_t$$

Which turns equation 3-13 into:

$$\frac{dn}{dt} = -\frac{n_f}{\tau_C}\left(1 - \frac{n_t}{N_t}\right) + \frac{n_t}{\tau_R} = 0 \qquad (3\text{-}14)$$

Which, when rearranged to isolate the ratio of free-to-trapped carriers, n_f and n_t, yields:

$$\frac{n_f}{n_t} = \frac{\tau_C}{\tau_R}\left(1 + \frac{n_f}{N_t}\right) \qquad (3\text{-}15)$$

Up to this point, the carrier concentrations are predicated on an arbitrary amount n_f which is in balance with n_t. Specifying a total carrier injection count of $n_0 = n_f + n_t$, the ratio of free-to-total carriers becomes n_f/n_0, which appears as:

$$\frac{n_f}{n_0} = \frac{n_f}{n_f + n_t} = \left[1 + \frac{n_t}{n_f}\right]^{-1} = \left[1 + \frac{\tau_R}{\tau_C}\left(\frac{N_t}{n_f + N_t}\right)\right]^{-1}$$

Assuming, as with n_t, that N_t is likewise much greater than n_f, this returns us to equation 3-8 and our mobility reduction factor θ.

$$\frac{n_f}{n_0} = \left[1 + \frac{\tau_R}{\tau_C}\right]^{-1} = \frac{\tau_C}{\tau_C + \tau_R} = \theta \qquad (3\text{-}16)$$

The alternate case where N_t is comparable or less than n_f describes the state where the traps are saturated with carriers, representing the absolute limit of the amorphous semiconductor's capacity to restrict free carrier drift. Intuitively speaking, trap filling becomes more relevant as the injection ratio *r* increases, but as trap filling is outside the scope of this work, with capture lifetimes specified a priori, the presumption that $N_t >> n_f$ will serve as the operational case for all simulations. This case is, however illustrative of the effects of θ in that, absent trap related restrictions on the current due to filling of the traps, the conductivity σ_0 becomes:

$$\sigma_0 = q_{e^-} \cdot n_0 \cdot \mu_0 \tag{3-17}$$

While the trap reduced conductivity is:

$$\begin{aligned} \sigma_{eff} &= q_{e^-} \cdot n_f \cdot \mu_0 \\ &= q_{e^-} \cdot \theta \cdot n_0 \cdot \mu_0 \\ &= \theta \cdot \sigma_0 \end{aligned} \tag{3-18}$$

This leads to the corresponding modulations of drift mobility μ_{eff}, effective photocurrent I_{eff}, and transit time t_{eff} as listed below:

$$\mu_{eff} = \theta \cdot \mu_0 \tag{3-19}$$

$$I_{eff} = \frac{n_f \cdot scale \cdot v}{L} = \frac{\theta \cdot n_0 \cdot scale \cdot v}{L} = \theta \cdot I_{norm} \tag{3-20}$$

$$t_{eff} = \frac{L^2}{\theta \cdot \mu_0 \cdot V} = \frac{t_T}{\theta} \tag{3-21}$$

3.3 Summary

In this chapter, we outlined the procedure for this work and laid the foundations for the expectations for the following chapter. We identified the strengths and limitations of MATLab as the simulation platform. It was established that MATLab functions adequately to the specified needs of the testing procedure, and that the data processing routines used in removing noise from the TOF waveforms are only nominally disruptive to the general trend of the original waveform. Additionally, we outlined the operational flow of the simulation program as it applies to each segment of testing.

The testing plan was detailed as parsed into two main phases each consisting of three testing schemes. The first phase simulated a crystalline semiconductor with systemic variance being introduced as a product of the photogeneration profile of each test. The expected effects of field perturbation were explained and their relationship to the photogeneration profiles identified. The first scheme identified the direct effect of perturbing the applied electric field through high carrier injection. The second scheme illustrated the dispersive effects of coulombic repulsion between single species carrier packages as the injection ratio increased. The third scheme explained how the presence of both carrier species served to counterbalance the perturbing effect of scheme one and the dispersive effect of scheme two.

Phase two replicated carrier transit though a generic amorphous semiconducting solid by modelling of the trap/release behaviour that results from the abundance of localized states below the conduction energy level E_C. The fourth scheme is used to illustrate how the control factors of capture time τ_C, mobility reduction factor θ, and injection ratio r are used to create different impacts on the measured dispersion of the TOF waveform. The fifth scheme detailed how the model handles multiple trap types, and how deep traps cause reduction of the current and total

charge collection. The sixth testing scheme highlights how dispersion is reduced by the artificiality of modelling with discretely distributed trap depths as opposed to using a continuous distribution of energy depths.

Finally, an explanation of the detailed balance state was used in the derivation of the mobility reduction factor θ, as well as its corresponding importance in predicting the reduction in drift mobility, the reduction in current at detailed balance given a known carrier injection quantity, and the rise of the average carrier transit time.

Chapter 4 Results and Discussion

This chapter is dedicated to the output results of the testing outlined in chapter 3. As laid out in Chapter 3, the work is broken down into two primary phases to simulate both primary classifications of semiconductor. In doing so, phase one simulates crystalline semiconductors and is used to evaluate dispersive effects as caused by the initialized state of the sample. Phase two, which simulates amorphous semiconductors is used to evaluate the intermediary effects related to carrier trapping.

4.1 Phase One

This section contains the results from the generic crystalline semiconductor simulations. It contains the output photocurrent waveform results from each phase of the test, as well as recordings of the carrier positions and the corresponding electric field at times $t = 0.1t_T$, $0.5t_T$, $1.0t_T$, and $1.5t_T$ if applicable. By comparing these recordings side-by-side, we can see the unevenness in the carrier drift as r increases. Additionally, we'll evaluate the effects of the charge carrier distribution on the electric field as a product of its two main effects; field disruption and mutual repulsion between carriers. The simulations are performed using the parameters delineated in Section 3.2.1.

4.1.1 No variation in carrier package generation

The first set to evaluate is the case where the illumination time and absorption depth are infinitesimal, resulting in a hypothetically perfect plane of carriers drifting through the bulk sample as propelled by the electric field. This is achieved by setting the generation time to a fixed value and the absorption depth to slightly above zero, since carriers are deemed collected at exactly zero. Figure 4-1 shows the results of the first set of tests corresponding to their respective entries in Table 4-1. The first items of note are:

- Time of flight current waveform is mostly unchanged between $r = 0.01\%$ and $r = 1\%$.

- At r = 10%, distortion of the electric field begins producing a more pronounced effect on the TOF waveform.
- As injection ratio increases above 10%, current reduced due to reduced drift caused by field perturbation.
- As field balancing constant $C_E(t)$ rises, carrier packages accelerate, producing an corresponding rise in the photocurrent which mimics that of C_E
- Total collected charge is unchanged between tests
- Regardless of injection ratio, dispersion is always zero because there is no lateral spread between carrier packages to be expanded by carrier charge repulsion. This is an artefact of the simulation parameters

Table 4-1: Scaling results for infinitesimal carrier package plane

No trapping : Absorption depth Δ = 0 : Uniform excitation time = 0 : N = 10,000						
Plot	Dk Blue	Red	Green	Black	Lt Blue	Magenta
Injection ratio r	0.0001	0.01	0.10	0.50	0.90	0.99
Scale	3.537×10^{7}	3.536×10^{9}	3.537×10^{10}	1.768×10^{11}	3.183×10^{11}	3.501×10^{11}
Transit Time (t_T)	1	1	1.005	1.025	1.080	1.095

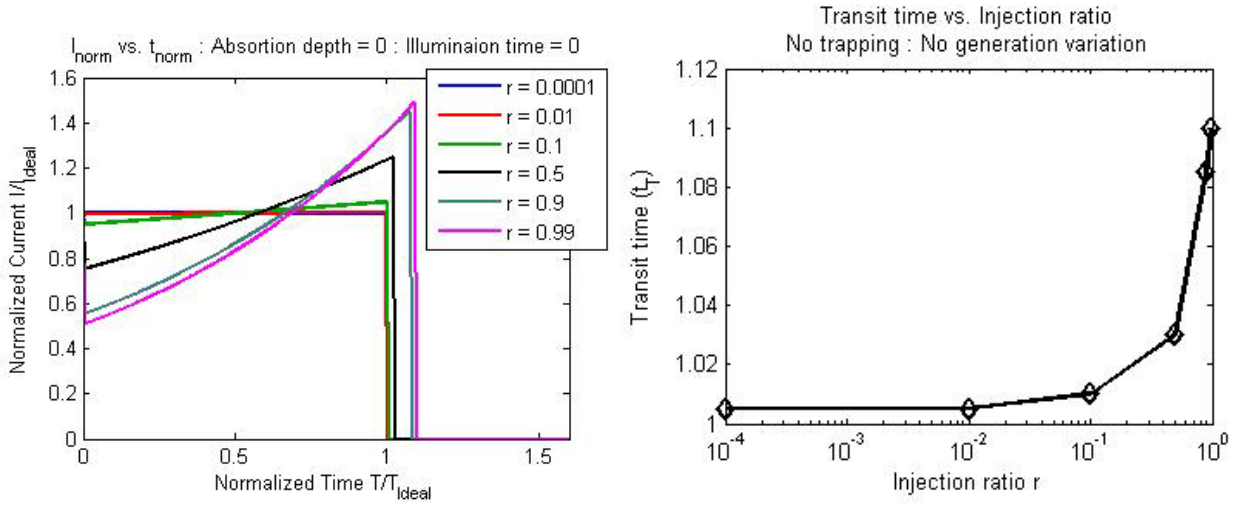

(a) *(b)*

Figure 4-1: TOF results for infinitesimally thick carrier plane including (a)induced transient photocurrent and (b) transit time as a function of injection ratio

The significance of Table 4-1 is to illustrate that the only difference in testing parameters between tests is in the scaling factor computed for ratio *r* which is used for each test. These are the values by which the charge tabulations and current computations are multiplied.

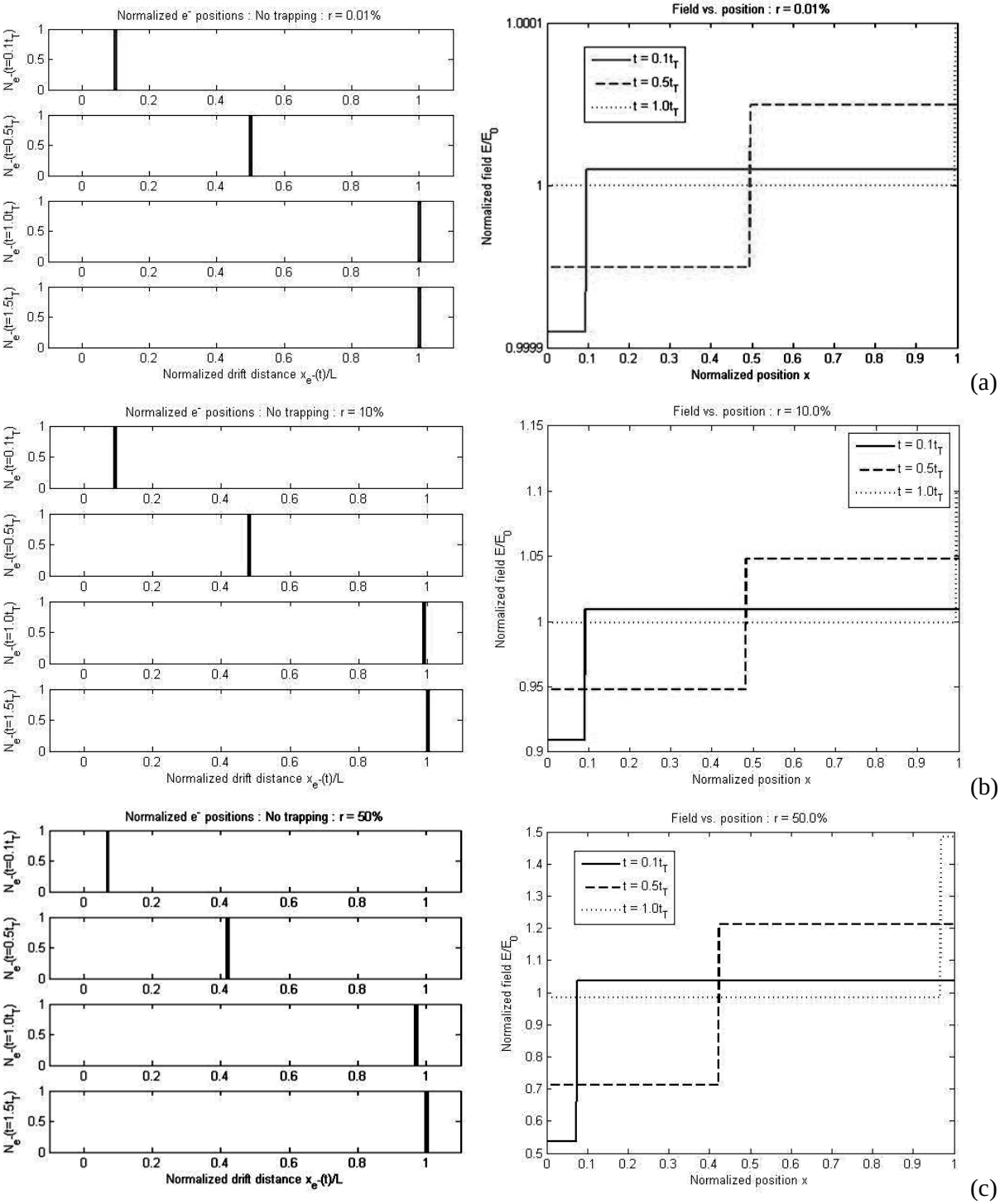

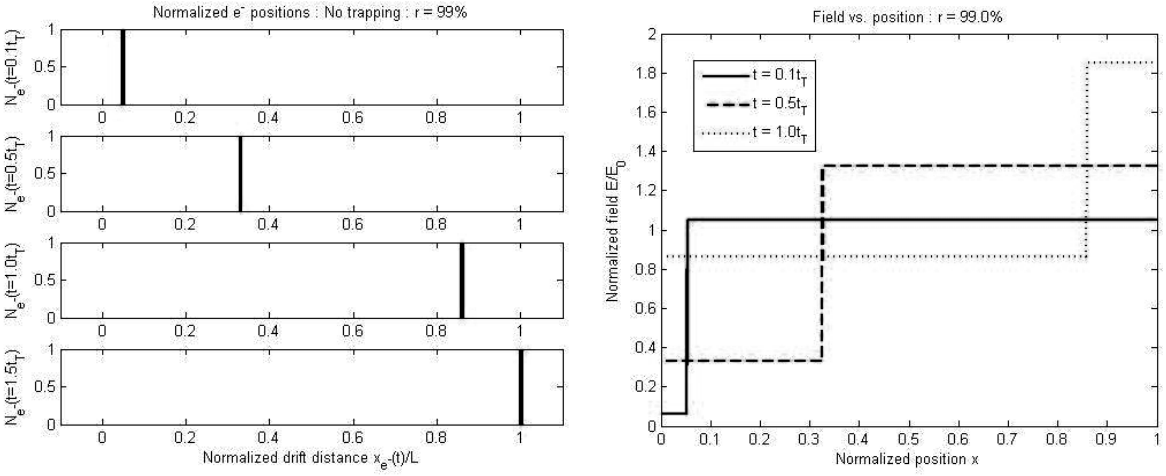

(d)

Figure 4-2: Package distributions and electric fields for infinitesimal carrier package plane at times t = 0.1t_T, 0.5t_T, 1.0t_T, and 1.5t_T for injection ratios of (a) r = 0.01% (b) r = 10% (c) r = 50% (d) r = 99%

Figures 4-2(a) to (d) show how the carrier packages drift less as the field is disturbed more. At the same times in each test, the higher injection cases have progressed a shorter distance into the bulk of the sample, as evidenced by the position histograms for each. The field balancing C_E is shown below in Figure 4-3 as a function of time for each injection ratio. In these tests, since the packages move as a sheet occupying a single bin of the electric field, the algorithm counts no carriers on each side, thus, modified from equation 3-5, the field driving the carriers is given as:

$$E_{norm}(x,t) = 1 + \frac{C_E(t)}{E_0} \qquad (4\text{-}1)$$

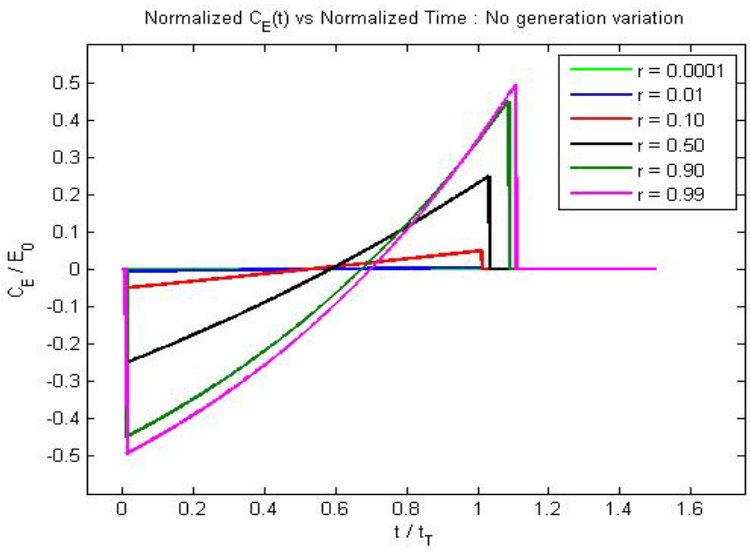

Figure 4-3: Time dependence of field balancing constant C_E for infinitesimal carrier package plane

4.1.2 Gaussian distribution of generation time

To simulate the natural spread of the laser illumination time, we adjust the generation time parameter for each carrier package from a fixed value to a Gaussian distributed random variable of mean `xbar` ($\bar{x}$) and standard deviation `dev` (σ). The statement used for this is:

```
eSt(i,2) = max(xbar + randn(1)*dev,0);
```

where `eSt(i,2)` is the generation time for carrier package `i`. As previously discussed, the `randn(M)` function creates an $M \times M$ array of Gaussian distributed numbers of variance $\sigma^2 = 1$. Each simulated carrier package is assigned a unique generation time based on the above; corrected to zero for instances where the random time generated falls below zero. For this reason, `xbar` is typically chosen as approximately three times `dev`, so as to minimize artificial clustering of packages at $t = 0$.

Unlike as with the results from Section 4.1.1, where no initial spread existed to expand upon, by varying the generation time, we introduce a real world analogue for carrier spread. At low injection, with no other effects increasing spread, we see that the TOF curve at collection mirrors

the curve at generation. Most simply put, dispersion in equals dispersion out. As such, these cases makes for good baselines to evaluate how much spread is introduced by the higher injection ratio experiments. At high injection, the mutual coulombic repulsion between larger charge packages propels the initial carrier packages forward while inhibiting the movement of the packages generated afterward resulting in added dispersion. Figure 4-4 shows how the dispersion changes for each excitation time first as a time normalized measurement, and then as normalized against the low injection case. The results of this set of tests are detailed below in Table 4-2 and Figure 4-5.

Table 4-2: Dispersion results for Gaussian excitation time

No carrier trapping : Uniform absorption depth = 0 : Gaussian excitation time standard deviation σ : N = 10,000 packages					
Plot on figures		Green	Blue	Black	Magenta
Injection ratio r		0.0001	0.10	0.50	0.99
Scale(carriers/package)		3.537×10^{7}	3.537×10^{10}	1.768×10^{11}	3.501×10^{11}
Dispersion D (t_T)	σ = 0.01	0.0506	0.1229	0.4140	0.6615
	σ = 0.05	0.1246	0.2101	0.4979	0.8201
	σ = 0.10	0.2435	0.3092	0.5682	0.8777
	σ = 0.15	0.3371	0.4035	0.6227	0.8924
	σ = 0.20	0.4695	0.5394	0.6993	0.9126

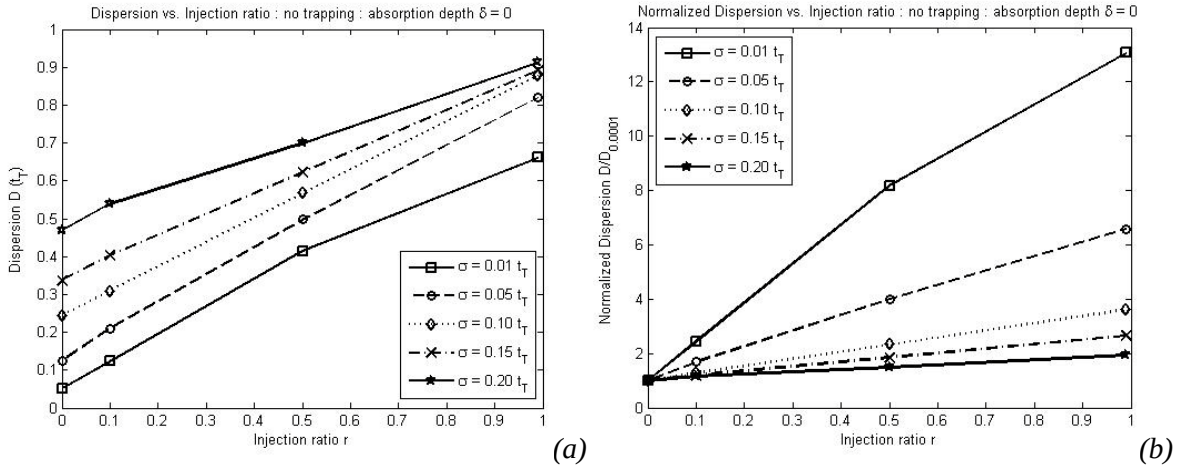

(a) *(b)*

Figure 4-4: Dispersion comparisons for Gaussian generation time (a)as measured and (b) as a multiple of the low injection case dispersion $D_{0.0001}$

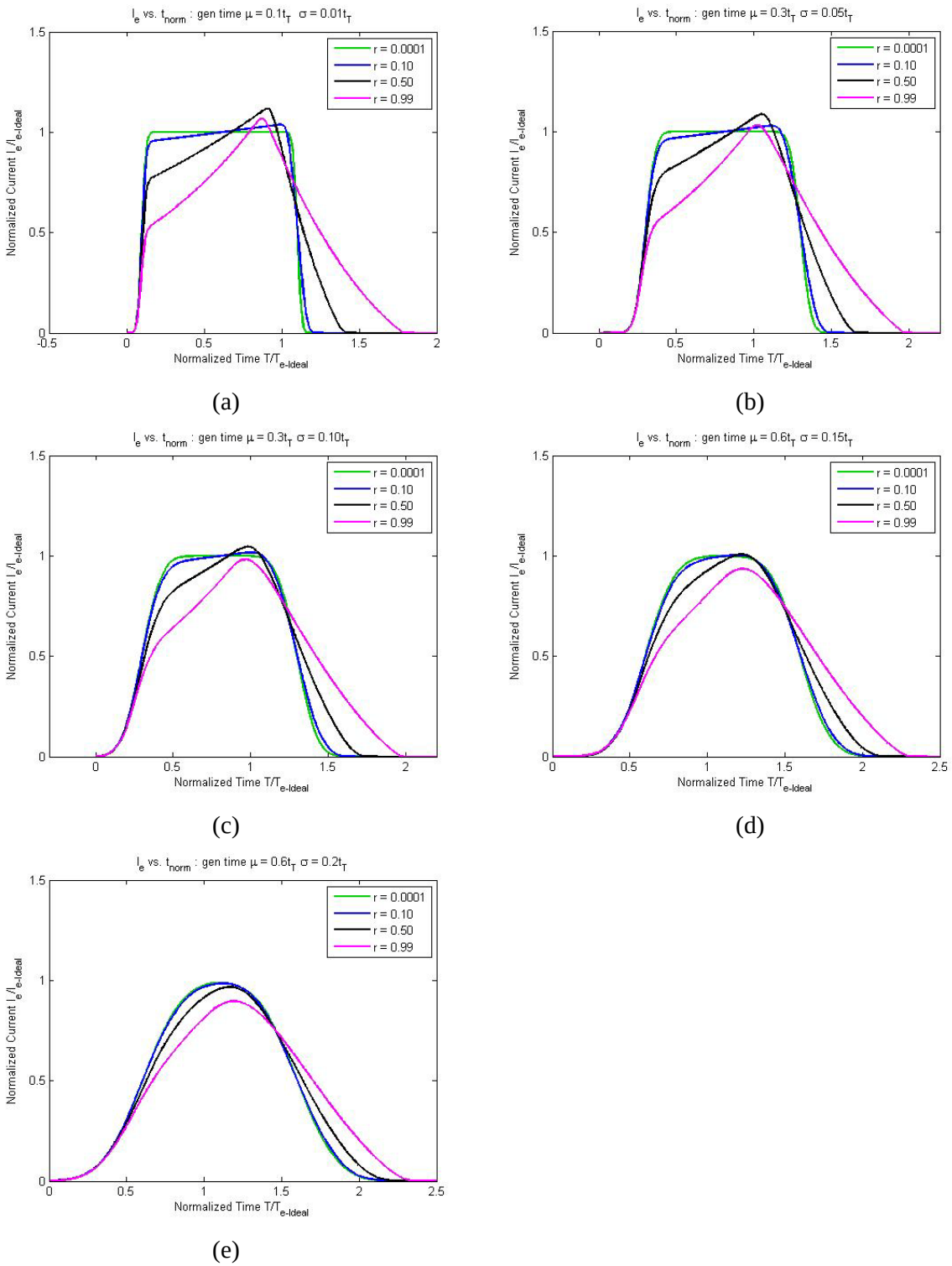

Figure 4-5: TOF waveform results for Gaussian generation time for (a)$\sigma = 0.01t_T$,(b) $\sigma = 0.05t_T$, (c) $\sigma = 0.10t_T$, (d) $\sigma = 0.15t_T$, and (e) $\sigma = 0.20t_T$

The very first thing we can infer from Figure 4-4 is that dispersion values from the TOF waveforms as injection ratios increase appear to be additive in magnitude, rather than

multiplicative. Generally, the dispersion increases from $D_{0.0001}$ at the low injection cases to $D_{0.0001}$ plus ~0.6 t_T (0.6L being roughly the distance spread at 1 t_T - see *Table 4-3*) for the highest injection cases. We know that the only factors contributing to carrier dispersion are the field balancing which distorts the average drift velocity of all carriers as a function of time and the mutual coulombic repulsion between same-charge carriers, which distorts the field and individual drift velocities as a function of relative carrier position. The field balancing factor is best simplified as:

$$C_E(t) = \frac{1}{L} \cdot \int_0^L E_{inj}(x,t)dx \qquad (4\text{-}2)$$

The injected field is generalized from modifying the Gaussian CDF of the carrier packages as:

$$E_{inj}(x,t) = \frac{E_0 \cdot r}{2} \cdot erf\left(\frac{x - \mu_x(t)}{\sqrt{2 \cdot \sigma_x(t)^2}}\right) \qquad (4\text{-}3)$$

where $\mu_x(t)$ and $\sigma_x(t)^2$ are the time-dependent mean position and positional variance of the carrier package pulse. Because the earliest generated packages experience dispersive effects before the later packages, this distribution is inherently inaccurate. Neglecting this initial dispersion, we assume the mean position to be the bin where the carrier count on each side is equal, which corresponds roughly to the current position of the middle packages generated at time $t = \bar{x}$, and which is least influenced by the coulombic spreading that characterizes the high injection testing. Effectively, $E_{inj}(\mu_x(t),t) = 0$, thus:

$$\mu_x(t) = \left(E_0 - C_E(t)\right) \cdot \mu_e \cdot t + \bar{x} \qquad (4\text{-}4)$$

The time variance of the pulse is best given as a time/ratio dependent variant of the initial pre-specified variance σ_{x0}. At +1σ, ~15.8% of the injected charge is impeding carrier drift while ~84.2% is propelling it. This leaves a net percentage of ~68.4% of the injected charge propelling drift at +1σ and impeding drift at -1σ. Thus, the injected field strengths at these locations are $\pm 0.684 \times E_0 \times r$. This gives a relative drift velocity of:

$$V_{rel(\pm\sigma)} = (\pm 0.684 \cdot E_0 \cdot r) \cdot \mu_e$$

and:

$$dx_{rel(\pm\sigma)}(t) = \begin{cases} 0 & : \ t < 0 \\ V_{rel(\pm\sigma)} \cdot t & : \ t \geq 0 \end{cases}$$

Since this is the relative drift of the variance of the carriers pulse from its original value σ_{x0}:

$$\sigma_x(t) = \sigma_{x0} + (0.684 \cdot E_0 \cdot r \cdot \mu_e \cdot t) \qquad (4\text{-}5)$$

Noting that the time dependence of the variance shifting is independent of the original variance, the additive nature of coulombic repulsion dispersion should come as no surprise. Using the test parameters given in section 3.2.1.2, for r = 0.0001, 0.10, 0.50, and 0.99, we should expect variance changes as listed in Table 4-3. Considering the dispersion results from Table 4-2, estimating the dispersion from the Gaussian spread and the injection ratio shows loosely proportional agreement with the simulated results.

Table 4-3: Expected test package variance spreads for injection ratio r and simulation time t

Ratio / Time	r = 0.0001	r = 0.10	r = 0.50	r = 0.99
$t = 0.1t_T$	6.84e-6	0.00684	0.0342	0.0677
$t = 0.5t_T$	3.42e-5	0.0342	0.171	0.3386
$t = 1.0t_T$	6.84e-5	0.0684	0.342	0.6773
$t = 1.5t_T$	1.026e-4	0.1026	0.513	1.0157

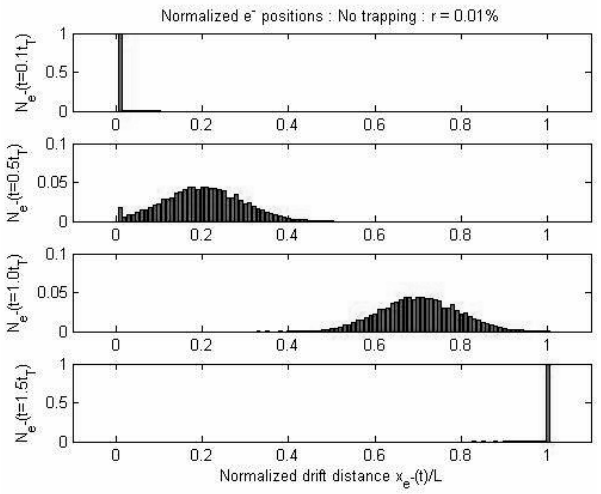
Normalized e⁻ positions : No trapping : r = 0.01%
N_e⁻(t=0.1t_T)
N_e⁻(t=0.5t_T)
N_e⁻(t=1.0t_T)
N_e⁻(t=1.5t_T)
Normalized drift distance x_e⁻(t)/L

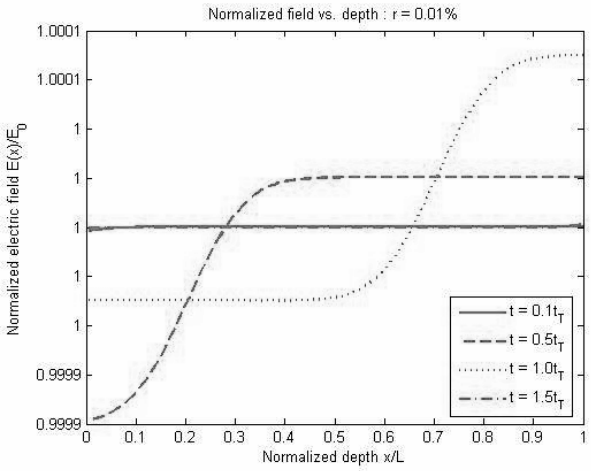
Normalized field vs. depth : r = 0.01%
Normalized electric field E(x)/E_0
Normalized depth x/L
t = 0.1t_T
t = 0.5t_T
t = 1.0t_T
t = 1.5t_T

(a)

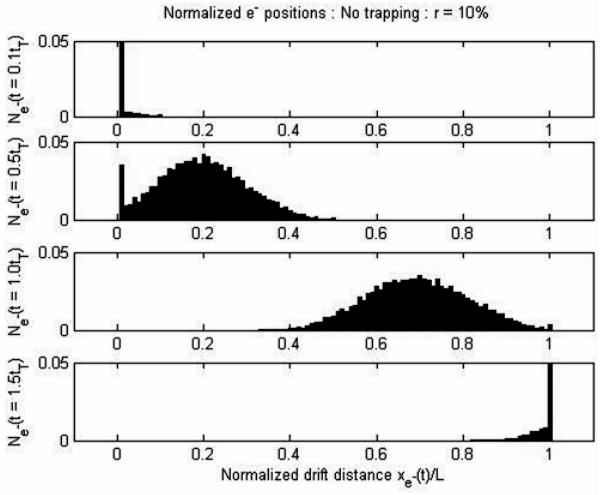
Normalized e⁻ positions : No trapping : r = 10%
N_e⁻(t = 0.1t_T)
N_e⁻(t = 0.5t_T)
N_e⁻(t = 1.0t_T)
N_e⁻(t = 1.5t_T)
Normalized drift distance x_e⁻(t)/L

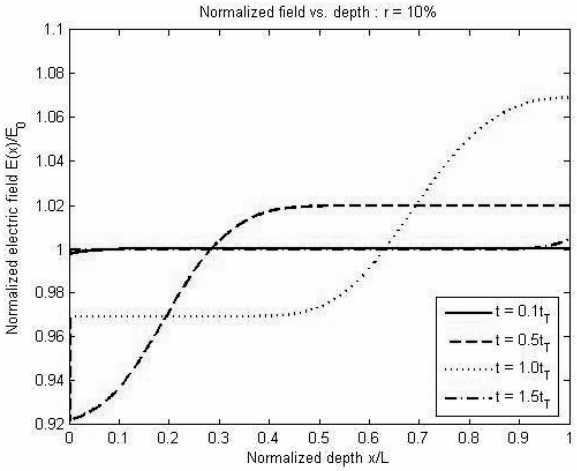
Normalized field vs. depth : r = 10%
Normalized electric field E(x)/E_0
Normalized depth x/L
t = 0.1t_T
t = 0.5t_T
t = 1.0t_T
t = 1.5t_T

(b)

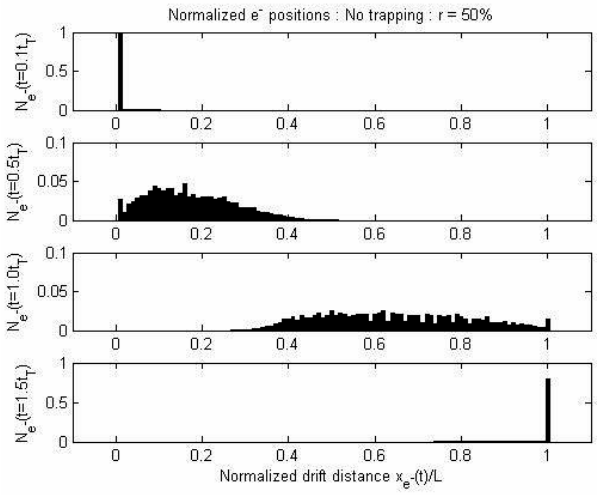
Normalized e⁻ positions : No trapping : r = 50%
N_e⁻(t=0.1t_T)
N_e⁻(t=0.5t_T)
N_e⁻(t=1.0t_T)
N_e⁻(t=1.5t_T)
Normalized drift distance x_e⁻(t)/L

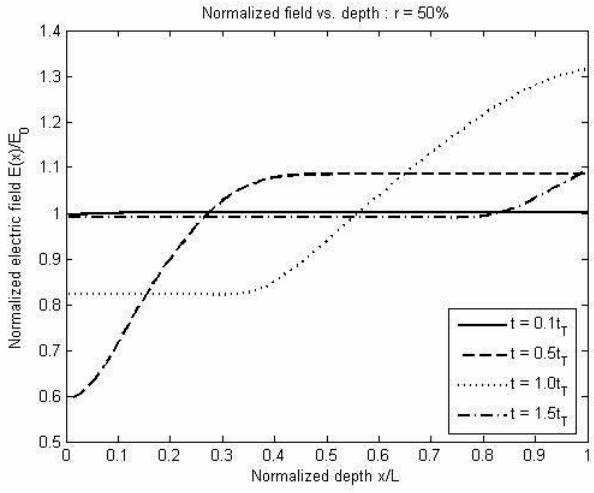
Normalized field vs. depth : r = 50%
Normalized electric field E(x)/E_0
Normalized depth x/L
t = 0.1t_T
t = 0.5t_T
t = 1.0t_T
t = 1.5t_T

(c)

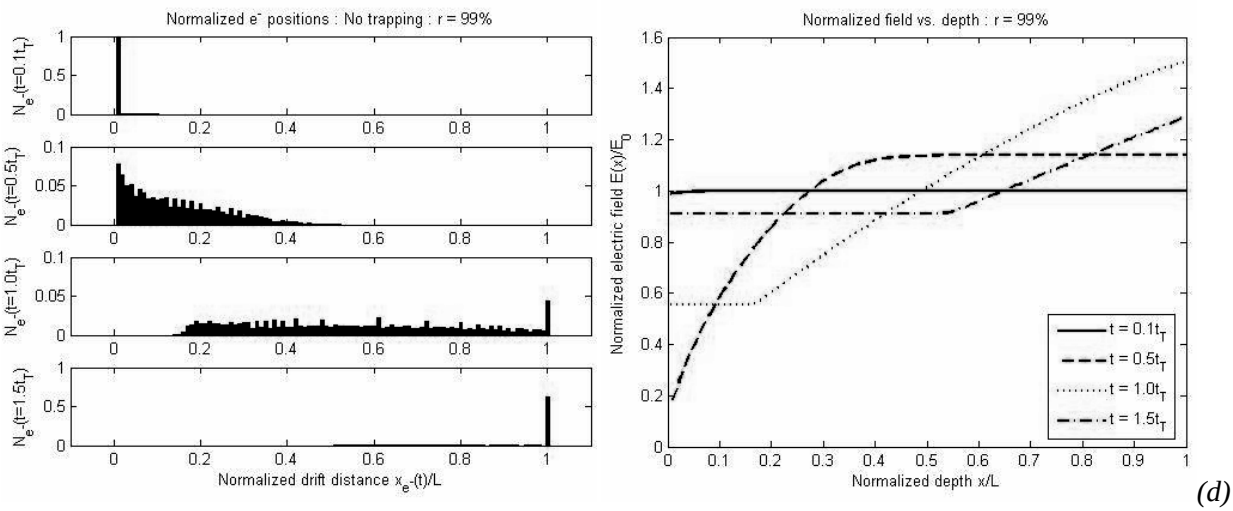

(d)

Figure 4-6: Carrier package distributions and corresponding electric fields for Gaussian generation time test for $\sigma = 0.1t_T$ at $t = 0.1t_T$, $0.5t_T$, $1.0t_T$, and $1.5t_T$ for (a) r = 0.01%, (b) r = 10%, (c) r = 50%, and (d) r = 99%

The position histograms and electric field plots of Figure 4-6 confirms first that the Gaussian spread of the test package set undergoes increased spreading with increased injection ratio, and secondly that the spread is more pronounced in the leading half of the moving pulse. This is as expected, since these packages have spent more time exposed to the dispersive effects.

4.1.3 Exponential distribution of absorption depth

This set of testing is used to illustrate the effects of the other generation related real-world analogue by simulating the exponentially decreasing absorption depth profile of the carrier packages. This is most easily simulated in generation by initializing the packages using the command line:

```
eSt(i,1) = exprnd(mu);
```

where `eSt(i,1)` is the current position of package `i` and `mu` is the mean absorption position. As explained in section 3.2.1.3, this creates an additional complication by necessitating the modelling of both carrier species, which share a common generation profile, but oppose each other in drift direction and electric field influence. Additionally, we know that the electron

microscopic mobility μ_e does not necessarily equal the hole mobility μ_h. Since tests are time-normalized against the electron transit time, electron mobility is kept constant in using the drift mobility ratio $b = \mu_e/\mu_h$ to set the hole mobility. Furthermore, the drift from the hole carriers produces its own current to compute dispersion from, as does the sum total of the electron and hole currents. These measured dispersions are listed below in Table 4-4. Note that the collection profile for hole carrier packages requires a different standard for dispersion measurement.

Table 4-4: Dispersion results for delta absorption depth tests

No trapping : Delta absorption Δ = 0.2L : Uniform excitation time = 0 : N = 10,000					
Plot on figures		Green	Blue	Black	Magenta
Injection ratio r		0.0001	0.10	0.50	0.99
Scale (carriers/package)		3.537×10^{7}	3.537×10^{10}	1.768×10^{11}	3.501×10^{11}
b = 0.1	e^- Dispersion D_e	0.1945	0.2786	0.5920	0.8106
	Total Dispersion D_t	0.1983	0.2715	0.5768	0.82343
b = 1.0	e^- Dispersion D_e	0.1907	0.2815	0.5335	0.7146
	Total Dispersion D_t	0.1992	0.2847	0.5935	0.7553
b = 10.0	e^- Dispersion D_e	0.1910	0.2877	0.5369	0.7436
	Total Dispersion D_t	0.1999	0.2811	0.5276	0.7358

Figures 4-7, 4-8, and 4-9 contain all of the TOF waveforms for testing in this series with mobility ratios of b = 0.1, 1.0, and 10.0 respectively. It is immediately evident that electron current is the dominant feature in determining the shape of the TOF curve. This is expected as the generation profile guarantees that the highest electron concentrations have the furthest distances to drift, while the highest hole concentrations are collected almost immediately. Intuitively, a reversal of the applied biasing field would likewise ensure that holes would be the dominant contributor to the generated photocurrent.

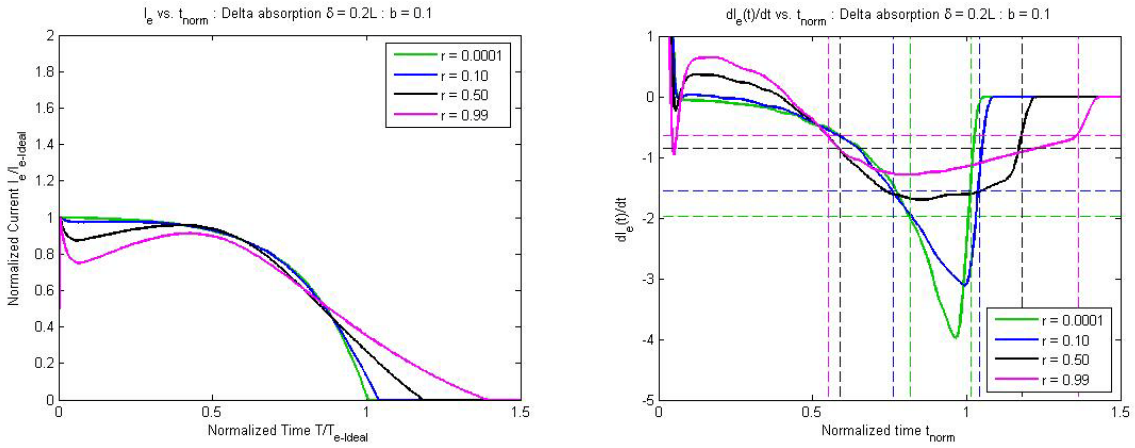

(a)

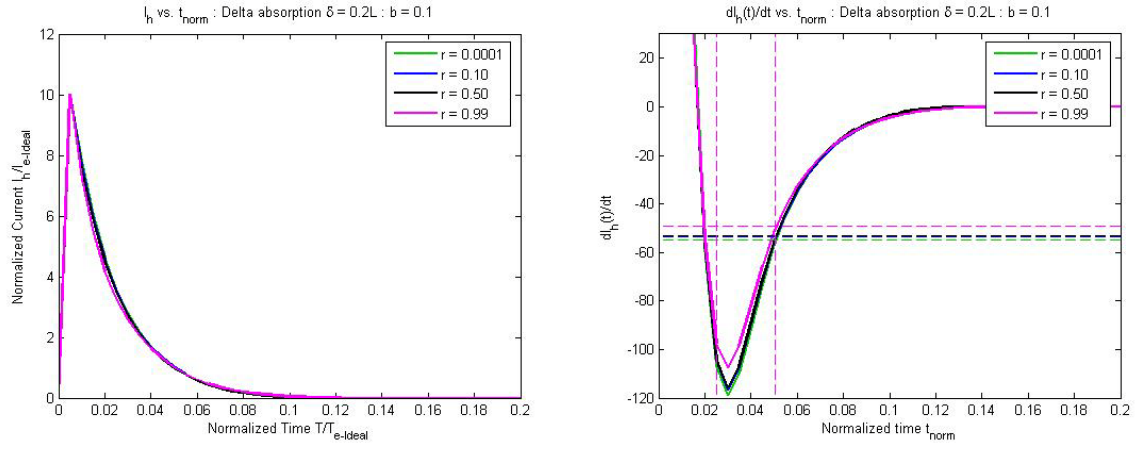

(b)

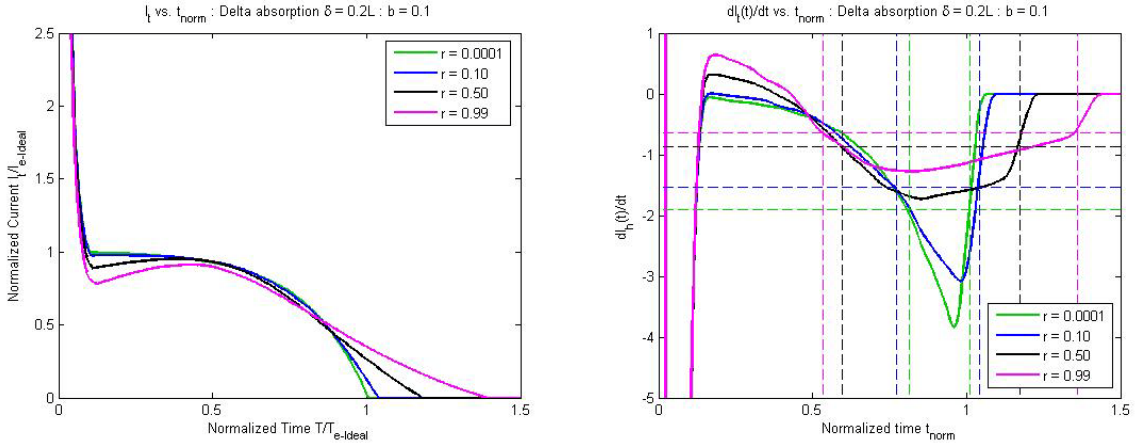

(c)

Figure 4-7: Generated photocurrents and their corresponding time derivative functions for delta absorption tests with mobility ratio b = 0.1 for (a)electron current $I_e(t)$, (b)hole current $I_h(t)$, and (c)total current $I_e+I_h = I_t(t)$.

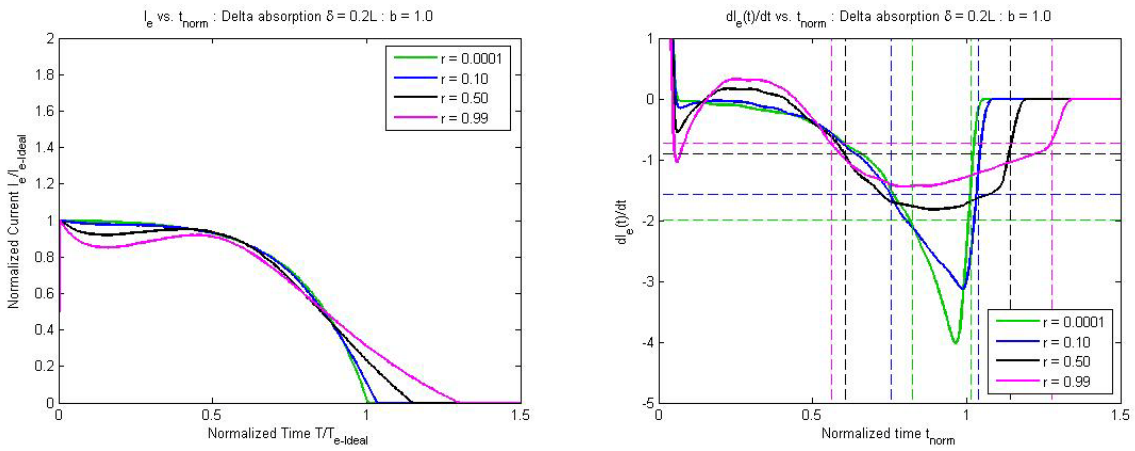

(a)

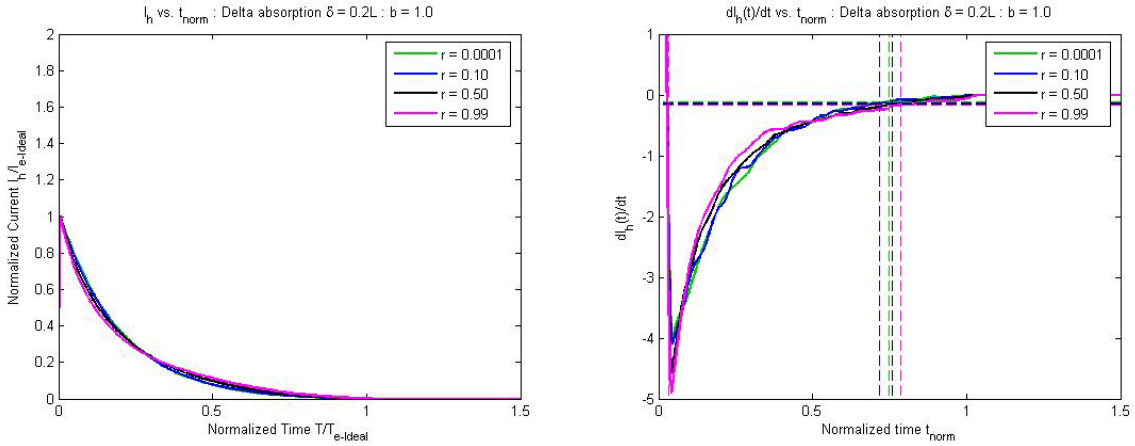

(b)

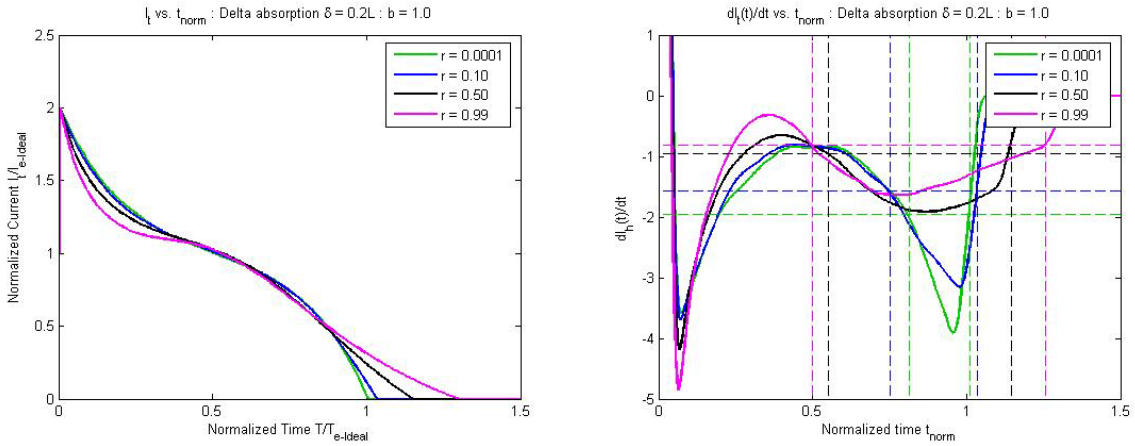

(c)

Figure 4-8: Generated photocurrents and their corresponding time derivative functions for delta absorption tests with mobility ratio b = 1.0 for (a)electron current $I_e(t)$, (b)hole current $I_h(t)$, and (c)total current $I_e+I_h = I_t(t)$.

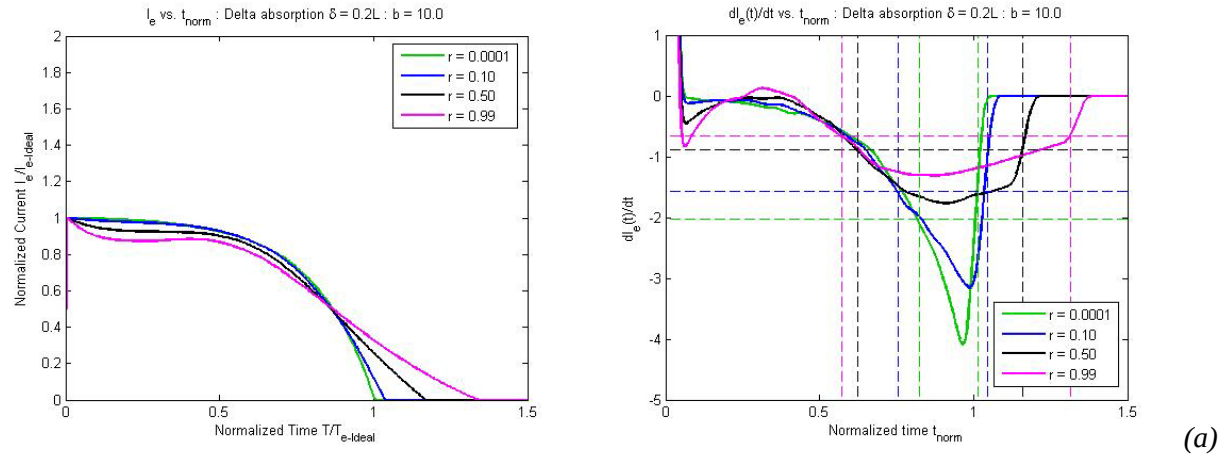

(a)

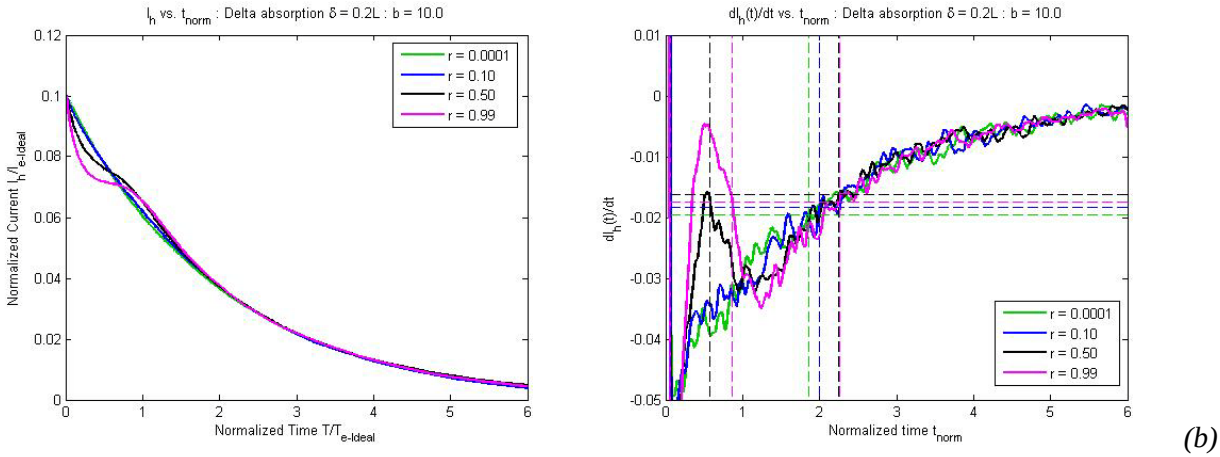

(b)

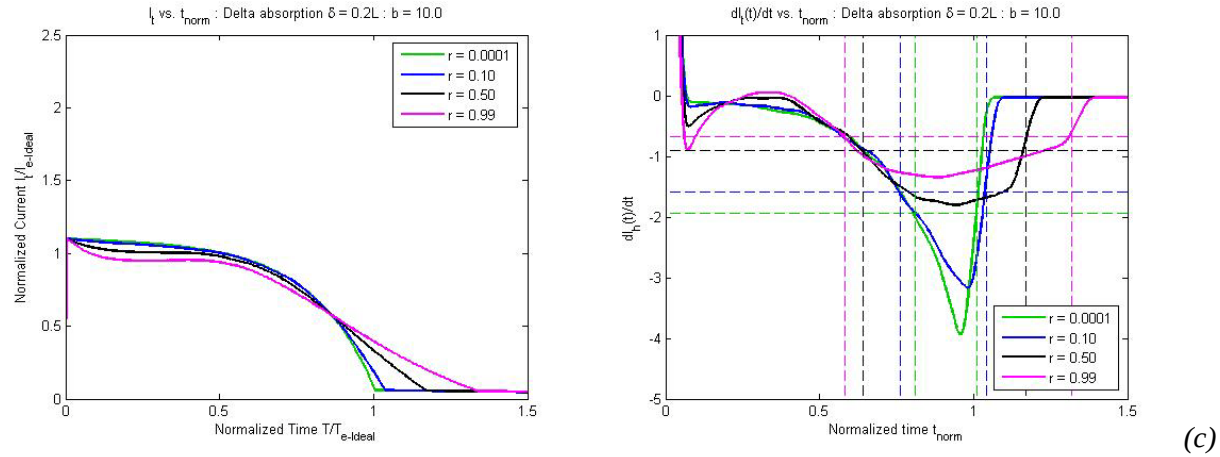

(c)

Figure 4-9: Generated photocurrents and their corresponding time derivative functions for delta absorption tests with mobility ratio b = 10.0 for (a)electron current $I_e(t)$, (b)hole current $I_h(t)$, and (c)total current $I_e+I_h = I_t(t)$.

The figures for the electron current all show an initial full normalized current which undergoes a slight dip before resuming the largely unimpeded flow rate. This occurs partially as a result of the high collection rate of the hole carriers and is more pronounced where the hole

carriers are more quickly collected. At the onset, because the carriers are all in such close proximity, there is only nominal disturbance of the electric field, and functionally no field balancing to influence the generated current. As hole carriers are removed from the field calculations, the electric field becomes more influenced by the field effects caused by the electron packages, which now exist in higher abundance. As the carrier count imbalance tilts more, the field balancing factor rises and factors more into the average drift of each package and the subsequent current generated. As the bulk of the electron packages passes through the medium, the balancing factor loses potency because the carriers are undergoing acceleration in their rate of collection, which counters the current gains due to acceleration caused the shifting field balancing. Figure 4-10 shows how the field balancing is influenced by the collection rates.

This is important because the field balancing is the primary mechanism driving the perturbation of the electric field. In the low mobility ratio case, a negative peak appears to occur near to the time when hole collection approaches completion because the electrons are still primarily distributed towards the front of the bulk when the holes leave the system. Interestingly, a negative peak does not appear in the field balancing plots for mobility ratios of unity or higher, which show a near or total lack of any below-zero time period for $C_E(t)$, implying that electron carriers maintain an accelerated drift speed for the entire duration of drift. The drift speed gains expected of this, however, are overwhelmed by the attractive pull of the hole carriers, resulting in the persistently reduced transient electron current seen in Figure 4-9(a).

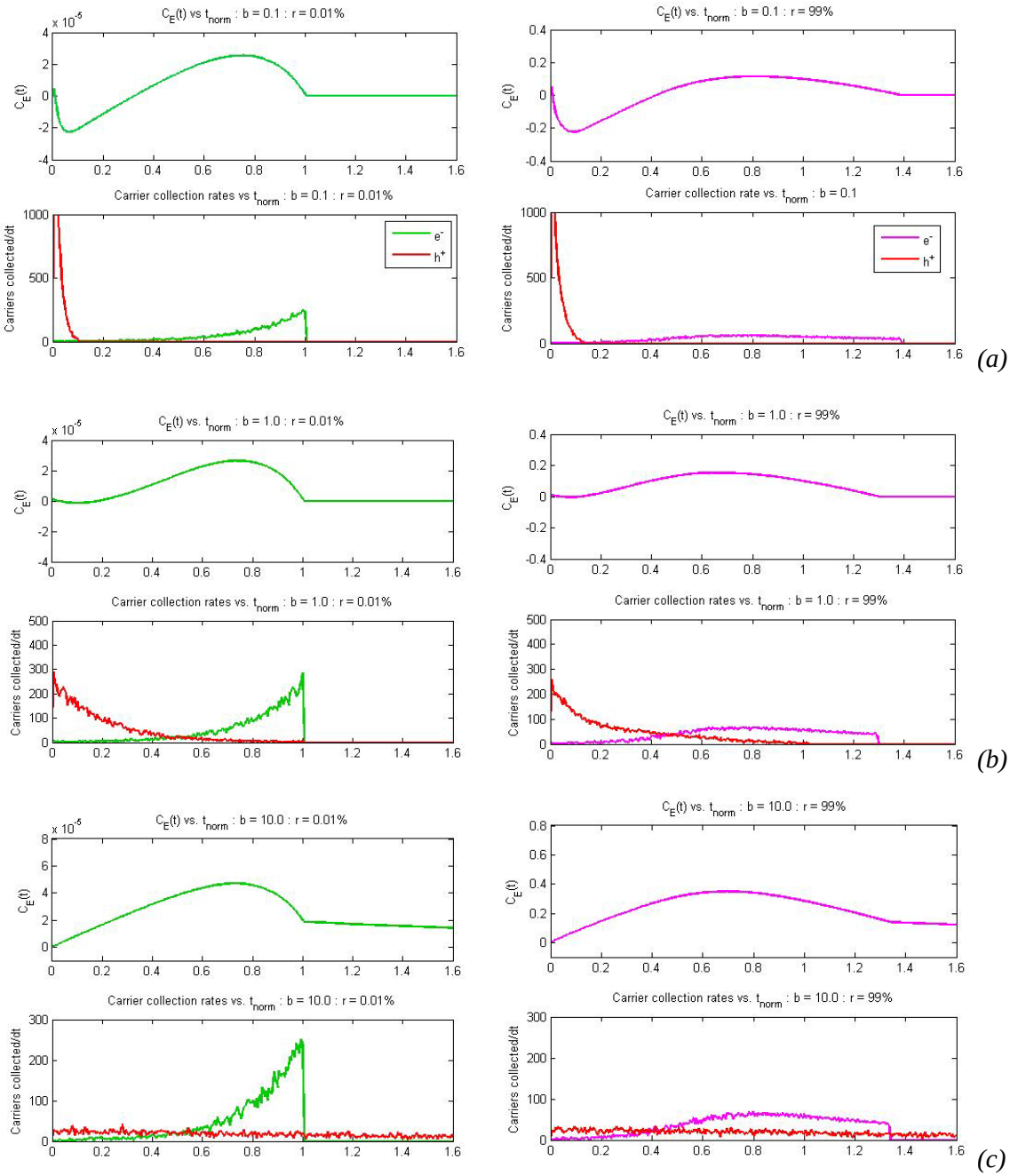

Figure 4-10: $C_E(t)$ compared to number of each carriers type collected per time step dt for ratios of r = 0.0001 and 0.99 and mobility ratios (a) b = 0.1, (b) b = 1.0, and (c) b = 10.0

A sampling of the electric fields themselves as compared to the placements of the carrier packages are shown below in Figure 4-11. In the low injections cases, the carrier distribution is unchanging as before. At higher injection, the package distribution flattens out in a way that obscures the initial exponential shape of the carrier package profile. This flattening of the

distribution can be seen in the linearization of the transient photocurrent curve seen in figures 4.7-9(a) and in the electric field plots of Figure 4-11(c) and (d).

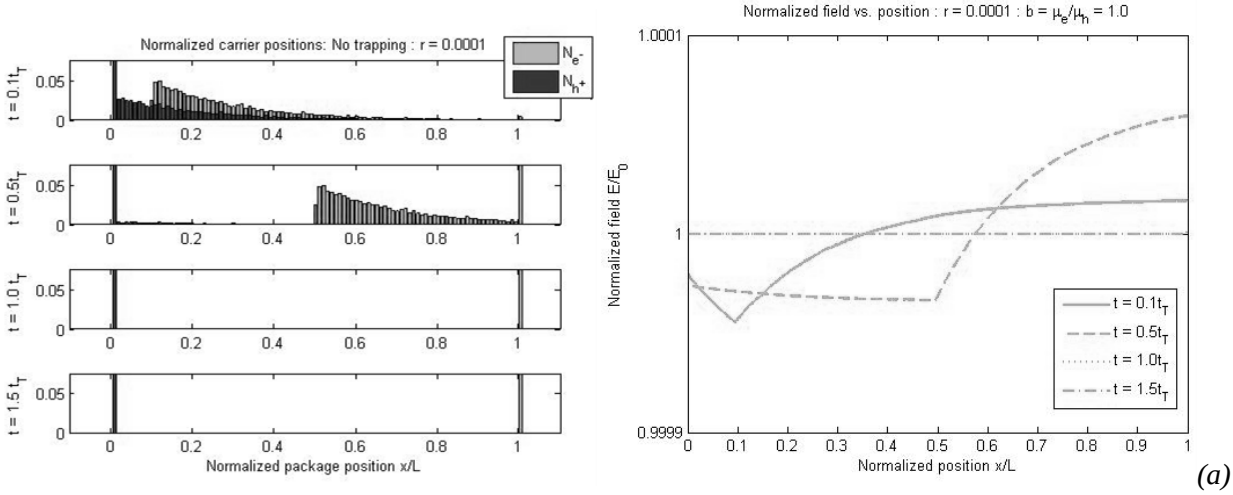

(a)

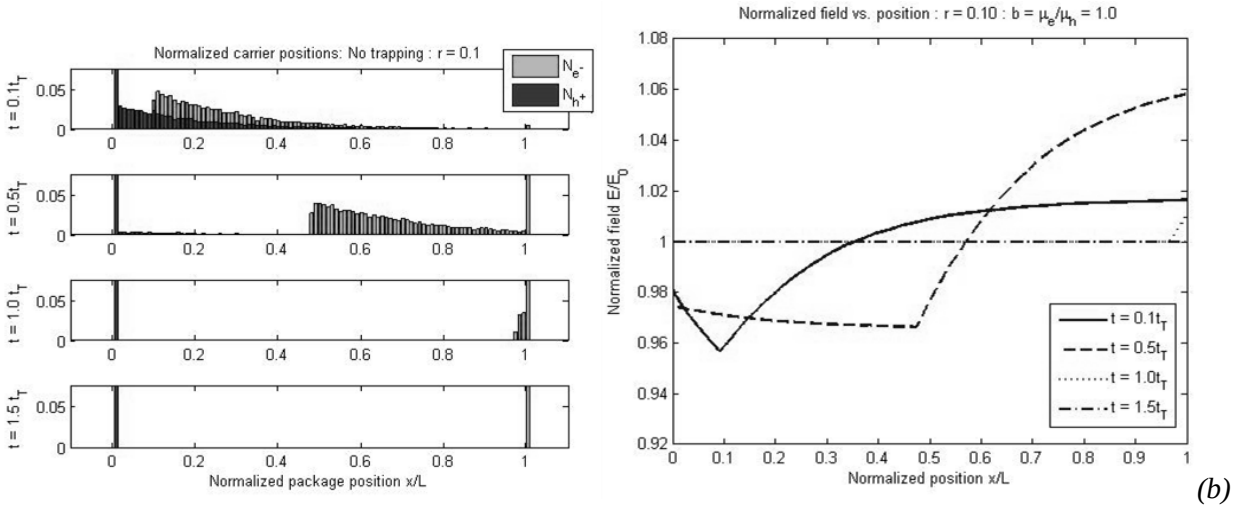

(b)

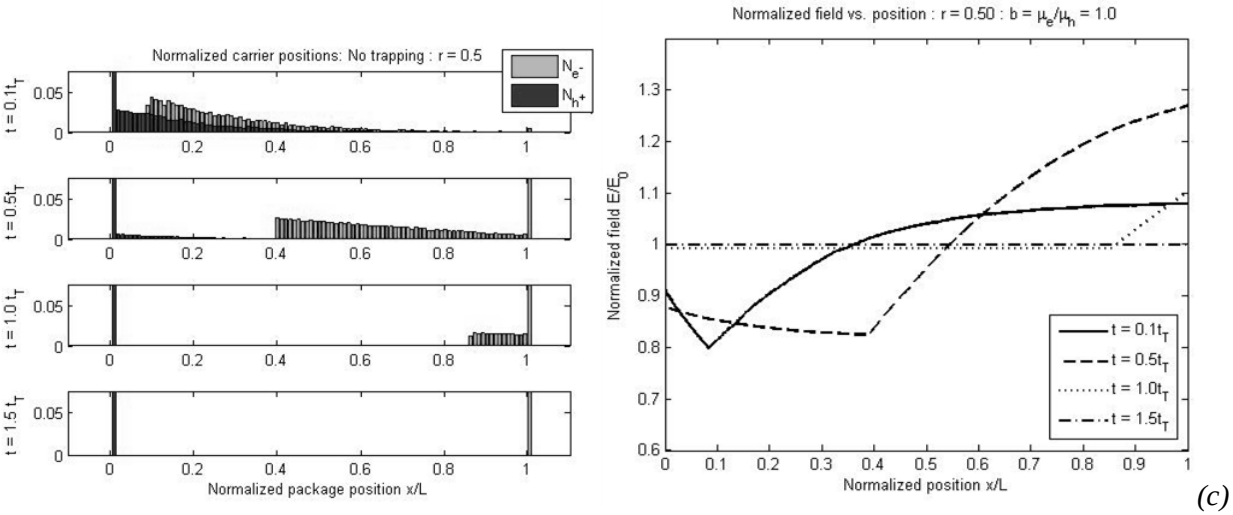

(c)

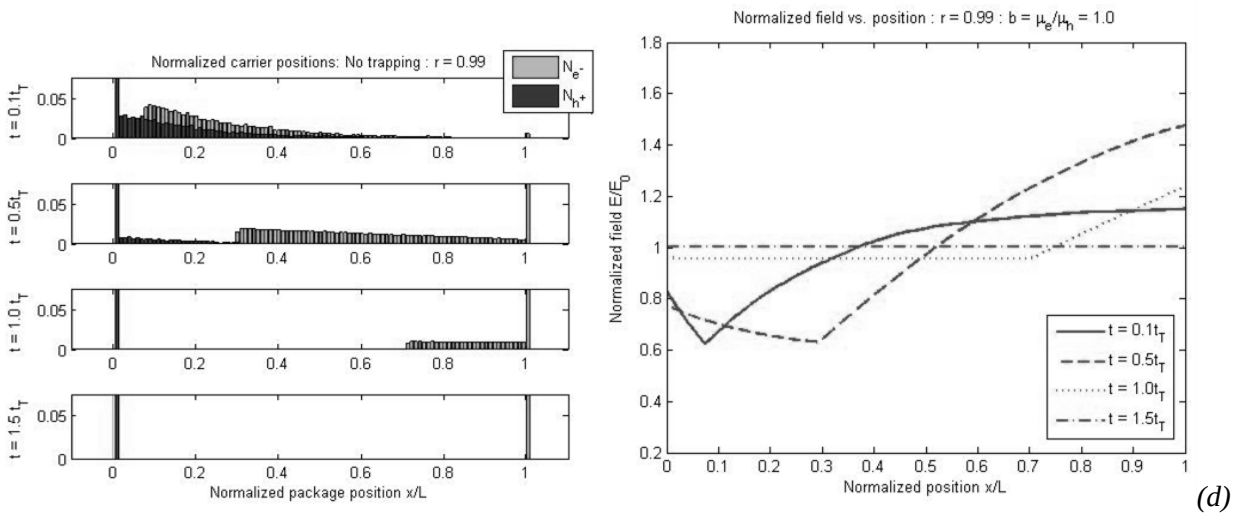

Figure 4-11: Carrier package distributions and corresponding electric fields for delta absorption testing with mobility ratio = 1.0 for injection ratios (a)0.0001, (b)0.10, (c)0.50, and (d)0.99

4.2 Phase Two

Phase two of testing incorporates the field perturbing model used in Phase One, but in lieu of generation characteristics being used as the initial dispersive element expanded by field perturbation, Phase Two serves to evaluate the TOF trap-release model as the carrier dispersive mechanism. This model recreates a simplified amorphous semiconducting environment by simulating the localized states that limit the flow of drifting carriers. Though, as demonstrated in section 4.1.3, both species of carrier can be readily simulated, this model will tentatively be used to evaluate the effect of high charge injection on the electron photocurrent only. Artificially limiting the test platform in this way allows us to easily confirm that it behaves according to expectations for known cases of low injection, so as to validate that it can indeed be used for the less investigated cases of high carrier injection.

The test plan is as outlined in section 3.2.2. Tests are performed for all schemes for injection ratios of *r = 0.0001, 0.10, 0.50,* and *0.99*, with the lowest ratio being the reference case for low injection expectations. Phase two, as detailed prior, is divided into three sections characterized

by the trapping routine. The first goal of this phase is to affirm that expectations for the mobility reduction factor θ as listed in section 3.2.3 - conforms to experimental results, and identify the cause for discrepancies. The second goal is to establish a relationship between injection ratio and dispersion. The third is to use these results to identify the practical uses best served by injection ratio testing.

4.2.1 Discrete shallow trapping

Part one of phase two is the simulation of singular discrete trapping depth. This is the simplest way to evaluate the mobility reduction factor θ because the output results are free of interference from variance in the component factors governed by θ. This round consists of a total of 36 simulations; accounting for direct modulation of capture time τ_C, indirect modulation of release time τ_R through θ, and injection ratios of 0.01%, 10%, 50%, and 99%. Statistics to be recorded include trapping incidence count, test runtime, energy depth corresponding to release time for the parameters used for a-Se simulation, measured average capture and release times, and measured dispersion. Results for each set of tests are organized as shown in Table 4-5 to simplify comparisons between results for each injection ratio.

Table 4-5: Typical single discrete trap level test results

Single Discrete Level Trapping : Uniform generation position and time = 0 : τ_C = 0.001 t_T : θ = 0.001 : τ_R = 0.999 t_T : N = 10,000				
Injection Ratio	r = 0.01%	r = 10%	r = 50%	r = 99%
Scale	3.537×10^{7}	3.537×10^{10}	1.768×10^{11}	3.501×10^{11}
Time steps used	707,898	816,500	826,038	1,192,017
E_S for $f=10^{11}Hz$	0.4069	0.4069	0.4069	0.4069
Trapping events	6,650,807	6,680,886	6,875,695	7,636,940
Avg. capture time t_C (t_T)	0.0010009	0.0010005	0.0010006	0.0010006
Avg. release time t_R (t_T)	0.99863	0.99850	0.99902	0.99891
Charge collected	90.00	100.00	90.00	100.00
Dispersion D (t_T)	80.304	114.419	288.195	440.625

The particular tests detailed in the above table represent some of the longest simulations performed in this work, with a maximum runtime of 1.19 million steps translating into 1,192 transit times t_T. This corresponds to ~7.5 million trapping events and an equal number of release events. This averages to roughly 13 trap/release events per time step. Related simulations using θ of 0.01 and 0.1 likewise yield averages of 102 and 1,012 events per time step respectively. At equilibrium, the trap events and release events are equal in both rates of incidence and magnitude of effect on current (that being $\delta i = \pm 1/N$). The mean current change per time step, obviously, is theoretically zero prior to commencement of collection (notwithstanding the carrier acceleration from the field perturbation). The law of large numbers holds that the higher the number of state change events: the more probable their sum effects will trend toward the mean of zero, so while the rates of state changes are in proportion to the transient equilibrium current, the total sum of the higher state change rate tests are more balanced, manifesting as a reduction in the apparent noise in each waveform as seen in Figure 4-12.

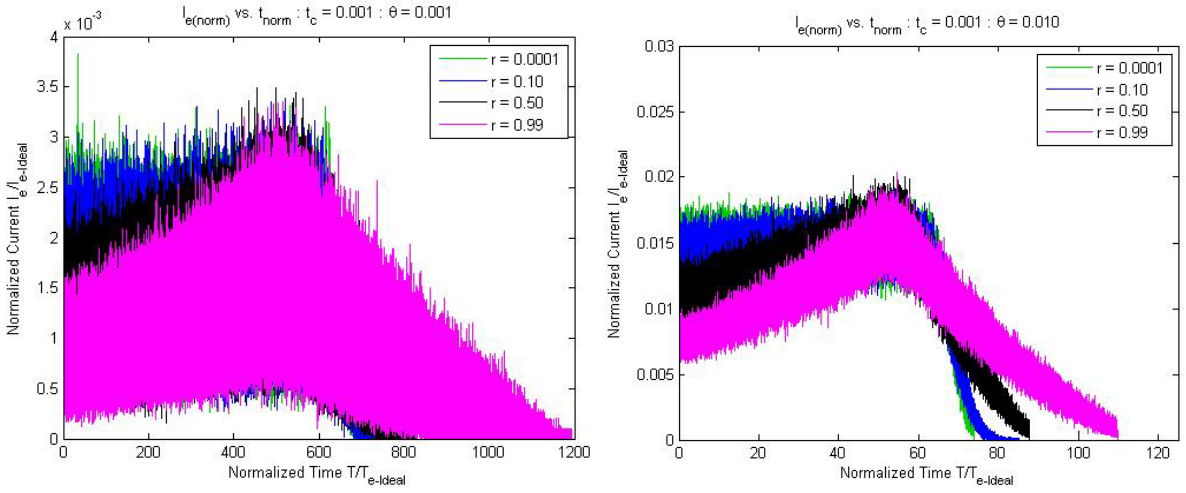

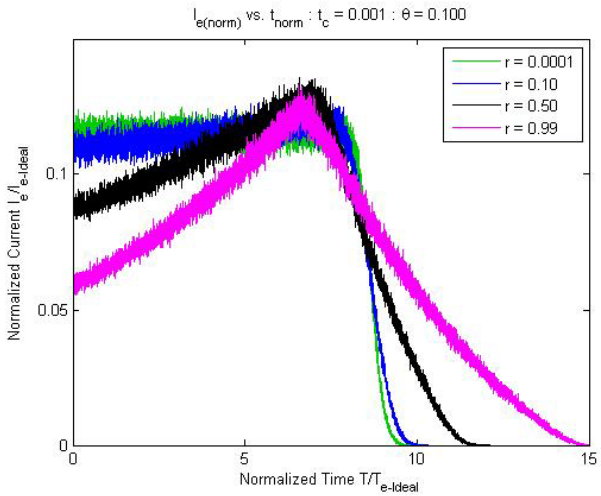

Figure 4-12: Example of noise prevalence as a product of θ, which governs the equilibrium current level.

The low θ case best illustrates the challenge in reducing the noise caused by the relatively low event incidence. The low injection ratio case returns a high noise curve, but the magnitude is relatively constant. By comparison, the highest injection ratio case shows a weakened initial noise profile which ramps up as the bulk of the carriers accelerate over time. This is a clear product of the individual current contributions being of reduced - but increasing - influence due to field perturbation in the field balancing factor $C_E(t)$, and is less pronounced where higher state change event rates balance toward zero. The primary challenge presented by this noise is in isolating the general trend from which dispersion can be measured. Where the noise filtering techniques applied are too strong, characteristic high points such as the knee of the curve can be lost in a moving average filter. Typically, once filtered, results are sampled down from their initial time step count to 200, where a much weaker moving average filter will then clean out the highest frequency noise. Final results are all presented below in Figures 4-14, 4-15, and 4-16, though bumpy results such as in 4-14(c) demonstrate that a better means for filtering the raw TOF waveform is desirable.

For purposes of comparison, dispersion results obtained from these studies are listed below in Table 4-6. Dispersion results are presented as a direct measurement for the low injection case which is then used as the baseline value for which the other dispersion values are presented as multiples of.

Table 4-6: Dispersion results for single discrete level trapping model. Results for higher injection ratios are also normalized against that of the low injection case.

τ_{CS}	θ	r = 0.0001	r = 0.10		r = 0.50		r = 0.99	
		$D_{0.0001}$	$D_{0.10}$	$\frac{D_{0.10}}{D_{0.0001}}$	$D_{0.50}$	$\frac{D_{0.50}}{D_{0.0001}}$	$D_{0.99}$	$\frac{D_{0.99}}{D_{0.0001}}$
0.001	0.001	80.304	114.419	1.4248	288.19	3.5887	440.63	5.4870
0.001	0.01	10.681	12.58	1.1778	28.697	2.6867	54.756	5.1265
0.001	0.1	0.817	1.2658	1.5499	3.3782	4.1364	5.3853	6.5940
0.01	0.001	225.283	281.286	1.2486	355.479	1.5779	508.919	2.2590
0.01	0.01	25.341	28.044	1.1067	33.031	1.3035	44.799	1.7678
0.01	0.1	2.749	3.2702	1.1896	4.1505	1.5098	6.2615	2.2777
0.1	0.001	586.752	706.747	1.2045	620.748	1.0579	661.833	1.1280
0.1	0.01	59.937	66.0863	1.1026	61.7002	1.0294	54.0049	0.9010
0.1	0.1	8.610	9.1936	1.0678	7.8268	0.9090	8.2336	0.9563

The first thing to note is in the initial values for $D_{0.0001}$, which inversely follow θ in order of magnitude. Figure 4-13 shows this dependency of the dispersion on the injection ratio for multiple combinations of τ_C and θ. As θ dictates the expected testing time, it is expected that the dispersion should be of the same scale. What does seem evident, however, is that the capture time seems to be the more relevant factor in larger dispersion values, and this can be seen in the TOF waveforms, where modulating τ_C has a much greater influence on the curvature than does modulating θ. Notable, in the derivative plots, is a loss of symmetry at the injection ratio increases. Typically, the FWHM techniques used are best applied to symmetric Gaussian shapes, but they should still be applicable here. The asymmetry is a product of the electric field gradient, which slows the trailing half of the otherwise Gaussian distributed packet while the leading half is being collected.

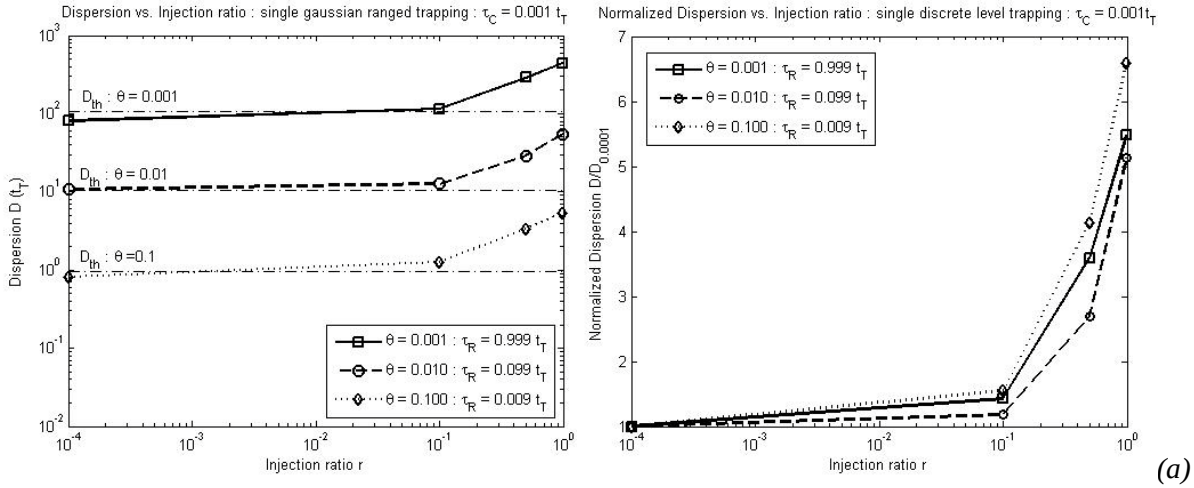

(a)

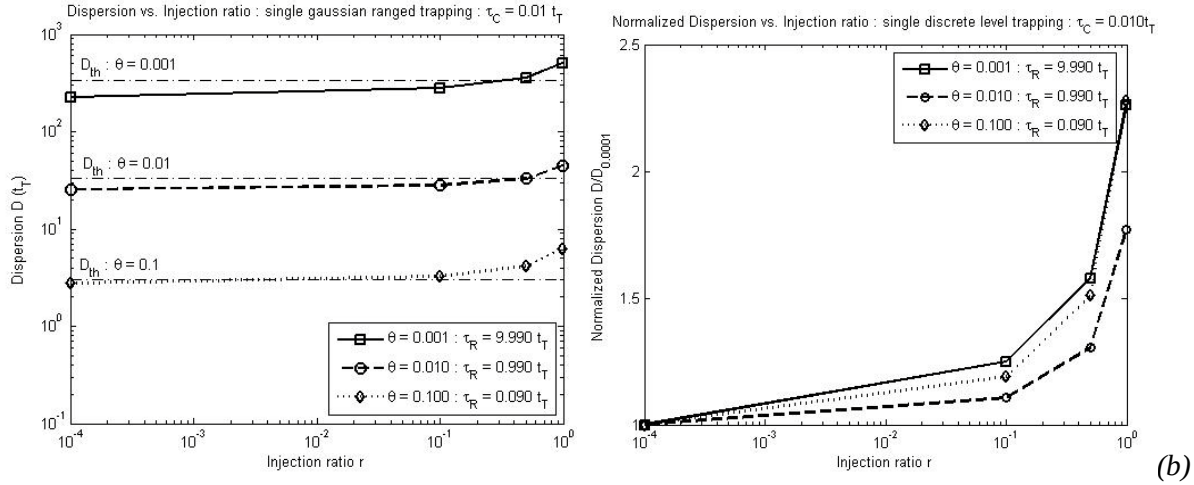

(b)

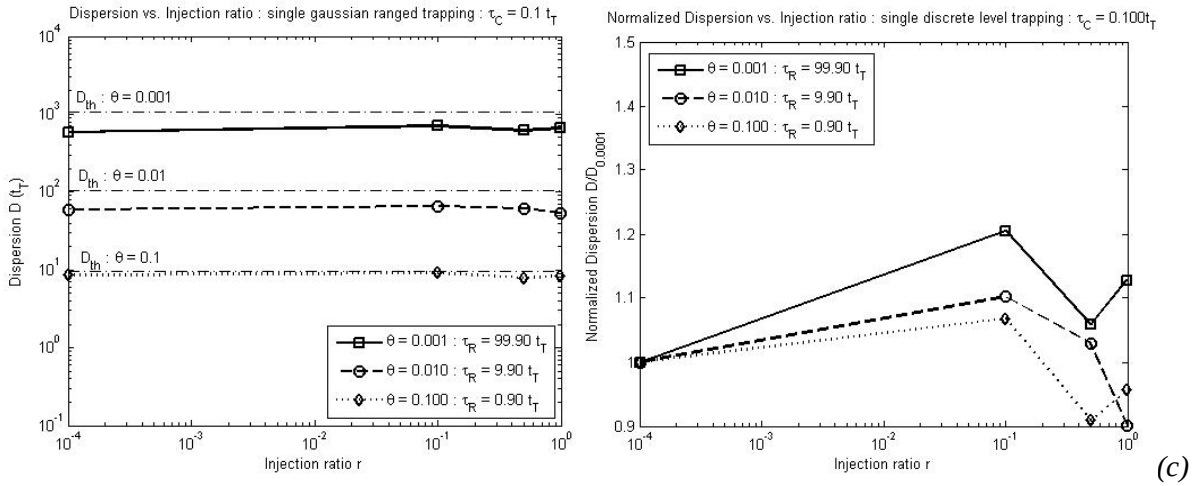

(c)

Figure 4-13: Dispersion D and $D/D_{0.0001}$ compared against the injection ratio r, including the theoretical low-injection dispersion values D_{th} as computed from Eq 2-11 for (a) $\tau_C = 0.001\ t_T$, (b) $\tau_C = 0.010\ t_T$ and (c) $\tau_C = 0.100\ t_T$.

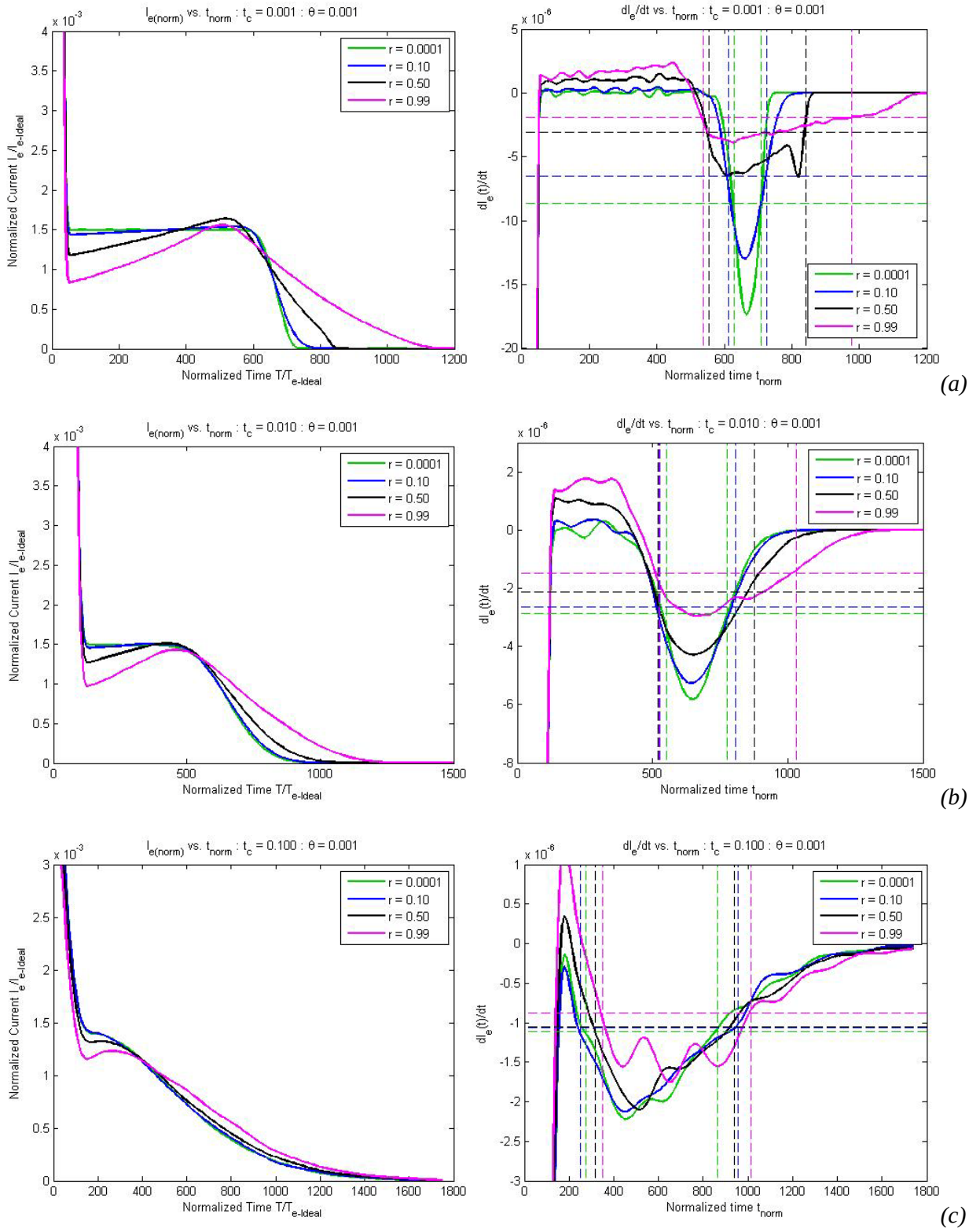

Figure 4-14: TOF transient photocurrents for single discrete level trapping simulations with θ = 0.001, and τ_C = (a)0.001, (b)0.010, and (c)0.100

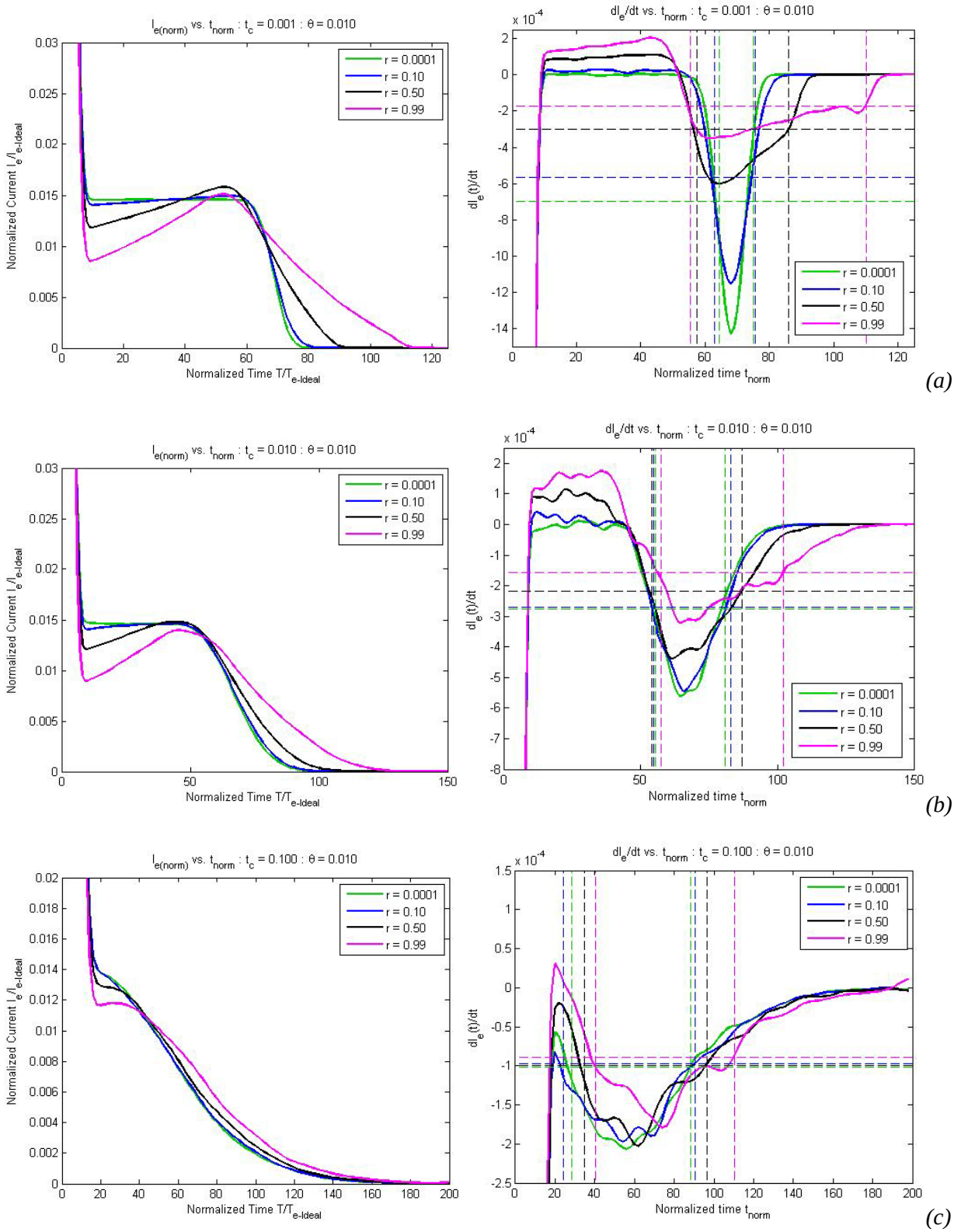

Figure 4-15: TOF transient photocurrents for single discrete level trapping simulations with θ = 0.010, and τ_C = (a)0.001, (b)0.010, and (c)0.100

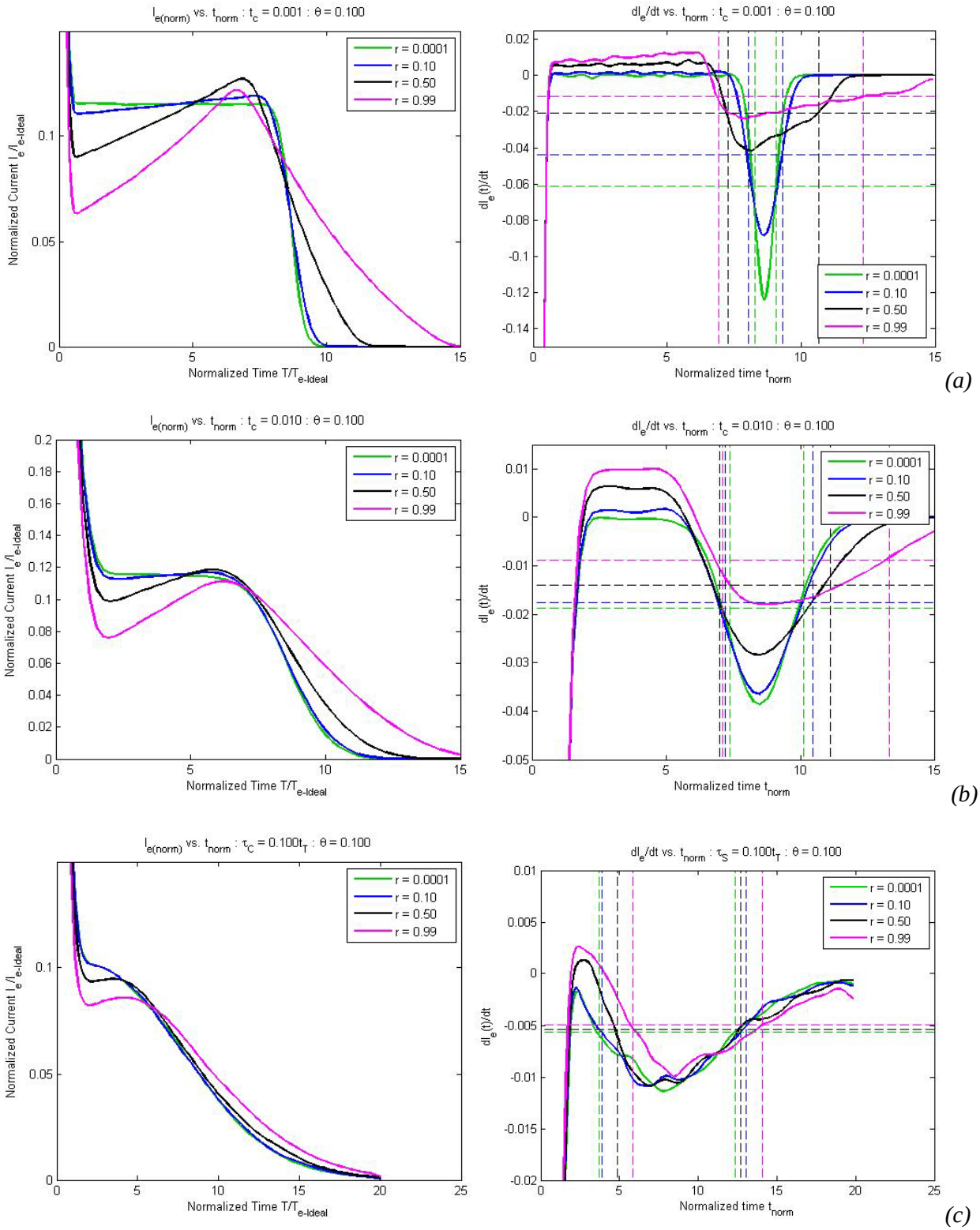

Figure 4-16: TOF transient photocurrents for single discrete level trapping simulations with θ = 0.100, and τ_C = (a)0.001, (b)0.010, and (c)0.100

Another metric by which these results can be evaluated is in the measured transit times. A few means exist to determine these times; each relying on a specific feature of the transient photocurrent signal. The first time, t_{inf}, comes from the time position of the inflection point in the collection period; denoted by the negative peaks which correspond to the points of highest collection. The second method involves measuring the time, $t_{1/2}$, at which the transient photocurrent drops to half that of the peak photocurrent at detailed balance. The third method used here measures the time, t_{knee}, which marks the transition point between detailed balance and collection. Figure 4-17 contains a select set of these measurements, which show little proportional change between varying values of θ, but much more between varying capture times.

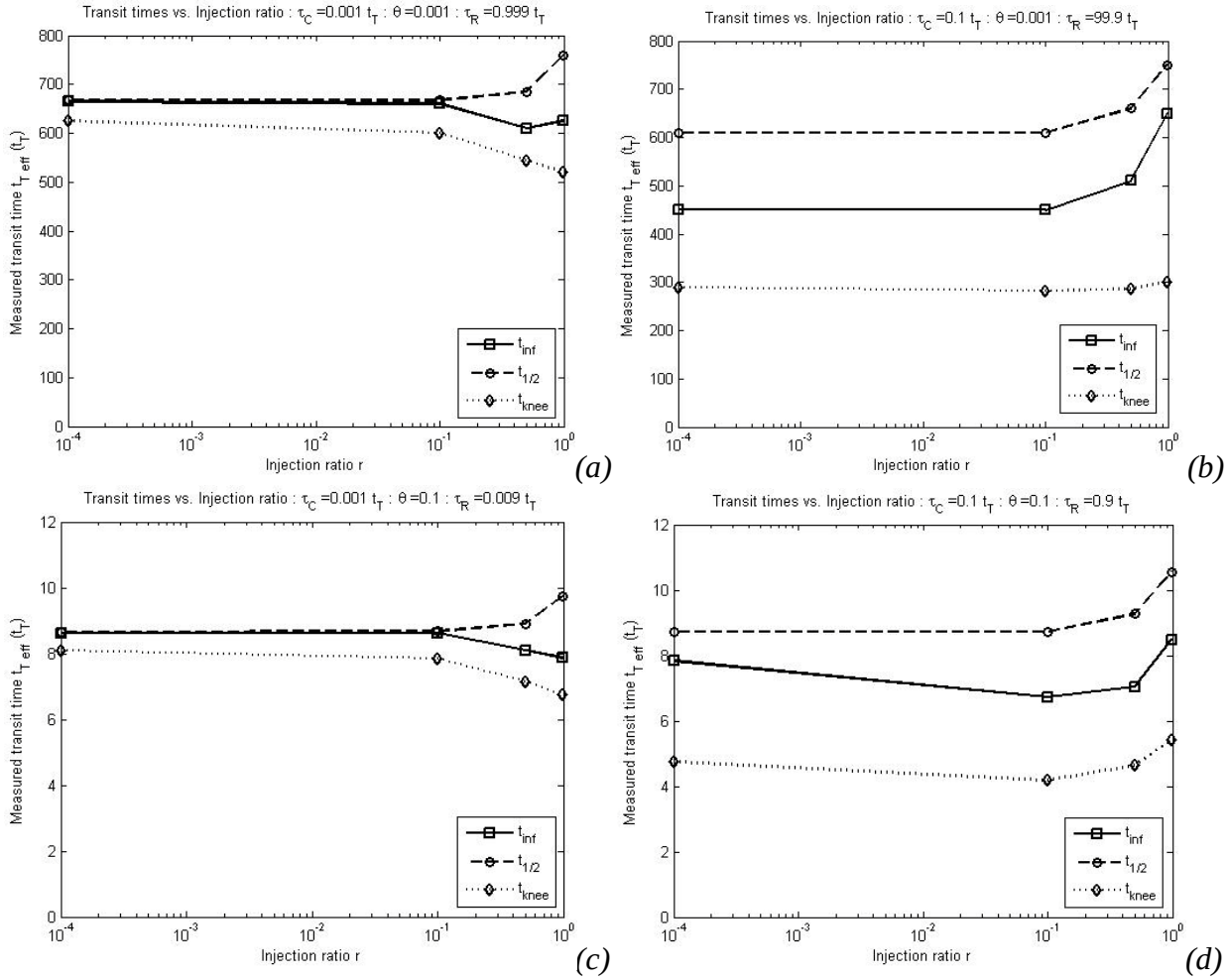

Figure 4-17: Transit times for monoenergetic trap tests showing all time measurements for τ_C and θ = (a) 0.001 t_T and 0.001(b) 0.001 t_T and 0.1 (c) 0.1 t_T and 0.001 (d) 0.1 t_T and 0.1.

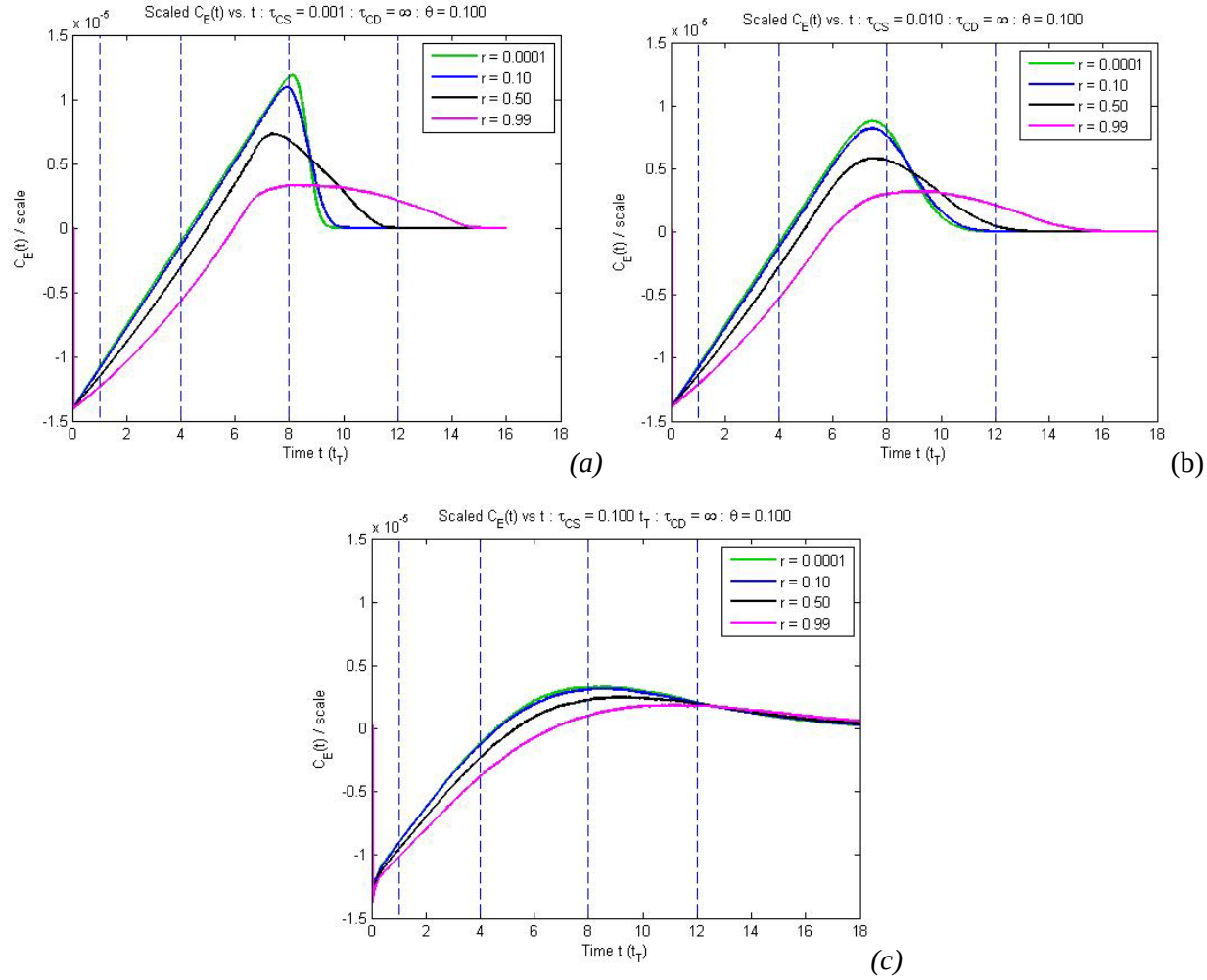

Figure 4-18: Scale adjusted field balancing $C_E(t)$ plots for all injection ratios using capture times of τ_{CS} = (a) 0.001 t_T, (b) 0.010 t_T, and (c) 0.100 t_T

As can be inferred from the plots, simulations where the parameters led to a sharp well-defined knee in the curve made for the shortest dispersion times, and all of those were cases where capture time τ_C was at its lowest. These were also the cases where dispersion was most influenced by the injection ratio. Examination of the field balancing functions $C_E(t)$ in Figure 4-18 reveals that the highest capture times resulted in the least – but most prolonged – overall disruption in the field, and that the difference in the perturbation between injection ratios for these cases is nominal.

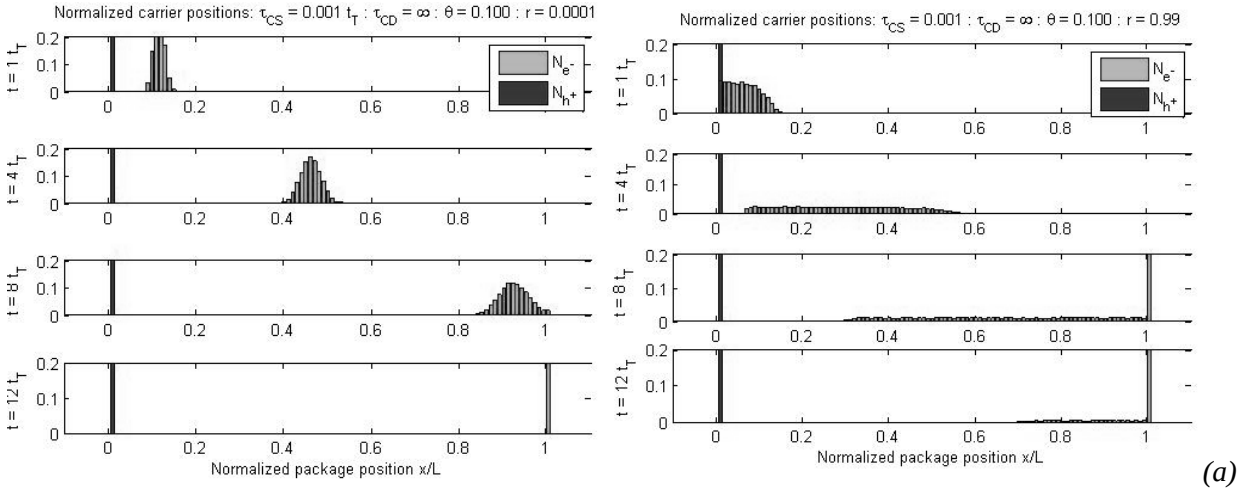

(a)

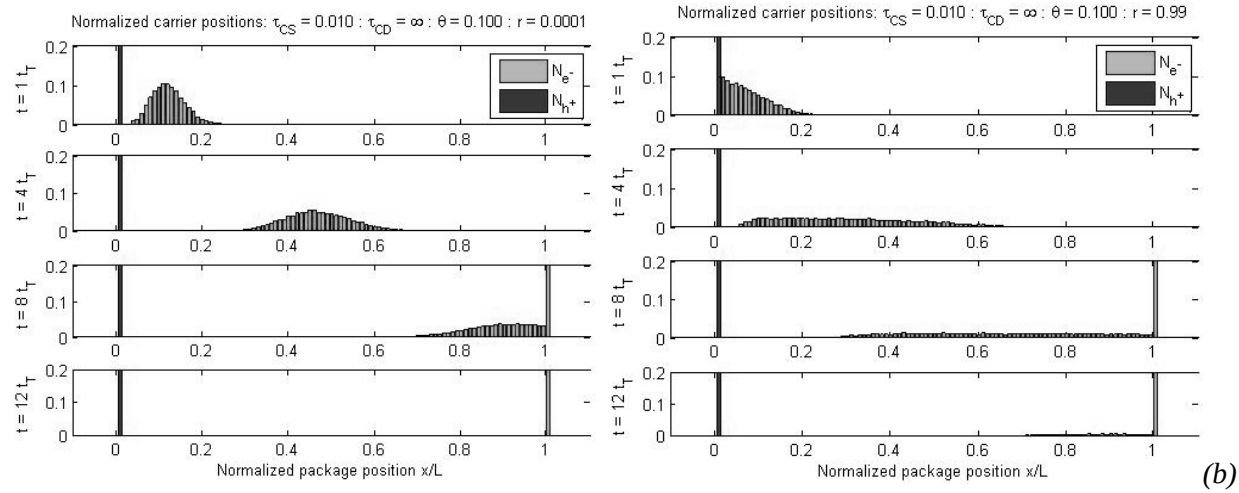

(b)

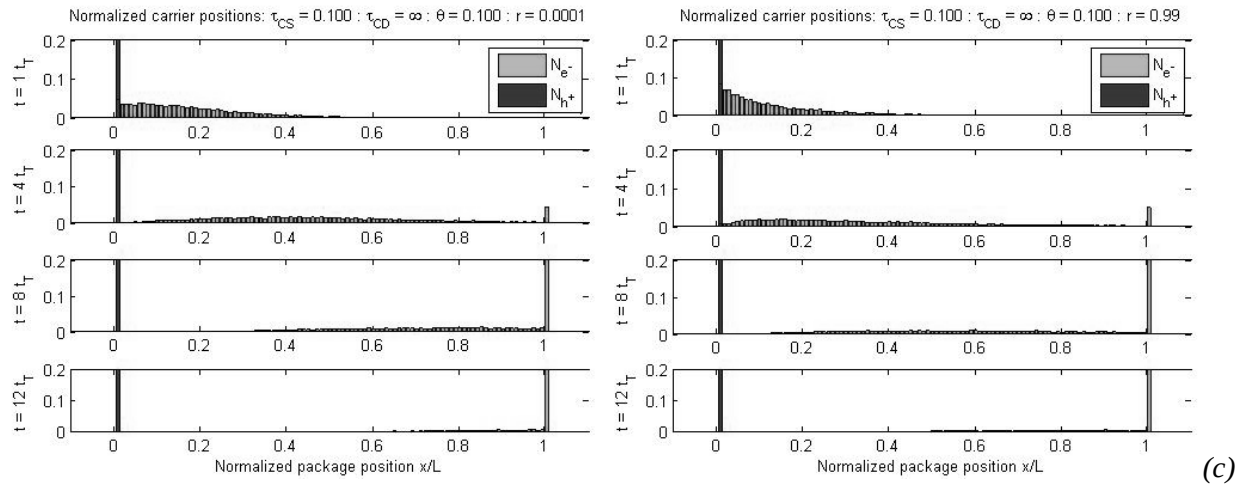

(c)

Figure 4-19: Carrier position histograms for the lowest and highest carrier injection cases for τ_{CS} = (a) 0.001 t_T, (b) 0.010 t_T, and (c) 0.100 t_T

The reason for the reduction in the field balancing profile for high capture times is visible in Figure 4-19, which shows that high capture times result in a faster loss of carrier package cohesion. Under low injection, the carrier package spreading occurs at a rate dictated by the capture times. Since the capture time determines the average pre-capture drift distance, and difference in the capture times between tests is by a factor of 10, the amount of expected full spread increases by a factor of 10 for each successive test. From the low injection cases of figures 4-19a and 4-19b, we see that the carrier distribution profile at 8 t_T for $\tau_C = 0.001t_T$ ($\tau_R = 0.009\ t_T$) is comparable to that of $\tau_C = 0.01\ t_T$ ($\tau_R = 0.09t_T$) at the time of 1 t_T. This observation does not hold for the high injection cases, where package cohesion is quickly lost to the high influence of the electric field gradient and exacerbated by mere existence of trapping processes.

For the highest capture time, because the package cluster loses cohesion as a result of trapping effects, the gradient across the electric field broadens out, resulting in a lower total potential in the injected charge field, and thus a lowing in the prominence of the field balancing as seen in Figure 4-18. Because collection begins relatively early, the effects which result from the high charge injection are mitigated before their full effect is realized. For these reasons, the high injection cases show comparatively little deviation from the baseline low injection case in both TOF waveforms and their corresponding derivative functions from which dispersion is measured.

4.2.2 Discrete bi-level trapping

Part two of Phase two builds upon the previous model and brings it more inline with real-world applicability by slightly diversifying the trapping scheme; specifically, by implementing trapping states corresponding to a functionally infinite release time. Though deep trapping states have release times governed by the same thermal excitation rules as shallow states, their release

rates in this work are arbitrarily set to zero, so as to identify how long-term trapped carriers influence the θ modified drift of their free counterparts. This manifests first as an attenuation of the current, as deep trapped carriers offer no contribution to the transient photocurrent, and secondly as a permanent layer of carriers propelling the free carriers through the medium via mutual repulsion.

The first manifestation provides for the main complication in this phase of work, in that by reducing the number of free carriers, we increasingly limit the number of transition events, which causes loss of resolution in the data. Firstly, this loss of resolution makes the waveform less readable by overvaluing the contributions of fewer carrier packages, thus increasing the amount of noise to process out, which increases the risk of losing characteristic data features to noise reduction routines. Secondly, the loss of carriers contributes to time dependent attenuation of these same characteristic features, and appears on the derivative function as an upward slope that may not reach the halfway point of the collection peak, which makes dispersion calculation impossible. To compensate, and identify the dispersion among those which *are* collected, it would be necessary to identify, in advance, which carriers are to avoid being deep trapped so as to generate a secondary current plot showing only their contributions. Between the loss of resolution and the interference in dispersion measurement due to current attenuation, many of the tests in the phase produced immeasurable results. The other alternative is to boost the number of carriers modelled as described in section 3.1, though this has the cost of considerable added computation time.

Table 4-7: Typical test results for one set of injection ratio tests for bi-level trapping model

Dual trap level - Variable E – Shallow traps : τ_{CS} = 0.001 t_T : τ_{CD} =1/3 t_T : θ = 0.001 : τ_{RS} = 0.999 t_T : τ_{RD} = ∞ : dt = 0.001 t_T				
Property	r = 0.01%	r = 10%	r = 50%	r = 99%
Scale (e^- per package)	3.537×10^7	3.537×10^{10}	1.768×10^{11}	3.501×10^{11}
Time steps used	771,331	781,797	871,802	953,172
Trap depth E_s	0.4069	0.4069	0.4069	0.4069
Shallow trap count	2,902,724	2,893,664	2,888,750	2,943,330
Avg. shal cap time t_{CS}	0.0009966	0.00099616	0.00099679	0.00099629
Avg. shal rel time t_{RS}	0.99903	0.99870	0.99970	0.99912
Deep trap count	8,605	8,638	8,605	8,755
Avg deep cap time t_{CD}	0.0009886	0.00099065	0.00099331	0.00098557
% charge collected	13.95	13.61	13.95	12.45
Dispersion D	108.646	118.176	Indeterminable	548.885

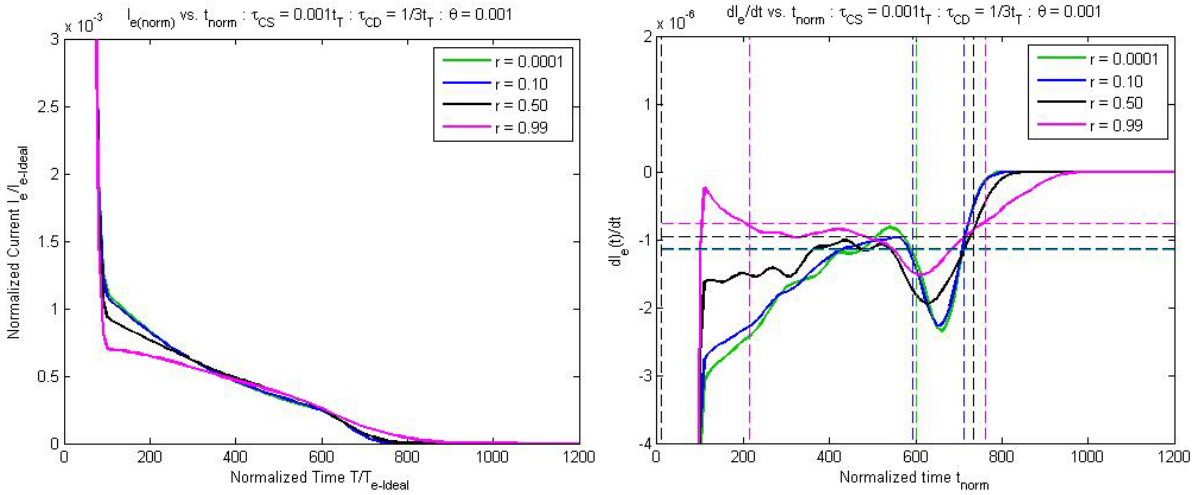

Figure 4-20: TOF transient photocurrent and derivative function corresponding to testing data listed in Table 4-7. Note that the r = 0.50 case returned a curve for which FWHM measurement could not be used to identify the dispersion, while the r = 0.99 case returned a distorted dispersion value.

Table 4-7 and Figure 4-20 show the results for testing of the highest deep capture rate as applied to the same parameters as the simulation set represented in Table 4-5. Given a low deep trap capture time of $1/3$ of the transit time t_T, it is inevitable that the vast majority (86-88% in this case) of the injected carriers are lost to deep traps. The testing results above do not give an adequate measurement for the average deep capture time since the average measured time only includes the small fraction of deep trap events with randomly generated occurrence times less

than those of the more common shallow traps; an artifact of the multi-level trap selection routines in the test platform. More accurately, average deep capture time should be given by the average amount of free time prior to the trapping event, which should be the sum of the measured deep capture time and all the preceding shallow capture times for each carrier. In these particular tests, 2.90 to 2.94 million shallow trap events are registered as compared to 8,605 to 8,755 deep trap events. This translates to approximately 337 shallow traps for each deep trap, and thus, given the shallow capture times listed, translates to a real measured deep capture time of around $0.336t_T$, which is inline with the pre-assigned average deep capture time of $1/3t_T$. Likewise, other tests with higher preset deep capture times produced real average deep capture times which conform to the preset times. Figure 4-21 shows that the increase in the injection ratio typically corresponds to a 1-3% increase in the signal loss between the low injection cases and the highest injection case (r = 0.99).

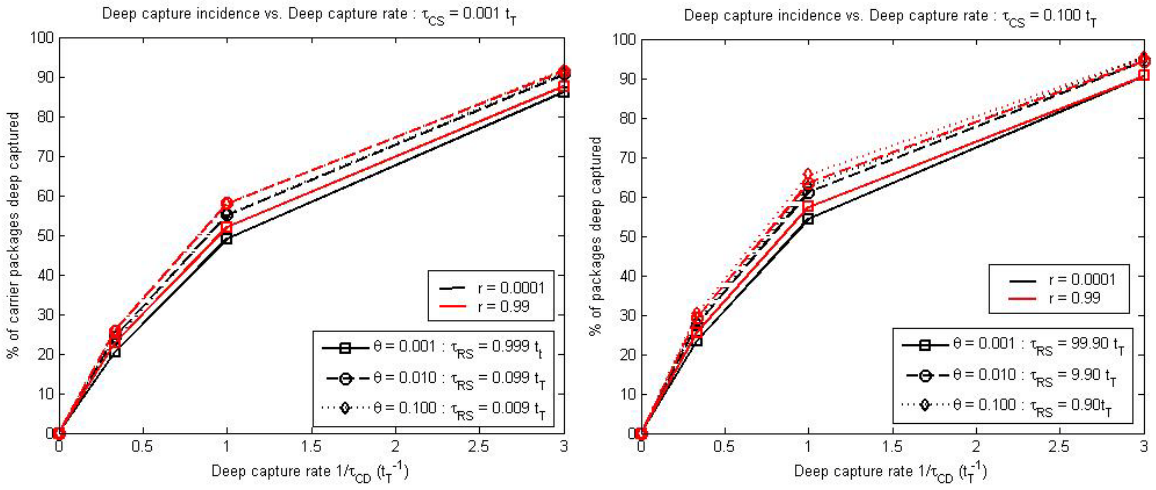

(a) *(b)*

Figure 4-21: Capture incidence as obtained for deep capture rates $1/\tau_{CD}$ = 0 (no deep capture), 1/3, 1, and 3. Cases shown are for (a)$\tau_{CS} = 0.001t_T$ and (b) $\tau_{CS} = 0.100\ t_T$.

For direct comparisons, Table 4-8 lists all dispersion results for this set of testing. As can be immediately noted with this set of tests, many simulations provided results where interference in

the derivative function resultant of the carrier attenuation made for immeasurable dispersion values. Likewise, where the reference dispersion $D_{0.0001}$ was indeterminable, so were all corresponding normalized dispersion values. Likewise, for cases with high deep capture incidence where $D_{0.99}$ was measurable, the result is badly distorted and only readable due to the field perturbation effects, which does not reflect the carrier spread as caused by the trap-release cycles. Notably, the highest rates of deep carrier capture ($\tau_{CD} = 1/3t_T$), almost universally led to unreadable or distorted dispersion numbers for all injection ratios.

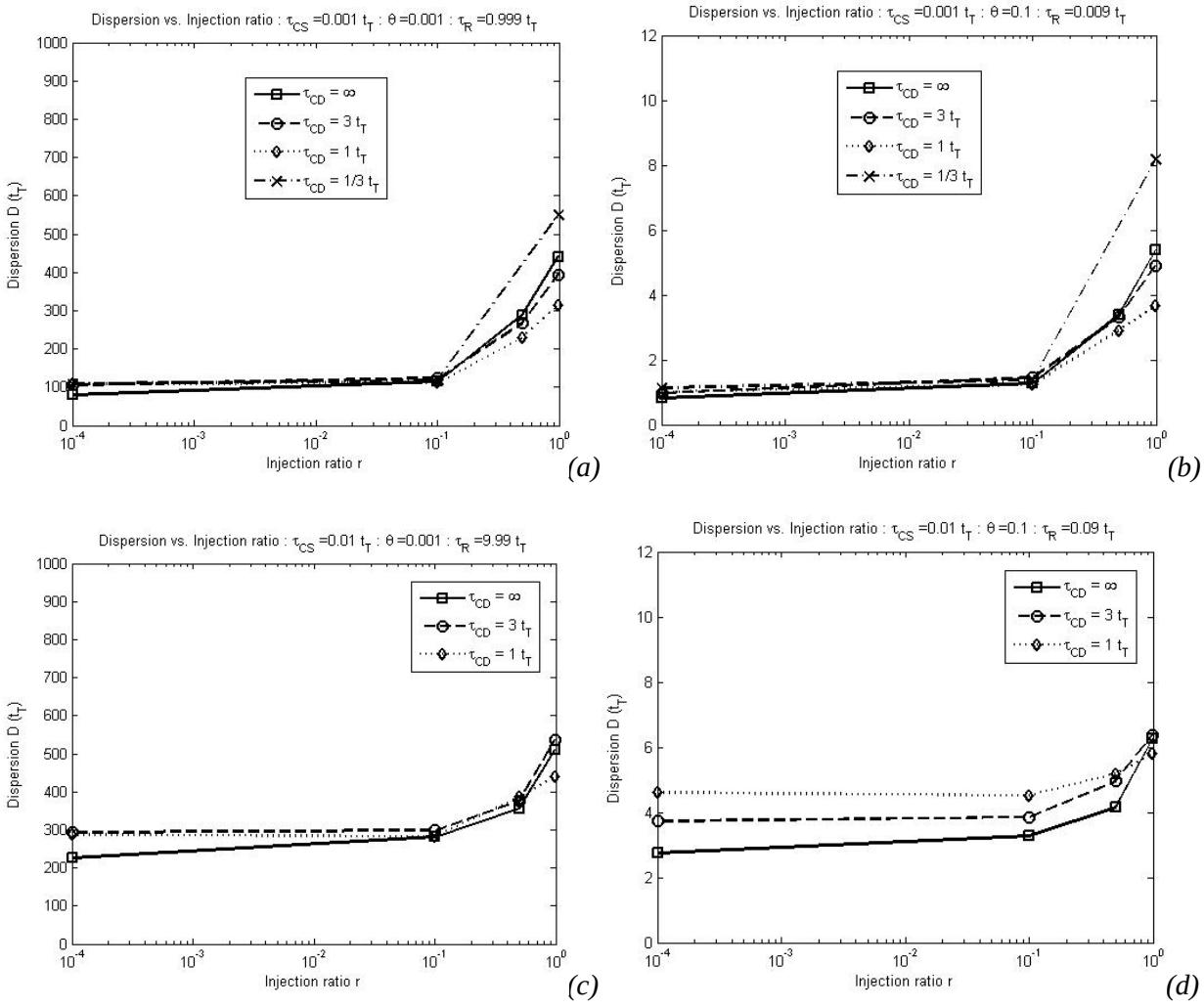

Figure 4-22: Dispersion measurements for bi-level trapping tests showing changes to injection ratio response for τ_{CS} and θ of (a) 0.001 t_T and 0.001 (b) 0.01 t_T and 0.1 (c) 0.01 t_T and 0.001 and (d) 0.01 t_T and 0.1.

Table 4-8: Dispersion results as measured and as normalized against the low injection ratio case (r = 0.0001) for all dual discrete level trapping tests. Many tests generated immeasurable dispersion results and are marked as indeterminable with 'ind'

$\tau_{CS}(t_T)$	θ_S	$\tau_{CD}(t_T)$	r = 0.0001	r = 0.10		r = 0.50		r = 0.99	
			$D_{0.0001}$	$D_{0.10}$	$\frac{D_{0.10}}{D_{0.0001}}$	$D_{0.50}$	$\frac{D_{0.50}}{D_{0.0001}}$	$D_{0.99}$	$\frac{D_{0.99}}{D_{0.0001}}$
0.001	0.001	1/3	108.646	118.176	1.088	ind	ind	548.885	5.052
0.001	0.001	1	108.456	111.259	1.026	229.435	2.116	315.120	2.906
0.001	0.001	3	105.689	122.813	1.162	267.017	2.526	393.734	3.725
0.001	0.01	1/3	12.645	14.422	1.141	21.249	1.680	70.385	5.566
0.001	0.01	1	9.806	14.099	1.438	24.824	2.531	30.896	3.151
0.001	0.01	3	9.645	13.179	1.366	29.716	3.081	43.766	4.538
0.001	0.1	1/3	1.133	1.369	1.208	Ind	Ind	8.175	7.213
0.001	0.1	1	1.010	1.240	1.227	2.907	2.878	3.663	3.627
0.001	0.1	3	0.967	1.447	1.496	3.307	3.419	4.891	5.057
0.01	0.001	1/3	ind	Ind	Ind	Ind	Ind	Ind	Ind
0.01	0.001	1	287.690	283.472	0.985	387.044	1.345	440.908	1.533
0.01	0.001	3	293.183	298.992	1.020	376.369	1.284	536.324	1.829
0.01	0.01	1/3	ind	Ind	Ind	Ind	Ind	Ind	Ind
0.01	0.01	1	32.548	31.801	0.977	40.310	1.239	44.816	1.377
0.01	0.01	3	29.280	30.172	1.031	38.857	1.327	54.574	1.864
0.01	0.1	1/3	ind	Ind	Ind	Ind	Ind	Ind	Ind
0.01	0.1	1	4.601	4.515	0.981	5.183	1.127	5.792	1.259
0.01	0.1	3	3.726	3.856	1.035	4.949	1.328	6.365	1.708
0.1	0.001	1/3	ind	Ind	Ind	Ind	Ind	Ind	Ind
0.1	0.001	1	ind	Ind	Ind	Ind	Ind	771.637	Ind
0.1	0.001	3	849.339	796.517	0.938	759.619	0.894	821.081	0.967
0.1	0.01	1/3	ind	ind	Ind	Ind	ind	Ind	ind
0.1	0.01	1	ind	ind	Ind	Ind	ind	101.574	ind
0.1	0.01	3	Ind	113.353	Ind	114.747	Ind	90.411	Ind
0.1	0.1	1/3	ind	ind	ind	Ind	ind	ind	ind
0.1	0.1	1	ind	ind	ind	ind	ind	9.228	ind
0.1	0.1	3	ind	ind	ind	9.952	ind	9.991	ind

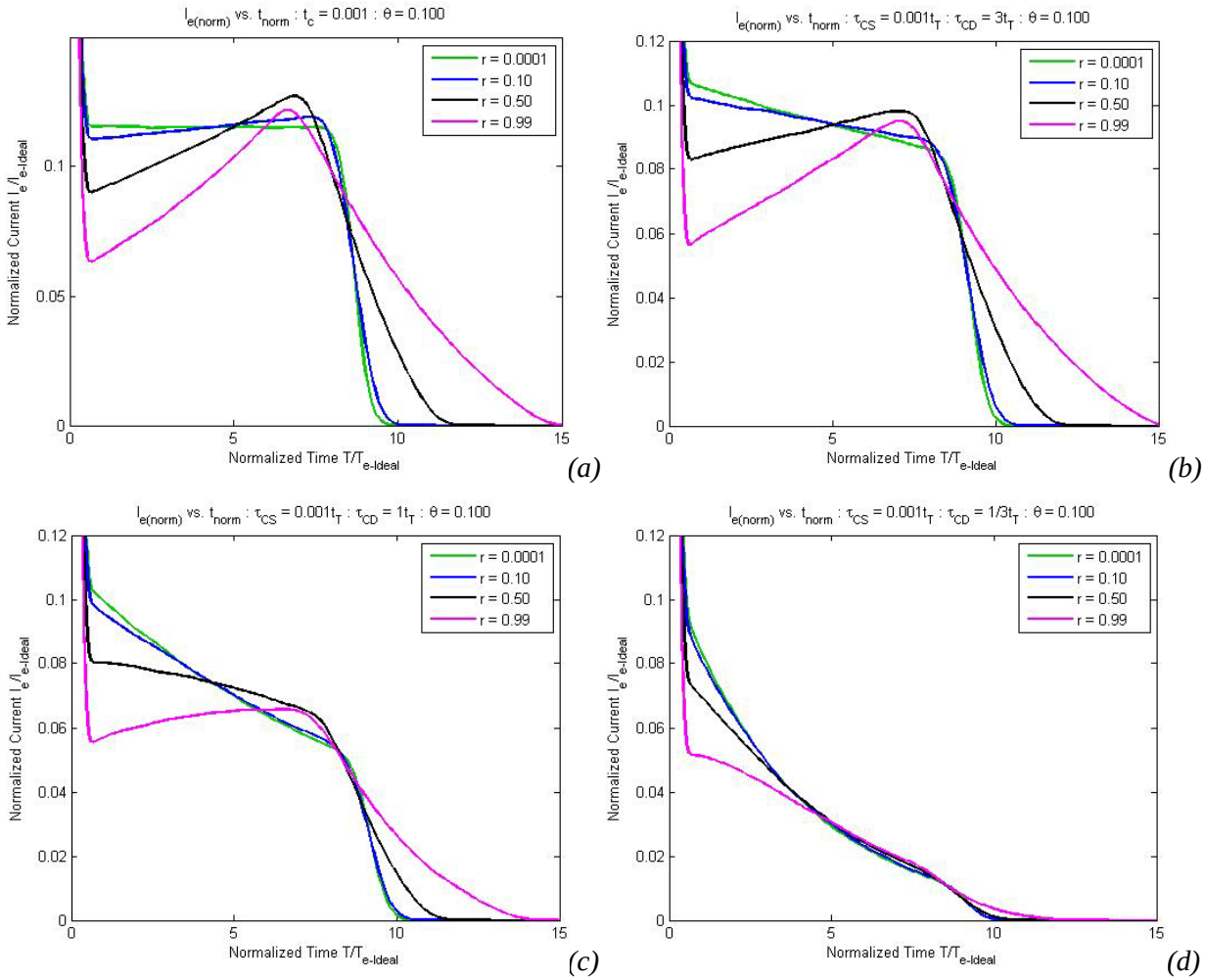

Figure 4-23: Processed transient TOF waveforms for four simulation sets with the same values for parameters τ_{CS} and θ_S, but varying preset deep capture time as τ_{CD} = (a) infinite, (b) $3t_T$, (c)$1t_T$, and (d) $1/3t_T$

Figure 4-22 contains the measured dispersions compared against the injection ratio (where measurements were obtainable), and again it appears that the proportionality of the change in response remains a product of the capture time, though increases in the deep trapping rate do track with an increase in the lower injection rate dispersion measurements. Figures 4-23 and 4-24 show how the TOF waveforms and their corresponding derivative functions respond to increased in the rate of deep trapping events starting with the first sets (4-23a and 4-24a) from the preceding section where no deep trapping occurred. Low and medium deep trapping rates (τ_{CD} = 3 t_T and 1 t_T respectively) maintain readable dispersion values, but the disruption in the

photocurrent can be seen by the way the deep capture profile counteracts the field balance related carrier acceleration. Figure 4-25 shows the suppressive effect of increased deep trapping rates on the field balance. This is a consequence of the permanently trapped carriers piled up near the positive electrode, as seen in the electron position histograms of Figure 4-26.

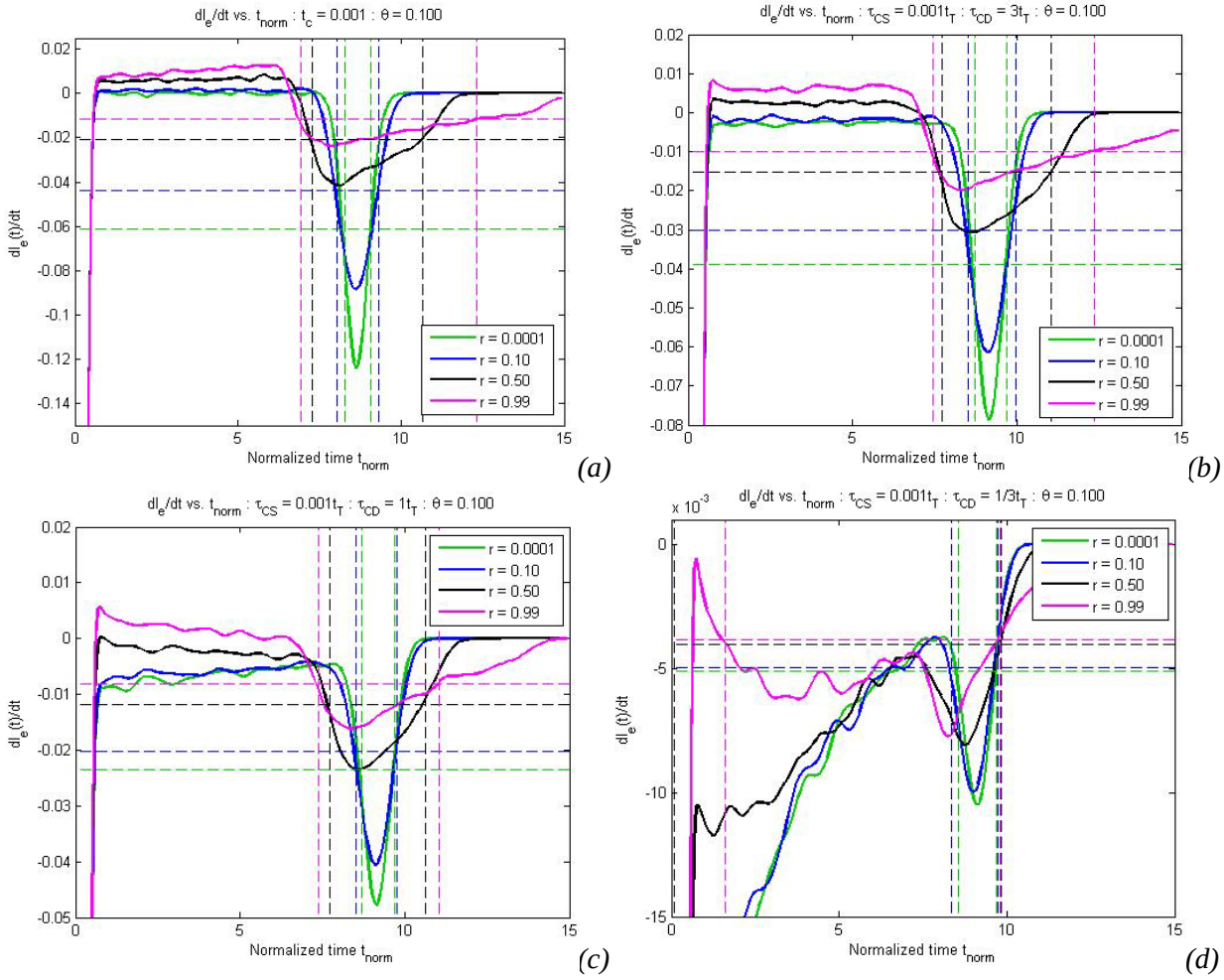

Figure 4-24: Derivative function plots for processed TOF waveforms of Figure 4-17, for τ_{DC} = (a) infinite, (b) $3t_T$, (c) $1t_T$, and (d) $1/3t_T$

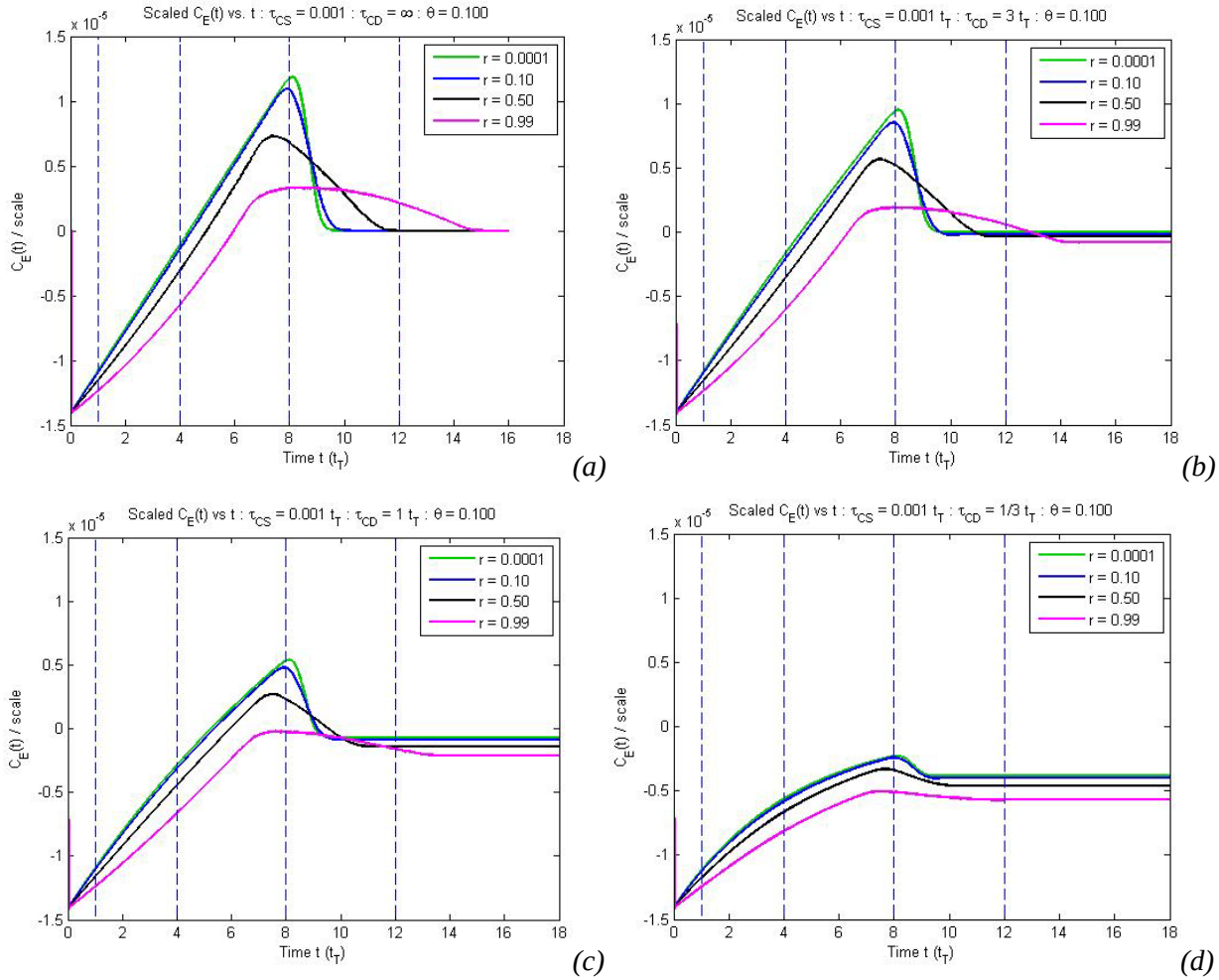

Figure 4-25: Field balancing factor plots for tests with varying deep carrier trapping rates. Shallow capture and release rates are kept constant with deep capture times of τ_{CD} = (a) infinity, (b) 3 t_T, (c) 1 t_T, and (d) 1/3 t_T.

The suppression of the field balance would normally correspond to a reduction in the average carrier drift velocity and thus maximum photocurrent, but because deep trapped carriers at the rear contribute to the field without being carried by it, it will only apply to the free carriers which comprise the forefront of the carrier package pulse. With higher deep trapping rates, the highest velocity carriers are more concentrated towards the front of the pulse which, due to the less pronounced variance in drift velocity, maintains better package cohesion, though any benefit to this is lost to the increase in the signal attenuation. Furthermore, slower carriers drift longer and are more susceptible to deep trapping.

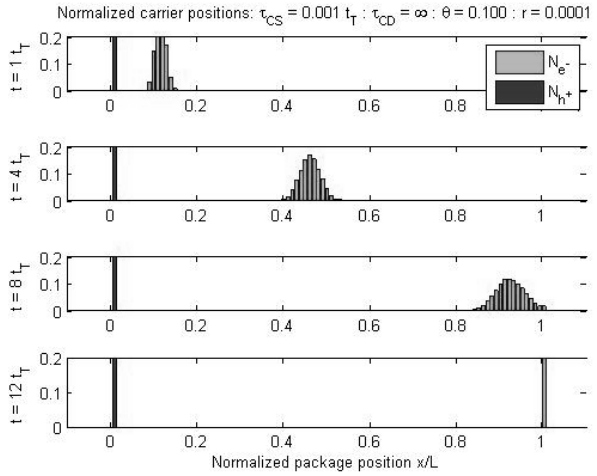
Normalized carrier positions: τ_{CS} = 0.001 t_T : τ_{CD} = ∞ : θ = 0.100 : r = 0.0001
t = 1 t_T
t = 4 t_T
t = 8 t_T
t = 12 t_T
N_{e^-}
N_{h^+}
Normalized package position x/L

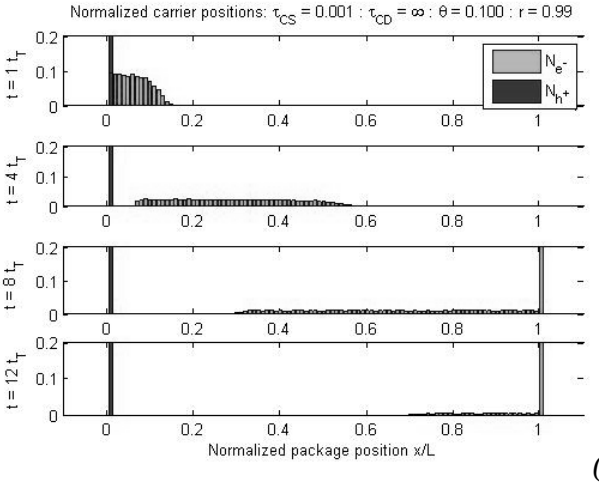
Normalized carrier positions: τ_{CS} = 0.001 : τ_{CD} = ∞ : θ = 0.100 : r = 0.99
t = 1 t_T
t = 4 t_T
t = 8 t_T
t = 12 t_T
N_{e^-}
N_{h^+}
Normalized package position x/L

(a)

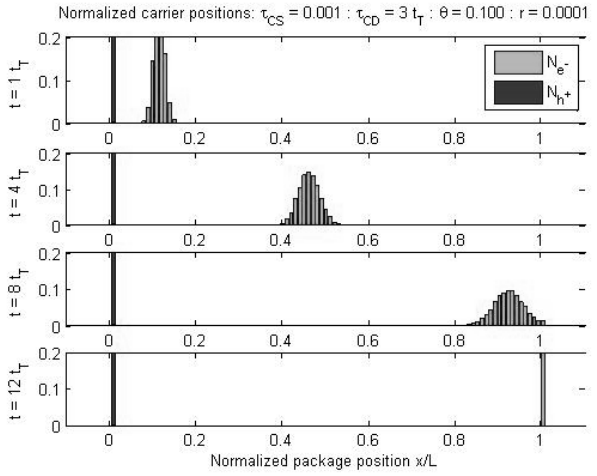
Normalized carrier positions: τ_{CS} = 0.001 : τ_{CD} = 3 t_T : θ = 0.100 : r = 0.0001
t = 1 t_T
t = 4 t_T
t = 8 t_T
t = 12 t_T
N_{e^-}
N_{h^+}
Normalized package position x/L

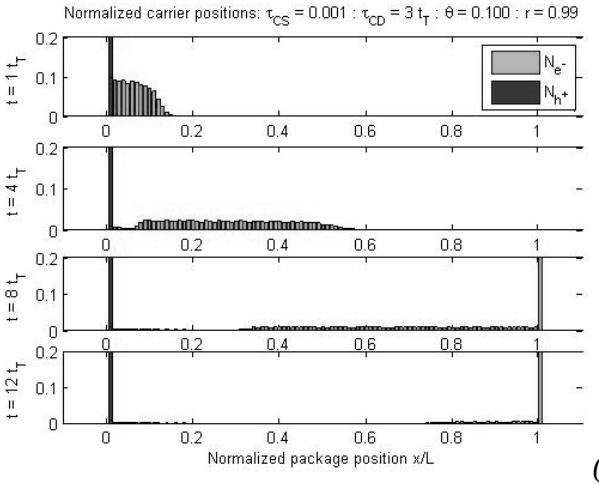
Normalized carrier positions: τ_{CS} = 0.001 : τ_{CD} = 3 t_T : θ = 0.100 : r = 0.99
t = 1 t_T
t = 4 t_T
t = 8 t_T
t = 12 t_T
N_{e^-}
N_{h^+}
Normalized package position x/L

(b)

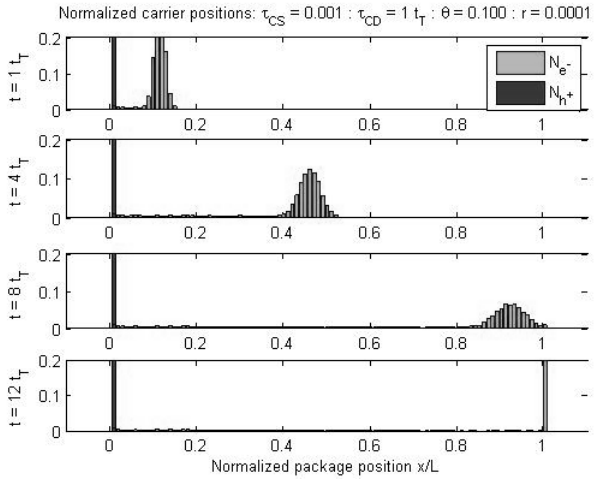
Normalized carrier positions: τ_{CS} = 0.001 : τ_{CD} = 1 t_T : θ = 0.100 : r = 0.0001
t = 1 t_T
t = 4 t_T
t = 8 t_T
t = 12 t_T
N_{e^-}
N_{h^+}
Normalized package position x/L

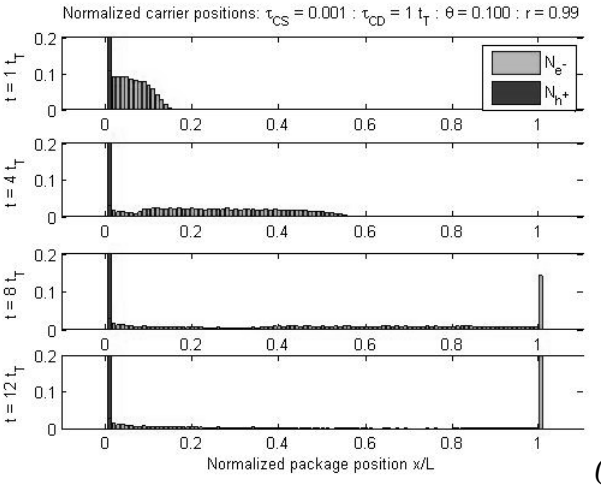
Normalized carrier positions: τ_{CS} = 0.001 : τ_{CD} = 1 t_T : θ = 0.100 : r = 0.99
t = 1 t_T
t = 4 t_T
t = 8 t_T
t = 12 t_T
N_{e^-}
N_{h^+}
Normalized package position x/L

(c)

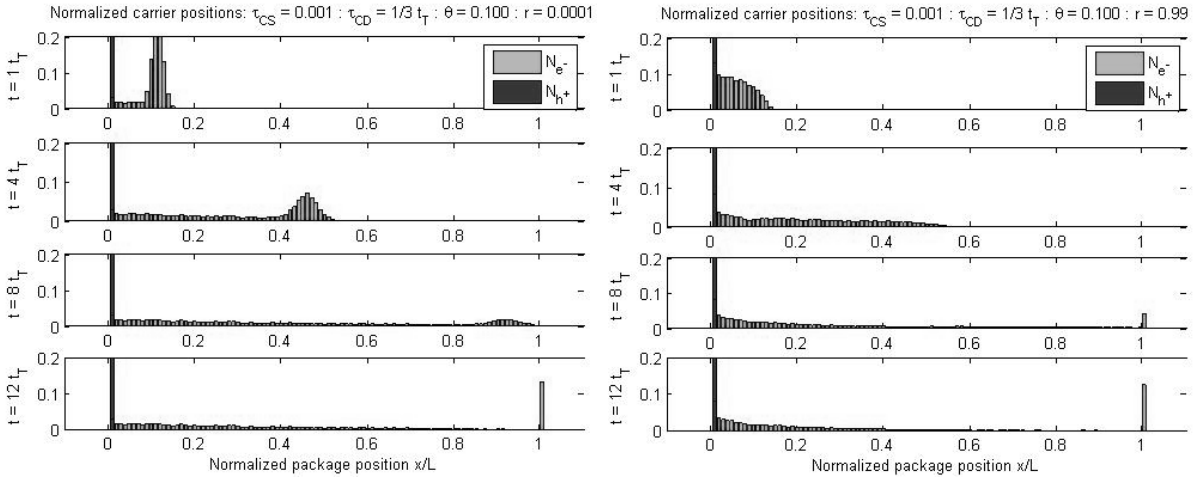

(d)

Figure 4-26: Histograms for carrier positions at sample times 1 t_T, 4 t_T, 8 t_T, and 12 t_T for varied deep trapping times of (a) infinity, (b) 3 t_T, (c) 1 t_T, (d) 1/3 t_T

4.2.3 Gaussian shallow trapping

The final part of this work will serve to evaluate the artificiality of using discrete mono-energetic trapping levels, as opposed to the real-world analogue of statistically distributed trapping energy levels; for this work, a single Gaussian distributed energy range of mean E_{S0} and standard deviation $\sigma = \Delta E/2$. Tests are performed as with the above sections for a preset average capture time of $\tau_C = 0.010$ t_T, varying mobility reduction factor θ, and varying of the energy spread $\Delta E = 0.0001E_{S0}$, $0.01E_{S0}$, and $0.1E_{S0}$. The prior sections modeled their release times as computed from θ. Since this section derives the energy depth variance as a product of a specific trap depth, it becomes necessary to identify E_{S0}. This is done using the command line:

```
Es0 = k*temp*log(f*trs*tT);
```

Where the material specific properties used are the sample temperature `temp` = 293 K and the lattice vibration frequency `f` as 1×10^{11} Hz. For θ = 0.001, 0.01, and 0.1, this returned energy depths of 0.4654eV, 0.4067eV, and 0.3462eV respectively. As these energy depths correspond to specific times rather than normalized times, it becomes necessary to specify that for this set of

testing, the normalizing time t_T is based on a sample thickness of $L = 100\mu m$, an applied field of $E_0 = 1x10^7\ V{\cdot}m^{-1}$, and an electron drift mobility $\mu_{e0} = 1{\times}10^{-7}\ m^2{\cdot}V^{-1}{\cdot}s^{-1}$. Specifying these factors make this particular set of testing notably less generic in its applicability.

Table 4-9: Dispersion results for Gaussian distributed trap depth testing

τ_C	θ_S	ΔE (in E_{S0})	r = 0.0001	r = 0.10		r = 0.50		r = 0.99	
			$D_{0.0001}$	$D_{0.10}$	$\frac{D_{0.10}}{D_{0.0001}}$	$D_{0.50}$	$\frac{D_{0.50}}{D_{0.0001}}$	$D_{0.99}$	$\frac{D_{0.99}}{D_{0.0001}}$
0.010	0.001	0.0001	276.364	303.945	1.100	408.531	1.478	603.049	2.182
0.010	0.010	0.0001	28.088	32.144	1.144	42.329	1.507	59.788	2.129
0.010	0.100	0.0001	3.219	3.538	1.099	4.715	1.465	7.061	2.194
0.010	0.001	0.01	302.008	319.885	1.059	404.841	1.340	601.157	1.991
0.010	0.010	0.01	28.611	29.788	1.041	41.917	1.465	58.225	2.035
0.010	0.100	0.01	2.994	3.624	1.210	4.902	1.637	7.763	2.593
0.010	0.001	0.1	629.192	486.012	0.772	726.437	1.155	881.458	1.401
0.010	0.010	0.1	50.057	58.377	1.166	68.314	1.365	78.238	1.563
0.010	0.100	0.1	4.775	4.951	1.037	5.680	1.190	9.220	1.931

The measured and low injection case normalized dispersion results of this set of testing are listed above in Table 4-9. From the measured results, it seems evident that there is no appreciable distinction between the dispersion values for low and medium spread tests. Figure 4-27 shows the dispersive response to injection ratio, measured and low-injection normalized, which suggests minimal changes in dispersion between lower spread tests, and a high proportional increase in the dispersion with a wider spread. This is supported by the side-by-side comparisons in Figure 4-28, which shows near perfect overlap between the two for all three examples. High trap energy spread resulted in a roughly 20% decrease in the equilibrium current and corresponding increase in the transit times without any disproportionate rise in the dispersion.

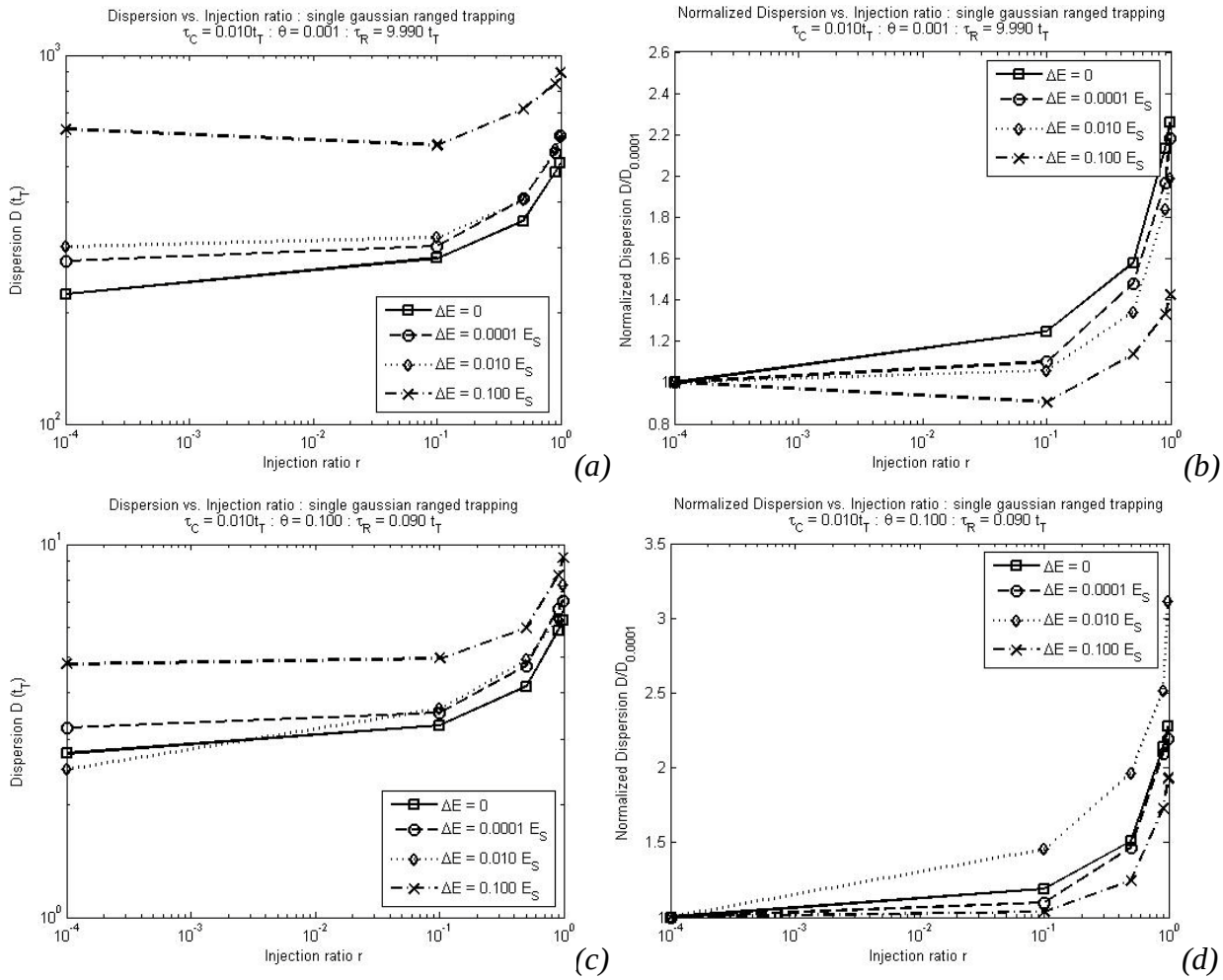

Figure 4-27: Dispersion as measured and normalized against low injection case compared with injection ratio for single Gaussian range trapping tests, including tests for $\tau_C = 0.010\ t_T$ and (a,b) $\theta = 0.001$ and (c,d) $\theta = 0.1$

That the injection ratio dispersion increases are proportionally inline with the low energy spread tests implies that the heightened spread test behaves more like a modest reduction in the mobility reduction factor. This is a reasonable assumption, given that the high energy spread tests all returned increased average release times, and thus a reverse modulation of the mobility reduction factor θ. The amount of modulation in θ is tied to the actual amount of spread in energy depth, with tests that had the deepest traps (and thus lowest baseline θ) exhibiting more susceptibility to modulation via the examined spread ratios.

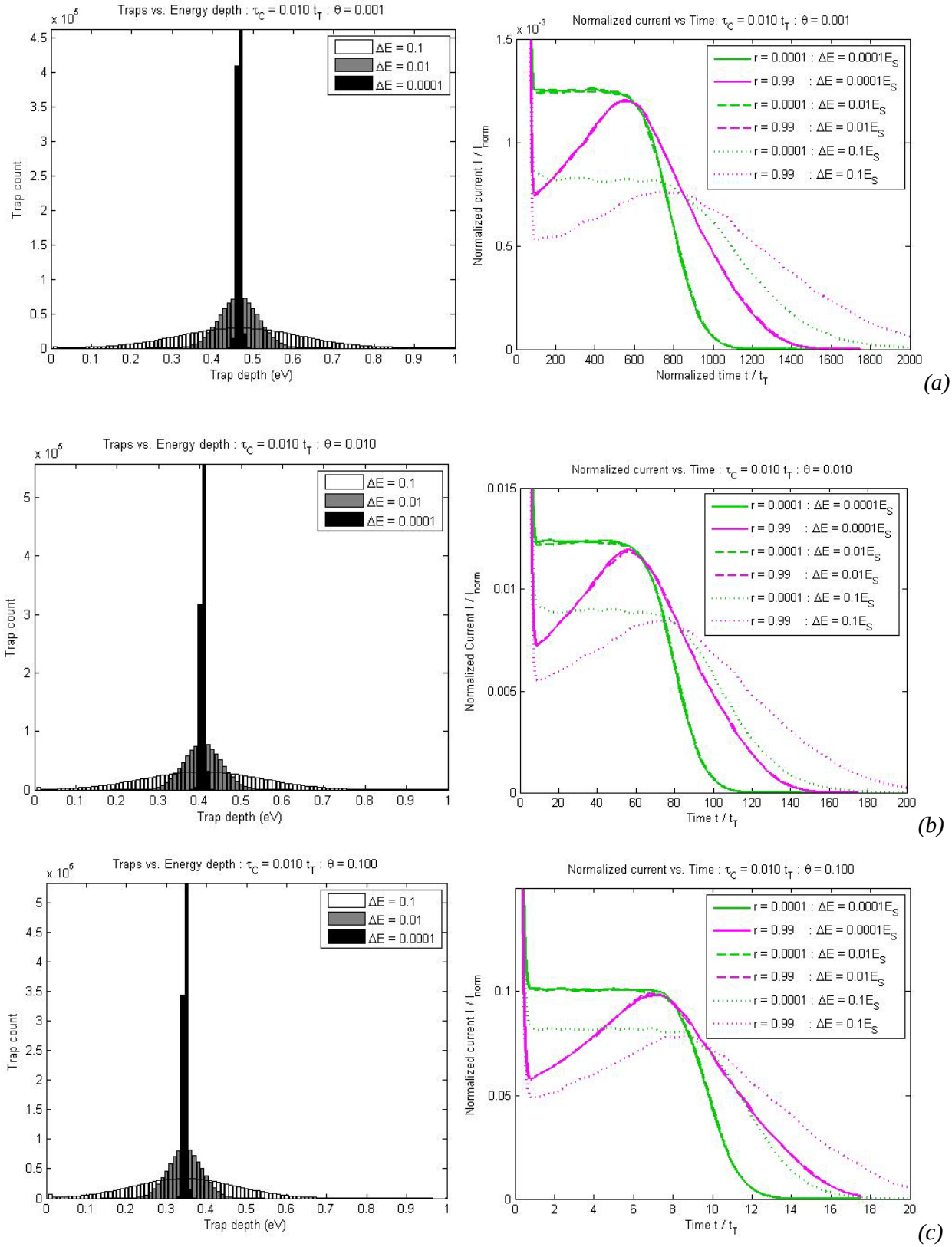

Figure 4-28: Trap depth histograms and corresponding TOF waveforms for lowest and highest injection ratios by variance ΔE for τ_C = 0.010 and θ= (a) 0.001, (b) 0.010, and (c) 0.100.

Table 4-10: Base trap energy depths as computed for τ_C = 0.010 t_T and varied θ_S, variances, corresponding expected and experimental release times, and the effective mobility reduction θ_{eff}.

θ_S	ΔE (in E_{S0})	E_{S0} (a-Se)	ΔE (a-Se)	$\tau_{R-E_{S0}}$	τ_{R-exp}	θ_{eff}
0.001	0.0001	0.4654	0.00004654	9.990	9.987	0.0010
0.010	0.0001	0.4067	0.00004067	0.990	0.989	0.0100
0.100	0.0001	0.3462	0.00003462	0.090	0.090	0.1000
0.001	0.01	0.4654	0.004654	9.990	10.028	0.0010
0.010	0.01	0.4067	0.004067	0.990	0.994	0.0100
0.100	0.01	0.3462	0.003462	0.090	0.090	0.1000
0.001	0.1	0.4654	0.04654	9.990	15.282	0.0007
0.010	0.1	0.4067	0.04067	0.990	1.371	0.0072
0.100	0.1	0.3462	0.03462	0.090	0.114	0.0806

Because there is so very little variation in the release time between the low and middle range energy spread tests, and thus negligible change in the mobility reduction, there's no reason to expect any change in the photocurrent TOF curves, their corresponding differential functions, or the dispersion measurements derived thereof, as illustrated in Figure 4-28. Furthermore, there's no expected added variance between injection ratio tests beyond what has been documented in prior sections.

In a simulated study like this work, θ can be the controlling factor in the release time, or dependent upon a specified release time; either way, it can be easily measured afterwards by recording the averages of the capture and release times. In an experimental work, theta must be extracted by measuring the equilibrium current at detailed balance. A mono-energetic trapping scheme is not a realistic feature to incorporate when proposing a density of states profile for a material sample, but we know from the results of this section that there exists a threshold energy spread below which it behaves as a discrete level, and beyond which, the mobility reduction factor is compromised from that of the trap concentration peak, leading to possible misinterpretation of the baseline depth of said peak. The challenge, thus, is distinguishing a deep and narrow trap energy spread from a shallow and broad trap energy spread. Variation in this

section manifests as a change of release time, so the effect on the factors affected by the injection ratio testing which is the crux of this work is indistinguishable from that of Section 4.2.1.

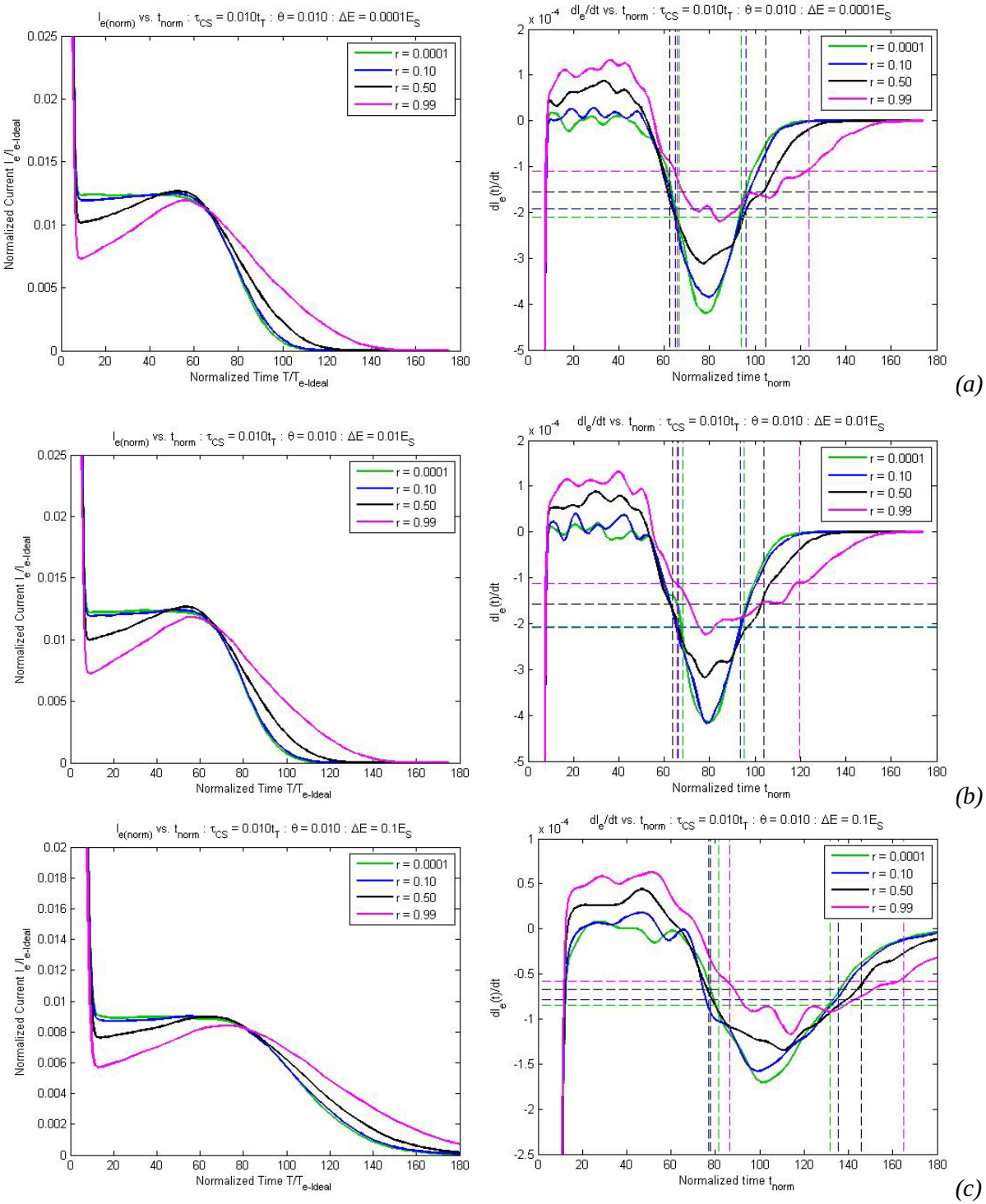

Figure 4-29: TOF waveforms and differential functions for Gaussian trap energy depth testing. Tests shown are for $\tau_C = 0.010\ t_T$, $\theta = 0.010$, and ΔE = (a) 0.0001, (b) 0.01, and (c) 0.1

Because of this, injection ratio testing using the current testing model is an inadequate tool for use in affirming a proposed model. Toward this end, future enhancements to the model may yet yield more useful options in interpreting experimental results.

4.3 Summary

The goal of this chapter was to parse the abundance of data from testing in the six stages of simulation work so as to catalogue the effects of injection ratio testing on the parameters laid out in chapter 3. In doing so, the expectation was that we could identify how each such parameter contributed to the shaping of the TOF photocurrent waveforms, and how the dispersion *D* which defines the peak carrier collection time range is impacted by the injection ratio as applied to the initial and intermediate factors of TOF modeling.

Phase one focused on the initial conditions of the simulation work. It replicated carrier drift in a crystalline semiconductor by foregoing the effects of band-gap localizations which characterize amorphous devices. Testing without variance in the initial conditions demonstrated the influence of the time-dependent field balancing factor $C_E(t)$, which illustrated that increases in the applied injection ratio fostered an acceleration in the carrier package pulse which mirrored the field balance. Introducing variance in the generation time introduced spread in the carrier pulse which illustrated the dispersive effect of mutual coulombic repulsion between carrier packages. Creating variation in the initial generation position changed the profile of the carrier spread, and added the counterbalancing effects of the second species of carrier.

Phase two simulated the intermediary effects of carrier trapping and release in three ways. The first, mono-energetic discrete trapping, examined the relationship between the capture time τ_C and the release time τ_R as calculated by the mobility reduction factor θ. This established that θ is

a useful tool in extrapolating capture or release times based on the measurements of the detailed balance current. Furthermore, it established that the shape of the TOF curve is more highly dependent on the capture time than the release time due to the added drifting time between capture events. The next section, based on dual discrete level trapping, showed the attenuating effects of deep carrier trapping, and how the field balance is suppressed as a consequence of a high rate of deep trapping. The final section examined a single Gaussian distributed trapping energy region, and determined that a practical threshold exists in the spread of these traps above which θ is modulated downward, complicating the measurability of the release times.

Chapter 5 Conclusion

Time of flight simulations provide a valuable tool to test theoretical density of states models, but are limited in how different variables can produce differing results distinct to each. The primary purpose of this work was to catalogue the effects of modulating the injection ratio in as generic a fashion as possible, so as to identify and catalogue the expectable changes to the system.

5.1 Observations

Several items of interest arose from the injection ratio testing in this work. In phase one, we established how the shape of the time of flight curve distorted as r increased. Since the voltage drop across the bulk needed to remain constant, as r increased, the injected carriers had to change the gradient of the applied electric field across the bulk without altering the total sum field. This was implemented with the field balance $C_E(t)$ which added uniformly to the applied and injected fields, and manifest in testing as a modulator of the average carrier drift velocity. $C_E(t)$ was dependent on the carrier concentration profile, and was most influential when carriers were most concentrated near either electrode. While $C_E(t)$ provides for the variance in the average drift velocity of each package in the carrier pulse, the expanding distance between them was entirely a product of the coulombic repulsion between carriers, was visible in effect on the shifting gradient of the electric field, and was mostly irrelevant below $r = 0.10$.

Phase two highlighted the dependency of the TOF waveform shape on the capture time τ_C and the release time τ_R as derived from the mobility reduction factor θ. These studies showed that θ proportionally controlled the magnitude of the detailed balance current and inversely and proportionally controlled the runtime of the simulations while τ_C dictated the shape of the curve

in terms of the definition of the knee and in the extent to which the collection process is dragged out. Short capture times resulted in a carrier pulse which maintained a high degree of cohesion at low injection, and so had much capacity for proportional spread as *r* increased. By contrast, higher capture times lost package cohesion to the trapping effects, and so did not experience such high gains of injection ratio related dispersion.

From this work, the things we expect to see under simulated conditions are as follows. In cases where illumination time approaches infinitesimal durations, or at least much less than the capture times, we expect to see a high impulse-like current peak at generation, followed by the mass thermalization to the detailed balance state where the current stays essentially constant until the foremost carriers reach their destination electrode. The TOF curve's knee shows how well the packages maintained their cohesion. A sharp knee with a short tail indicated that all collected carriers arrived in a very short time period, which shows high cohesion. An extended tail shows that the cohesion has been mostly lost to one or more of the various effects encountered in simulation. Injection ratio testing showed that rates exceeding $r = 0.10$ produced a distortion of the waveform that first appeared as a suppressed current state which grew to an accelerated state; the capacity for this change being dependant on how well the pulse maintained its cohesion. In these tests, the highest maximum currents often resulted from the $r = 0.50$ tests rather than for $r = 0.99$ because the lower ratio exhibited less cohesion loss.

5.2 Implications

Aside from cataloguing of the effects of injection ratio testing, there is evidence that a more complete library of dispersion measurements could be useful in testing the veracity of proposed DOS profiles. As discussed in section 2.6, Laplace transform analyses of the measured TOF waveforms can produce illustrative approximations of the material DOS. This model can be

easily retooled to replicate the DOS estimate by combining multiple distributions into a continuous DOS profile. If the expected profile is simple enough, gauging the injection ratio response can be useful in refining the relationship between the trap depth mean and its corresponding variance.

Though this approach may be useful for single level or narrow range trapping states, it may not be suitable for detecting extended ranges of energy depths, which as previously discussed, can obscure the actual trap state depth by diminishing θ. Nor is this a complete means for evaluating multiple shallow level trapping ranges such as proposed for the a-Se DOS model as described in Chapter 2.

5.3 Future Work

The model in its current state is incomplete. Currently, it can be easily tooled to simulate any single distribution of electron-hole pair generation time (to simulate illumination duration) or position (to simulate photoabsorption depth). It can be adjusted for specific illumination times and intensities or be set as a ratio of the applied electric field. It can handle up to four different distributions and concentrations of trapping states for electrons without needing to separate them by energy range. It can handle both species of charge carrier drifting at different rates according to the magnitude and polarity of the electric field.

What it cannot currently do is as follows. It cannot yet simulate trap-release processes for hole carriers. It does not consider diffusion as a drifting mechanism for carriers. It does not consider the incidence of recombination between electrons and holes as they pass each other in the medium. It cannot simulate the reduction of available trapping states due to occupation. It does not factor in the known effects of a high electric field on the release time of trapped

carriers; notably more prevalent in cases where high injection ratios are applied to already high electric fields. It cannot simulate the loss of detector sensitivity due to the residual effects of deeply trapped carriers accumulating over sequential simulations.

5.3.1 Recombination effects

The first such limitation to the model comes from recombination of carriers as they drift past each other in the medium. Through most of this work, this was a non-issue because the carriers were set to generate near the surface of the sample, guaranteeing that the hole carriers were collected at the onset. Furthermore, the nature of the testing ignored the three-dimensionality of the sample. At a practical level, there will be greater rates of recombination at higher injection levels, given that the carrier concentrations will be higher. Carrier recombination would behave much like collection, with the carriers being permanently removed from all current and field calculations. The subsequent attenuation would abate as the bulks of each species pass each other.

In the generic sample, the trap concentration which dictates capture time is overridden by the testing parameters, so the geometry of the pixel is completely irrelevant. Carrier recombination is dependent on the proximity of the carriers which exist in finite quantities across the sample, so the incidence of recombination depends highly on the geometry of the pixel which dictates the carrier concentrations. Assuming no increase in per-pixel illumination, larger pixel areas correspond to lower carrier concentration, which in turn becomes a lower rate of recombination. Specifying the *x*-axis as being parallel with the applied electric field, we assume that the carriers are distributed evenly across the *y* and *z* axes for simplicity. Calculating for recombination would require specification of the area and thickness of the sample. These would translate to carrier concentration profiles for each of the placement bins already handled by this model.

Comparisons of concentration profiles at each time step would return a count of recombined carrier packages in each bin which would be appropriately deducted from each profile.

5.3.2 Trap filling effects

Trap filling effects are a reduction of available trap states, and thus increase of capture time in their regions, due to occupancy by trapped carriers. As with recombination, this could not be modelled in a generic sample because the trap concentration was neglected in favour of a preset capture time. Simulation of this would require that upon each release, each carrier package would "look ahead" at the varying trap concentrations of each placement bin to estimate an average concentration to devise a new capture time from. This would likewise require that each placement bin keep track of how many carrier packages in each are actually trapped, and of which type, so as to deduct the appropriate scale-adjusted amount from the correct base trap concentrations.

5.3.3 Poole-Frenkel emission

Under an adequately high applied electric field, trapped carriers can experience a reduction in trap release time due to the reduction of the potential barrier keeping the carrier packaged localized. This potential reduction lowers the energy required for a thermal fluctuation to elevate the carrier back into the conduction band. The release time reduction can be modified[19] from equation 3-10 as:

$$t_{release} = -\log(X)/f \cdot e^{-\left(\frac{E_S - \Delta\varphi_{PF}}{k \cdot T}\right)} \cdot t_T \qquad (5\text{-}1)$$

where:

$$\Delta\varphi_{PF} = \left(\frac{e^3}{\pi\varepsilon_r\varepsilon_0}\right)^{1/2} \cdot E(x,t)^{1/2} \qquad (5\text{-}2)$$

and noting that the applied field in this testing is position and time dependent. Simulating this generically was impractical because it could simply be said that the release time reduction was factored into the mobility reduction choices. In applied testing, it becomes more relevant both as the applied field is increased and as the injection ratio increases, given that the highest injection ratios tested registered field balancing factors of as much as 50% of the applied field.

5.3.4 Ghosting and residual effects

Ghosting is the loss of detector sensitivity which results from deeply trapped carriers lingering in the bulk after an illumination. At a practical level, this shows up in sequential illuminations as an afterimage of the previous exposures. The sensitivity loss is primarily a result of recombination between currently drifting carriers of one type interacting with previously trapped carriers of the other type, which, of course, depends on the concentration of the trapped carriers. In these simulations, ghosting loss is not possible because the simulation parameters set generation depth to near-zero, and thus permit no mingling between carrier species. There is, however, the occupancy of the deep traps reducing their availability, and the corresponding field distortion due to the pre-existing immobile carrier charges.

Accounting for cumulative testing requires that deep trapping records be preserved between trials. The current model presets the baseline of each field bin to the magnitude of the applied field E_0, which is uniform across the bulk. It then adapts the field according to carrier charge contributions and the field balancing factor. Preserved trap records can be easily transferred to predefine the baseline field. If recombination losses are to be considered, they can be done by considering the pre-existing carrier packages in the concentration estimates, and applying the

methodology conceptualized in Section 5.3.1. Carrier packages to be recombined can be randomly chosen from either drifting or trapped carriers; depending on their respective concentrations.

References

[1] Mettler, F. A. , Thomadsen, B. R. , Bhargavan, M, Gilley, D. B. & Grey, J. E. (2008). Medical radiation exposure in the U.S. in 2006: preliminary results. *Health physics*, *95*(5), 502-507. DOI: 10.1097/01.HP.0000326333.42287.a2

[2] Hall, E. J., & Giaccia, A. J. (2006). *Radiobiology for the radiologist*. (6th ed.). Philidelphia: Lippincott Williams & Wilkins.

[3] Ferlini, C, De Angelis, C, Biselli, R, Distefano, M, & Scambia, G. (1998). Sequence of metabolic changes during x-ray-induced apoptosis. *Experimental Cell Research*, *247*(1), 160-167.

[4] S. O. Kasap and J. A. Rowlands, Direct-conversion flat panel X-ray image detectors, *IEE Proc.-CDS*, ***149***, pp. 85-96, (2002*).*

[5] Kasap, S. , Frey, J. , Belev, G. , Tousignant, O. & Mani, H. (2011). Amorphous and polycrystalline photoconductors for direct conversion flat panel x-ray image sensors. *Sensors*, *11*(5), 5112-5157. DOI: 10.3390/s110505112

[6] O. Frisch, British Atomic Energy Report No. BR-49, (1944). Unpublished

[7] Goldan, A. H., Fang, Y., Karim, K. S., Tousignant, O., & Mani, H. (2009). Amorphous selenium detector utilizing a frisch grid for photon-counting imaging applications. Proc. of SPIE Vol. 7258. doi: 10.1117/12.813708

[8] Sazanov, A. , Straikrelev, D. , Lee, C. & Nathan, A. (2005). Low-temperature materials and thin film transistors for flexible electronics. *Proceedings og the IEEE*, *95*(8), 1420-1428. DOI: 10.1109/JPROC.2005.851497

[9] Thin-film Transistor. (22 December, 2011). In *Wikipedia*. Retrieved Jan 10, 2012, from http://en.wikipedia.org/wiki/Thin-film_transistor

[10] Guha, S, & Yang, J. US Department of Energy, National Renewable Energy Laboratory. (2007). *High-efficiency amorphous silicon and nanocrystalline silicon-based solar cells and modules* Retrieved from http://www.nrel.gov/pv/thin_film/docs/USOC1A.pdf

[11] Ramo, S. (1939). “Currents induced by electron motion”. *Proceedings of the IRE*, *27*(9), 584-585.

[12]Schmidlin, F. (1977). Theory of multiple trapping. *Solid State Communications*, *22*(7), 451-453. doi: 10.1016/0038-1098(77)90123-5

[13] Nagase, T., Kishimoto, K., & Naito, H. (1999). High resolution measurement of localized-state distributions from transient photoconductivity in amorphous and polymeric semiconductors. *Journal of Applied Physics*, *86*(9), 5026-5035.

[14] Koughia, K., Shakoor, Z., Kasap, S.O., & Marshall, J.M. (2005). Density of localized electronic states in a-se from electron time-of-flight photocurrent measurements. *Journal of Applied Physics*, *97*(3), doi: 10.1063/1.1835560

[15] Gueoguieva, M. , Main, C. , Reynolds, S. , Bruggemann, R. & Longeaud, C. (2002). Probing localized states distributions in semiconductors by laplace transform transient photocurrent spectroscopy. *Journal of Non-Cystalline Solids*, *299-302*, 541-545. DOI: 10.1016/S0022-3093(01)00967-X

[16] Kim, K.H., Oh, K.N., & Kim, S.U. (2002). Determination of localized states in nanocrystalline CdZnTe by using a transient photocurrent analysis. *Journal of the Korean Physical Society*, *41*(4), 471-474.

[17] Blakney, R. & Grunwald, H. (1967). Small signal current transients in insulators with traps. *Physical Review*, *159*(3), 658-664.

[18] Papadakis, A. C. (1967). Theory of transient space-charge perturbed currents in insulators. *J. Phys. Chem. Solids*, *28*, 641-647.

[19] Simmons, J. G. (1971). Conduction in thin dielectric films. *Journal of Physics D: Applied Physics*, *4*(5), 613-657. DOI: 10.1088/0022-3727/4/5/202